arXiv:1812.01679v1 [astro-ph.CO] 4 Dec 2018

Cluster Cosmology Constraints from the 2500 deg^2 SPT-SZ Survey:
Inclusion of Weak Gravitational Lensing Data from Magellan and the *Hubble Space Telescope*

S. Bocquet,[1,2,3] J. P. Dietrich,[1,4] T. Schrabback,[5] L. E. Bleem,[2,3] M. Klein,[1,6] S. W. Allen,[7,8,9]
D. E. Applegate,[3] M. L. N. Ashby,[10] M. Bautz,[11] M. Bayliss,[11] B. A. Benson,[12,3,13] M. Brodwin,[14] E. Bulbul,[10]
R. E. A. Canning,[7,8] R. Capasso,[1,4] J. E. Carlstrom,[12,3,15,2,16] C. L. Chang,[12,3,2] I. Chiu,[17] H-M. Cho,[18]
A. Clocchiatti,[19] T. M. Crawford,[12,3] A. T. Crites,[12,3,20] T. de Haan,[21] S. Desai,[22] M. A. Dobbs,[23,24]
R. J. Foley,[25,26] W. R. Forman,[10] G. P. Garmire,[27] E. M. George,[21,6] M. D. Gladders,[12,3] A. H. Gonzalez,[28]
S. Grandis,[1,4] N. Gupta,[29] N. W. Halverson,[30] J. Hlavacek-Larrondo,[31,32,8] H. Hoekstra,[33] G. P. Holder,[23]
W. L. Holzapfel,[21] Z. Hou,[3,15] J. D. Hrubes,[34] N. Huang,[21] C. Jones,[10] G. Khullar,[3,12] L. Knox,[35] R. Kraft,[10]
A. T. Lee,[21,36] A. von der Linden,[37] D. Luong-Van,[34] A. Mantz,[7,8] D. P. Marrone,[38] M. McDonald,[11]
J. J. McMahon,[39] S. S. Meyer,[12,3,15,16] L. M. Mocanu,[12,3] J. J. Mohr,[1,6,4] R. G. Morris,[9,7] S. Padin,[12,3,20]
S. Patil,[29] C. Pryke,[40] D. Rapetti,[1,4,30,41] C. L. Reichardt,[29] A. Rest,[42] J. E. Ruhl,[43] B. R. Saliwanchik,[43]
A. Saro,[44,1,4] J. T. Sayre,[30] K. K. Schaffer,[3,16,45] E. Shirokoff,[12,3] B. Stalder,[10] S. A. Stanford,[35,46]
Z. Staniszewski,[43] A. A. Stark,[10] K. T. Story,[7,8] V. Strazzullo,[1] C. W. Stubbs,[10,47] K. Vanderlinde,[48,49]
J. D. Vieira,[25,26] A. Vikhlinin,[10] R. Williamson,[12,3,20] and A. Zenteno[50]

[1]*Faculty of Physics, Ludwig-Maximilians-Universität, Scheinerstr. 1, 81679 Munich, Germany*
[2]*HEP Division, Argonne National Laboratory, Argonne, IL 60439, USA*
[3]*Kavli Institute for Cosmological Physics, University of Chicago, Chicago, IL 60637, USA*
[4]*Excellence Cluster Universe, Boltzmannstr. 2, 85748 Garching, Germany*
[5]*Argelander-Institut für Astronomie, Auf dem Hügel 71, 53121 Bonn, Germany*
[6]*Max Planck Institute for Extraterrestrial Physics, Giessenbachstr. 1, 85748 Garching, Germany*
[7]*Kavli Institute for Particle Astrophysics and Cosmology, Stanford University, 452 Lomita Mall, Stanford, CA 94305, USA*
[8]*Department of Physics, Stanford University, 382 Via Pueblo Mall, Stanford, CA 94305, USA*
[9]*SLAC National Accelerator Laboratory, 2575 Sand Hill Road, Menlo Park, CA 94025, USA*
[10]*Center for Astrophysics | Harvard & Smithsonian, Cambridge MA 02138, USA*
[11]*Kavli Institute for Astrophysics and Space Research, Massachusetts Institute of Technology, 77 Massachusetts Avenue, Cambridge, MA 02139, USA*
[12]*Department of Astronomy and Astrophysics, University of Chicago, Chicago, IL 60637, USA*
[13]*Fermi National Accelerator Laboratory, Batavia, IL 60510-0500, USA*
[14]*Department of Physics and Astronomy, University of Missouri, 5110 Rockhill Road, Kansas City, MO 64110, USA*
[15]*Department of Physics, University of Chicago, Chicago, IL 60637, USA*
[16]*Enrico Fermi Institute, University of Chicago, Chicago, IL 60637, USA*
[17]*Institute of Astronomy and Astrophysics, Academia Sinica, Taipei 10617, Taiwan*
[18]*NIST Quantum Devices Group, Boulder, CO 80305, USA*
[19]*Departamento de Astronomia y Astrosifica, Pontificia Universidad Catolica, Chile*
[20]*California Institute of Technology, Pasadena, CA 91125, USA*
[21]*Department of Physics, University of California, Berkeley, CA 94720, USA*
[22]*Department of Physics, IIT Hyderabad, Kandi, Telangana 502285, India*
[23]*Department of Physics, McGill University, Montreal, Quebec H3A 2T8, Canada*
[24]*Canadian Institute for Advanced Research, CIFAR Program in Cosmology and Gravity, Toronto, ON, M5G 1Z8, Canada*
[25]*Astronomy Department, University of Illinois at Urbana-Champaign, 1002 W. Green Street, Urbana, IL 61801, USA*
[26]*Department of Physics, University of Illinois Urbana-Champaign, 1110 W. Green Street, Urbana, IL 61801, USA*
[27]*Huntingdon Institute for X-ray Astronomy, LLC, USA*
[28]*Department of Astronomy, University of Florida, Gainesville, FL 32611, USA*
[29]*School of Physics, University of Melbourne, Parkville, VIC 3010, Australia*
[30]*Department of Astrophysical and Planetary Sciences and Department of Physics, University of Colorado, Boulder, CO 80309, USA*
[31]*Department of Physics, Université de Montréal, Montreal, Quebec H3T 1J4, Canada*
[32]*Kavli Institute for Particle Astrophysics and Cosmology, Stanford University, 452 Lomita Mall, Stanford, CA 94305-4085, USA*
[33]*Leiden Observatory, Leiden University, Niels Bohrweg 2, 2333 CA, Leiden, the Netherlands*
[34]*University of Chicago, Chicago, IL 60637, USA*

sebastian.bocquet@physik.lmu.de

[35] *Department of Physics, University of California, Davis, CA 95616, USA*

[36] *Physics Division, Lawrence Berkeley National Laboratory, Berkeley, CA 94720, USA*

[37] *Department of Physics and Astronomy, Stony Brook University, Stony Brook, NY 11794, USA*

[38] *Steward Observatory, University of Arizona, 933 North Cherry Avenue, Tucson, AZ 85721, USA*

[39] *Department of Physics, University of Michigan, Ann Arbor, MI 48109, USA*

[40] *Department of Physics, University of Minnesota, Minneapolis, MN 55455, USA*

[41] *NASA Ames Research Center, Moffett Field, CA 94035, USA*

[42] *Space Telescope Science Institute, 3700 San Martin Dr., Baltimore, MD 21218, USA*

[43] *Physics Department, Center for Education and Research in Cosmology and Astrophysics, Case Western Reserve University, Cleveland, OH 44106, USA*

[44] *INAF-Osservatorio Astronomico di Trieste, via G. B. Tiepolo 11, 34143 Trieste, Italy*

[45] *Liberal Arts Department, School of the Art Institute of Chicago, Chicago, IL 60603, USA*

[46] *Institute of Geophysics and Planetary Physics, Lawrence Livermore National Laboratory, Livermore, CA 94551, USA*

[47] *Department of Physics, Harvard University, 17 Oxford Street, Cambridge, MA 02138, USA*

[48] *Dunlap Institute for Astronomy & Astrophysics, University of Toronto, 50 St George St, Toronto, ON, M5S 3H4, Canada*

[49] *Department of Astronomy & Astrophysics, University of Toronto, 50 St George St, Toronto, ON, M5S 3H4, Canada*

[50] *Cerro Tololo Inter-American Observatory, Casilla 603, La Serena, Chile*

ABSTRACT

We derive cosmological constraints using a galaxy cluster sample selected from the 2500 deg^2 SPT-SZ survey. The sample spans the redshift range $0.25 < z < 1.75$ and consists of 377 cluster candidates with SZ detection significance $\xi > 5$. The sample is supplemented with optical weak gravitational lensing measurements of 32 clusters in the range $0.29 < z < 1.13$ (using data from Magellan and the *Hubble Space Telescope*) and X-ray measurements of 89 cluster in the range $0.25 < z < 1.75$ (from *Chandra*). We rely on minimal modeling assumptions: i) weak lensing provides an accurate means of measuring halo masses, ii) the mean SZ and X-ray observables are related to the true halo mass through power-law relations in mass and dimensionless Hubble parameter $E(z)$ with a-priori unknown parameters, iii) there is (correlated, lognormal) intrinsic scatter and scatter due to measurement uncertainties relating these observables to their mean relations. With our multi-observable analysis pipeline, we simultaneously fit for these astrophysical modeling parameters and for cosmology. Assuming a flat $\nu\Lambda$CDM model, in which the sum of neutrino masses is a free parameter, we measure $\Omega_{\rm m} = 0.276 \pm 0.047$, $\sigma_8 = 0.781 \pm 0.037$, and the parameter combination $\sigma_8(\Omega_{\rm m}/0.3)^{0.2} = 0.766 \pm 0.025$. The redshift evolution of the X-ray $Y_{\rm X}$–mass and $M_{\rm gas}$–mass relations are both consistent with self-similar evolution to within 1σ. The mass-slope of the $Y_{\rm X}$–mass relation shows a 2.3σ deviation from self-similarity with a weak hint for an evolution with redshift. Similarly, the mass-slope of the $M_{\rm gas}$–mass relation is steeper than self-similarity at the 2.5σ level. In a νwCDM cosmology, we measure the dark energy equation of state parameter $w = -1.55 \pm 0.41$ from the cluster data, while marginalizing over the sum of neutrino masses. We perform a measurement of the growth of structure since redshift $z \sim 1.7$ and find no evidence for tension with the prediction from General Relativity. This is the first analysis of the SPT cluster sample that uses direct weak-lensing mass calibration, and is a step toward using larger weak-lensing datasets (e.g., from the Dark Energy Survey) in the near future. We provide updated redshift and mass estimates for the SPT sample.

Keywords: cosmological parameters — cosmology: observations — galaxies: clusters: general — large-scale structure of universe

1. INTRODUCTION

Measurements of the abundance of galaxy clusters have become an important part of the cosmological toolkit. Galaxy clusters and their associated dark matter halos trace the highest and therefore rarest peaks in the matter density field on megaparsec scales. To obtain cosmological constraints, one confronts the predicted halo abundance, the *halo mass function* (HMF), which is provided by numerical cosmological simulations, with the observations. The key challenge is to accurately describe the relation between halo mass in the simulations and the observable quantities. The cluster abundance essentially constrains the parameter combination $\sigma_8(\Omega_{\rm m}/0.3)^\alpha$, where σ_8 is the root mean square fluctuation in the linear matter density field on 8 Mpc/h scales

at $z = 0$ and α is of the order of about $0.2-0.4$ depending on survey specifics. Measuring the cluster abundance over a range of redshifts enables constraints on the cosmic expansion and structure formation histories. This probe can therefore be used to challenge the paradigms of a cosmological constant and of General Relativity, and, when analyzed jointly with measurements of primary anisotropies in the cosmic microwave background (CMB), to measure the sum of neutrino masses (for reviews, see, e.g., Allen et al. 2011; Kravtsov & Borgani 2012).

Cosmological analyses have been performed using samples of galaxy clusters constructed from their observed galaxy populations (e.g., Rykoff et al. 2016), their X-ray emission (e.g., Vikhlinin et al. 2009b; Mantz et al. 2010b), and their millimeter-wave signal (e.g., Bleem et al. 2015; Planck Collaboration et al. 2016b; Hilton et al. 2018). The latter is dominated by the thermal Sunyaev-Zel'dovich effect (SZ; Sunyaev & Zel'dovich 1972) which arises when CMB photons scatter off hot electrons in the intracluster medium (ICM). The surface brightness of the SZ effect is independent of cluster redshift, and high-resolution mm-wave surveys can therefore be used to construct clean and essentially mass-limited catalogs out to the highest redshifts at which clusters exist. This makes SZ-selected cluster samples particularly suited for studying the evolution of scaling relations and the growth of cosmic structure over a significant fraction of the age of the Universe.

In this paper, we present an analysis of the 2500 deg^2 SPT-SZ survey cluster sample that is enabled by optical weak gravitational lensing (WL) data for SPT-SZ clusters. The WL dataset consists of two subsamples: i) 19 clusters at intermediate redshifts $0.28 < z < 0.63$, with ground-based Magellan/Megacam imaging, referred to as the "Megacam sample" hereafter (Dietrich et al. 2017, hereafter D17); ii) 13 clusters at higher redshifts $0.58 < z < 1.13$ observed with the *Hubble Space Telescope*, referred to as the "HST sample" hereafter (Schrabback et al. 2018a, hereafter S18). Using these WL data in our analysis has two main advantages: i) it removes the need to rely on external calibrations of the observable–mass relations, ii) our analysis now only considers clusters that are actually part of the SPT-SZ sample which ensures a fully self-consistent handling of selection effects.

This work represents an improvement over the first cosmological analysis of the SZ-selected cluster sample from the full 2500 deg^2 SPT-SZ survey (de Haan et al. 2016, hereafter dH16), where we combined the cluster number counts in SZ significance and redshift with X-ray Y_X follow-up (Y_X is the product of X-ray gas mass M_{gas} and temperature T_X; Kravtsov et al. 2006) of 82 clusters. The dH16 analysis relied on external, WL-based calibrations of the normalization of the Y_X–mass relation and the assumption that its evolution in mass and redshift follows the self-similar expectation within

some uncertainty (5% and 50% uncertainty at 1σ on the parameters of the mass and redshift evolution, respectively).

As already mentioned, the key challenge in cluster cosmology is to robustly model the relation between the observables (SZ signal, WL shear profiles, X-ray Y_X measurements) and the underlying, unobserved halo mass, which is the link to the predicted HMF.[1] Our modeling assumptions are:

- The relation between true halo mass and the observed WL signal, and the scatter around this mean relation are well understood, with systematic uncertainties at the few percent level. We use numerical simulations to account for the effects of halo triaxiality, miscentering, and correlated large-scale structure along the line of sight. Uncorrelated large-scale structure along the line of sight is accounted for in a semi-analytic approach (Megacam sample) and via simulated cosmic shear fields (HST sample). For the Megacam sample, the systematic limit in mass is 5.6% (D17), and it is 9.2% for the HST sample (S18).

- The mean relations between true halo mass and the SZ and X-ray observables are described by power-law relations in mass and the dimensionless Hubble parameter $E(z) \equiv H(z)/H_0$. This functional form is motivated by the self-similar model (evolution assuming only gravity is at play; Kaiser 1986) and confirmed using numerical N-body and hydrodynamical simulations (e.g., Vanderlinde et al. 2010; de Haan et al. 2016; Gupta et al. 2017a). However, we do not assume any a-priori knowledge of the parameters in these relations and allow for departures from self-similarity by marginalizing over wide priors.

- The intrinsic scatter in the SZ and X-ray observable–mass relations is described by lognormal distributions (with a-priori unknown width). The scatter among all three observables may be correlated, and we marginalize over the correlation coefficients.

This paper is organized as follows: In Section 2, we provide an overview of the cluster dataset and of external cosmological data used in the analysis. We describe our analysis method in Section 3. In Section 4, we present our constraints on scaling relations and cosmology. We summarize our findings in Section 5 and provide some outlook. Further robustness tests are discussed in the Appendices A–C.

---

[1] Although some of the observables carry cosmological dependences themselves, we seek to constrain cosmology primarily through its impact on the HMF.

Throughout this work we assume spatially flat cosmological models. Cluster masses are referred to as $M_{\Delta c}$, the mass enclosed within a sphere of radius r_Δ, in which the mean matter density is equal to Δ times the critical density. The critical density at the cluster's redshift is $\rho_{\mathrm{crit}}(z) = 3H^2(z)/8\pi G$, where $H(z)$ is the Hubble parameter. We refer to the vector of cosmology and scaling relation parameters as $\boldsymbol{p}$.

All quoted constraints correspond to the mean and the shortest 68% credible interval, computed from the MCMC chains using a Gaussian kernel density estimator.[2] All multi-dimensional posterior probability plots show the 68% and 95% contours. We use standard notation for statistical distributions, i.e. the normal distribution with mean $\boldsymbol{\mu}$ and covariance matrix Σ is written as $\mathcal{N}(\boldsymbol{\mu}, \boldsymbol{\Sigma})$, and $\mathcal{U}(a,b)$ denotes the uniform distribution on the interval $[a,b]$.

2. DATA

The cluster cosmology sample from the 2500 deg^2 SPT-SZ survey consists of 377 candidates of which 356 are optically confirmed and have redshift measurements. X-ray follow-up measurements with *Chandra* are available for 89 clusters, and WL shear profiles are available for 19 clusters from ground-based observations with Magellan/Megacam and for 13 clusters observed from space with the *Hubble Space Telescope* (see Fig. 1).

2.1. *The SPT-SZ 2500 deg^2 Cluster Sample*

The South Pole Telescope (SPT) is a 10 m telescope located within 1 km of the geographical South Pole (Carlstrom et al. 2011). The ~1 arcmin resolution and 1 degree field of view are well suited for a survey of rare, high-mass clusters from a redshift of $z \geq 0.2$ out to the highest redshifts where they exist. From 2007 to 2011, the telescope was configured to observe with the SPT-SZ camera in three millimeter-wave bands (centered at 95, 150, and 220 GHz). The majority of this period was spent on the SPT-SZ survey, a contiguous 2500 deg^2 area within the boundaries 20h $\leq$ R.A. $\leq$ 7h and $-65° \leq$ Dec. $\leq -40°$. The survey achieved a fiducial depth of ≤ 18 μK-arcmin in the 150 GHz band.

Galaxy clusters are detected via their thermal SZ signature in the 95 and 150 GHz maps. These maps are created using time-ordered data processing and map-making procedures equivalent to those described in Vanderlinde et al. (2010); Reichardt et al. (2013). Galaxy clusters are extracted using a multi-scale matched-filter approach (Melin et al. 2006) applied to the multi-band data as described in Williamson et al. (2011); Reichardt et al. (2013).

We use the same SPT-SZ cluster sample that was analyzed in dH16. Namely, this *cosmological sample* is a subset of the full SPT-SZ cluster sample presented in
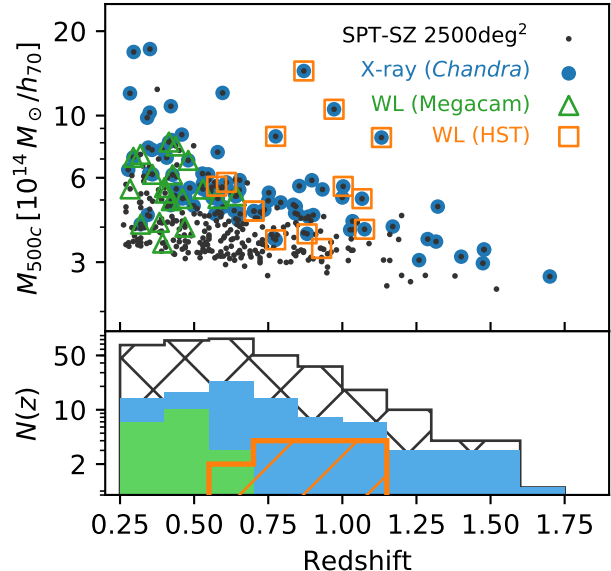
Figure 1. The SPT-SZ 2500 deg^2 cluster cosmology sample, selected to have redshift $z > 0.25$ and detection significance $\xi > 5$. *Top panel:* The distribution of clusters in redshift and mass (assuming a fiducial observable–mass relation). Black points show the full sample, blue dots mark those 89 clusters for which X-ray follow-up data from *Chandra* are available, and green triangles (orange squares) mark those 19 with Magellan/Megacam (13 with the *Hubble Space Telescope*) WL follow-up data. *Bottom panel:* Histograms with the same color coding. While the X-ray follow-up dataset covers the entire redshift range, the WL follow-up covers $0.25 < z \lesssim 1.1$.

Bleem et al. (2015), restricted to redshifts $z > 0.25$ and detection significances $\xi > 5$. This cosmological sample has an expected and measured purity of 95% (Bleem et al. 2015). For clusters at redshifts below $z = 0.25$, confusion with primary CMB fluctuations changes the scaling of the ξ–mass relation.

We have improved the cluster redshift estimates from the original values provided in Bleem et al. (2015) to incorporate both new spectroscopic measurements (Bayliss et al. 2016; Khullar et al. 2018, Mantz et al., in prep.), two updated high-redshift photo-z measurements with *Hubble Space Telescope* (Strazzullo et al. 2018), and improved photometric measurements. These improved photometric redshifts are enabled both via the recalibration of our *Spitzer* redshift models using the new spectroscopic data and by the use of optical data from the Parallel Imager for Southern Cosmology Observations (PISCO), a new imager installed on the Magellan/Clay telescope at Las Campanas Observatory (Stalder et al. 2014). PISCO—with a fast (~ 20 s) readout, 9 arcmin field-of-view, and simultaneous 4-band (*griz*) imaging capability—is optimized for efficient characterization of
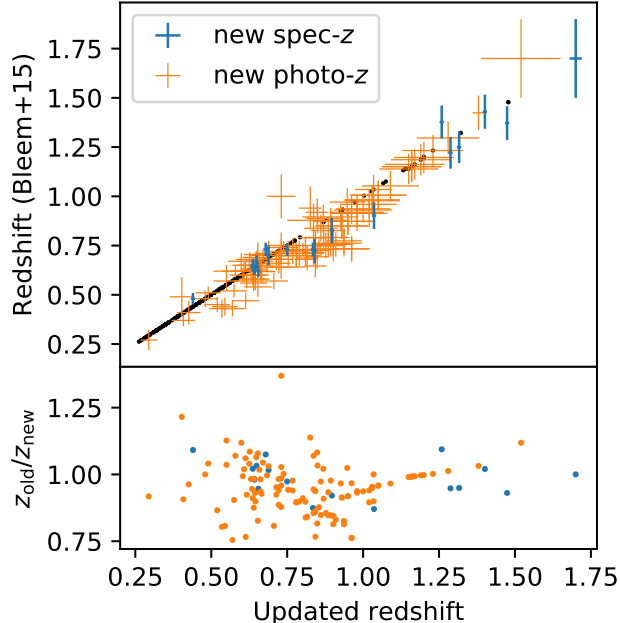
Figure 2. Updates in cluster redshifts since the publication of the SPT-SZ cluster catalog (Bleem et al. 2015). *Top panel*: Original redshifts plotted against the updated ones. Black points show unchanged redshifts (without error bars for ease of presentation), orange error bars show updated photometric redshifts, and blue error bars show new spectroscopic measurements. *Bottom panel:* Changes in redshifts; we omit unchanged redshifts and all error bars. Orange points show the change in photo-zs, blue points show changes due to new spec-z measurements.

clusters and other systems identified from external surveys. As part of further efforts to characterize the SPT-SZ cluster sample, we have obtained approximately uniform PISCO imaging for the majority of the previously confirmed SPT-SZ clusters. Notably, this deeper optical data has allowed less constraining infrared-driven redshift estimates from *Spitzer* to be replaced by more robust estimates based on optical red-sequence techniques for a significant number of clusters in the range $0.8 \lesssim z \lesssim 1$. As a consequence, while the improved data and model calibration results in small changes in redshift estimates for systems at $z \lesssim 0.8$ and $z \gtrsim 1$, at intermediate redshifts, replacing infrared-driven redshifts with more robust optical estimates leads to up to 1.5σ systematic shifts, see Fig. 2. We will briefly come back to this issue in Section 4.3.

2.2. *X-ray Measurements*

We use X-ray measurements for a subsample of 89 clusters. Eighty-one of these were also used in our previous cosmological analysis (dH16). Most of those X-ray measurements were originally presented in McDonald et al. (2013), and they were largely acquired through

a *Chandra* X-ray Visionary Project (PI: Benson). This sample is now supplemented with observations of 8 high-redshift $z > 1.2$ clusters (McDonald et al. 2017). We refer the reader to these references for the details of the X-ray analysis.

The X-ray data products entering this analysis are: i) lookup tables of the total gas mass, M_{gas} within an outer radius ranging from $80 - 2000$ kpc (calculated using a fiducial cosmology), allowing interpolation of M_{gas} within any realistic value of r_{500}, and ii) spectroscopic temperatures, T_{X}, in the $0.15 - 1.0 \, r_{500}$ aperture. All X-ray measurements were re-made for this work using the *Chandra* calibration CALDB v4.7.7.

2.3. *Weak Gravitational Lensing Data*

We use WL measurement for 32 clusters in our sample. Of these, 19 were observed with Magellan/Megacam at redshifts $0.29 \leq z \leq 0.69$ (D17), and 13 at redshifts $0.576 \leq z \leq 1.132$ with the Advanced Camera for Surveys onboard the *Hubble Space Telescope* (S18). Details on the data reduction and analysis methods can be found in these works.

The data products from these works used in our analysis are the reduced tangential shear profiles in angular coordinates, corrected for contamination by cluster galaxies, and the estimated redshift distributions of the selected source galaxies. These are the observable quantities, which are independent from cosmology, whereas mass estimates or shear profiles in physical coordinates depend on cosmology through the redshift distance relation and the cosmology dependence of the NFW profile. Our approach ensures a clean separation between the actual measurements and their modeling.

2.4. *External Cosmological Data Sets*

In addition to our cluster dataset, we will also consider external cosmological probes. We use measurements of primary CMB anisotropies from *Planck* and focus on the TT+lowTEB data combination from the 2015 analysis (Planck Collaboration et al. 2016a). We use angular diameter distances as probed by Baryon Acoustic Oscilations (BAO) by the 6dF Galaxy Survey (Beutler et al. 2011), the SDSS Data Release 7 Main Galaxy Sample (Ross et al. 2015), and the BOSS Data Release 12 (Alam et al. 2017). We also use measurements of luminosity distances from Type Ia supernovae from the Pantheon sample (Scolnic et al. 2018).

3. ANALYSIS METHOD

In this section, we present the observable–mass relations, the likelihood function, and the priors adopted. Fig. 3 shows a flowchart of the analysis pipeline. The data and likelihood code will be made publicly available.

3.1. *Observable–mass Relations*

We consider three cluster mass proxies: the unbiased SZ significance ζ, the X-ray Y_{X}, and the WL mass M_{WL}.

We parametrize the observable–mass relations as

$$\zeta = A_{\rm SZ} \left(\frac{M_{500c}\, h_{70}}{4.3 \times 10^{14} M_\odot} \right)^{B_{\rm SZ}} \left(\frac{E(z)}{E(0.6)} \right)^{C_{\rm SZ}} \qquad (1)$$

$$\frac{M_{500c}\, h_{70}}{8.37 \times 10^{13} M_\odot} = A_{Y_{\rm X}} \left(\frac{Y_{\rm X} h_{70}^{5/2}}{3 \times 10^{14} M_\odot\, {\rm keV}} \right)^{B_{Y_{\rm X}}} \\ \times E(z)^{C_{Y_{\rm X}}} \qquad (2)$$

$$M_{\rm WL} = b_{\rm WL} M_{500c}. \qquad (3)$$

The ζ–mass and $Y_{\rm X}$–mass relations are equivalent to the ones adopted in dH16, except for replacing $h/0.72$ by h_{70} in $Y_{\rm X}$–mass. The intrinsic scatters in $\ln \zeta$ and $\ln Y_{\rm X}$ at fixed mass and redshift are assumed to be normal with widths $\sigma_{\ln \zeta}$ and $\sigma_{\ln Y_{\rm X}}$, respectively, that are independent of mass and redshift. Note that these parameters have been called $D_{\rm SZ}$ and $D_{\rm X}$ in some previous SPT publications. The scatter in $M_{\rm WL}$ is described by a log-normal component $\sigma_{\rm WL_{local}}$ due to the NFW modeling of the halo, and a normal component $\sigma_{\rm WL_{LSS}}$ due to uncorrelated large-scale structure (more details below in Section 3.1.2).

We allow for correlated scatter between the SZ, X-ray, and WL mass proxies by allowing for non-zero correlation coefficients $\rho_{\rm SZ-X}$, $\rho_{\rm SZ-WL}$, and $\rho_{\rm WL-X}$ that link $\sigma_{\ln \zeta}$, $\sigma_{\ln Y_{\rm X}}$, and $\sigma_{\rm WL_{local}}$. All parameters are listed in Table 2.

While our default X-ray observable is $Y_{\rm X}$, we also consider the X-ray gas mass $M_{\rm gas}$. Note that both observables share the same $M_{\rm gas}$ data, and so we do not use them simultaneously. We define a relation for the gas mass fraction $f_{\rm gas} \equiv M_{\rm gas}/M_{500c}$

$$f_{\rm gas} = h_{70}^{-3/2} A_{f_{\rm g}} \left(\frac{M_{500c}\, h_{70}}{5 \times 10^{14} M_\odot} \right)^{B_{M_{\rm g}}-1} \left(\frac{E(z)}{E(0.6)} \right)^{C_{M_{\rm g}}} \qquad (4)$$

with which the $M_{\rm gas}$–mass relation becomes

$$\frac{M_{\rm gas}}{5 \times 10^{14} M_\odot} = h_{70}^{-5/2} A_{f_{\rm g}} \left(\frac{M_{500c}\, h_{70}}{5 \times 10^{14} M_\odot} \right)^{B_{M_{\rm g}}} \\ \times \left(\frac{E(z)}{E(0.6)} \right)^{C_{M_{\rm g}}}. \qquad (5)$$

3.1.1. The SZ ξ–mass Relation

The observable we use to describe the cluster SZ signal is ξ, the detection signal-to-noise ratio (SNR) maximized over all filter scales. To account for the impact of noise bias, the *unbiased* SZ significance ζ is introduced, which is the SNR at the true, underlying cluster position and filter scale (Vanderlinde et al. 2010). Following previous SPT work, the average ξ across many noise realizations is related to ζ as

$$\langle \xi \rangle^2 = \zeta^2 + 3 \qquad (6)$$

with a Gaussian scatter of unit width. In practice, we only map objects with $\zeta > 2$ to ξ using this relation, but the exact location of this cut has no impact on our results (see also dH16). The validity of this approach and of Eq. 6 has been extensively tested and confirmed by analyzing simulated SPT observations of mock SZ maps (Vanderlinde et al. 2010).

The SPT-SZ survey consists of 19 fields that were observed to different depths. The varying noise levels only affect the normalization of the ζ–mass relation, and leave $B_{\rm SZ}$, $C_{\rm SZ}$, and $\sigma_{\ln \zeta}$ effectively unchanged (dH16). In the analysis presented here, $A_{\rm SZ}$ is rescaled by a correction factor for each of the 19 fields, which then allows us to work with a single SZ observable–mass relation, given by Eq. 1. The scaling factors $\gamma_{\rm field}$ can be found in Table 1 in dH16.

In a departure from previous SPT analyses, we do not apply informative (Gaussian) priors on the SZ scaling relation parameters. The self-calibration through fitting the cluster sample against the halo mass function, (see, e.g., Majumdar & Mohr 2004), the constraint on the normalization of the observable–mass relations through our WL data, and the constraint on the SZ scatter through the X-ray data are strong enough to constrain all four SZ scaling relation parameters (in $\nu\Lambda$CDM, see Table 3). When not including the X-ray data in our fit, however, we apply a Gaussian prior $\sigma_{\ln \zeta} = 0.13 \pm 0.13$ as in dH16 (this constraint was extracted from mock observations of hydrodynamic simulations from Le Brun et al. 2014).

We discuss possible limitations in our description of the ξ–mass relation that would lead to systematic biases in the recovered cosmological constraints. Because of our empirical weak-lensing mass calibration and the parametrization of the SZ scaling relation by power laws and lognormal scatter with free parameters, any bias in the SZ–mass relation that can be described by a power law and/or lognormal scatter would only lead to parameter shifts in the SZ scaling relation, but would not affect *cosmological* parameter constraints. Therefore, important systematics would be from potential contaminants that would lead to an additional, non-lognormal scatter, a mass or redshift dependence in the scatter, or a redshift dependence of the mass-slope.

A potential worry might be the dilution of the SZ signal by AGN activity and the presence of dusty star-forming galaxies in the cluster. Various studies have found that emission by dusty star-forming galaxies is negligible compared to the SZ signal (see, e.g., Lin et al. (2009); Sehgal et al. (2010) and the summary in Section 6.4 in Benson et al. (2013)). Gupta et al. (2017b) measured the cluster radio luminosity function using an X-ray selected cluster sample at $z \lesssim 0.7$ and concluded that radio sources obeying this luminosity function would not have a strong impact on the SZ signal. Only a few percent at most of the SPT-SZ clusters would host sufficiently bright radio sources for their SZ signal to drop below the selection threshold, and this is

within the Poisson uncertainty of our sample. At higher redshifts, it has been previously measured that the radio fraction in optically selected clusters somewhat decreases at $z > 0.65$ (Gralla et al. 2011). This result is consistent with simulations of the microwave sky from Sehgal et al. (2010), which predicted that the amount of radio contamination in SZ surveys was either flat or falling at $z > 0.8$. Using tests against mocks, we find for example that, to cause a shift in w by more than $\Delta(w) = -0.3$, the level of SZ contamination would have to be strong enough to remove more than $\sim 30\%$ of all cluster detections at redshifts $z \gtrsim 1$, which by far exceeds the measurement by Gupta et al. (2017b). In conclusion, none of the discussed sources of potential SZ cluster contamination have an impact that is strong enough to introduce large biases in our cosmological constraints.

Another approach to testing the robustness of the SZ observable–mass relation is to compare it with other cluster mass proxies, and to try and find deviations from the simple scaling relation model. Note that, if such a deviation was found, it would be hard to discern which observable is behaving in an unexpected way, but importantly, one would learn that the multi-observable model needs an extension. At low and intermediate redshifts $z \lesssim 0.8$, comparisons with cluster samples selected through optical and X-ray methods have shown that the cluster populations can be described by power-law observable–mass scaling relations with lognormal intrinsic scatter (Vikhlinin et al. 2009a; Mantz et al. 2010a; Saro et al. 2015; Mantz et al. 2016; Saro et al. 2017). At higher redshifts, the subset of the SPT selected sample with available X-ray observations from *Chandra* and *XMM-Newton* exhibit scaling relations in X-ray $T_{\rm X}$, $Y_{\rm X}$, $M_{\rm gas}$, and $L_{\rm X}$ as well as in stellar mass galaxies, that are consistent with power-law relations in mass and redshift with lognormal intrinsic scatter (Chiu et al. 2016; Hennig et al. 2017; Chiu et al. 2018; Bulbul et al. 2018). When a redshift dependent mass slope parameter has been included in the analyses of these datasets, the parameter constraints have been statistically consistent with 0 in all cases (see Table 4 in Bulbul et al. 2018).

In conclusion, our description of the ξ–mass relation has been confirmed by various independent techniques, especially for redshifts $z \lesssim 1$. Note that these tests are harder to perform at higher redshifts where non-SZ selected samples are small and more challenging to characterize. Our expectation is that as the cluster sample grows larger and the mass calibration information improves that we will be able to characterize the currently negligible departures from our scaling relation model. At that point, we will need to extend our observable–mass relation to allow additional freedom.

3.1.2. *The Weak-Lensing observable–mass Relation*

Table 1. WL modeling parameters (D17; S18). The *WL mass bias* and the local (lognormal) component of the *intrinsic scatter* are calibrated against N-body simulations. Among other effects, they also account for the uncertainty and the scatter in the $c(M)$ relation. This is done separately for each cluster in the HST sample leading to a range of values; here we report the smallest and largest individual values. The *mass modeling uncertainty* accounts for uncertainties in the calibration against N-body simulations and in the centering distribution. The *systematic measurement uncertainties* account for a multiplicative shear bias and the uncertainty in estimating the redshift distribution of source galaxies. *Uncorrelated large-scale structure* along the line of sight leads to an additional, Gaussian scatter.

| Effect | Impact on Mass | |
	Megacam	HST
WL mass bias	0.938	$0.81 - 0.92$
Intrinsic scatter	0.214	$(0.26 - 0.42)$
Δ(intrinsic scatter)	0.04	$0.021 - 0.055$
Uncorr. LSS scatter $[M_\odot]$	9×10^{13}	8×10^{13}
Δ(Uncorr. LSS scatter) $[M_\odot]$	10^{13}	10^{13}
Mass modeling uncertainty	4.4%	$5.8 - 6.1\%$
Systematic measurement uncert.	3.5%	7.2%
Total systematic uncertainty	5.6%	$9.2 - 9.4\%$

The WL modeling framework used in this work is introduced in D17, and we refer the reader to their Section 5.2 for details.

The WL observable is the reduced tangential shear profile $g_{\rm t}(\theta)$, which can be analytically modeled from the halo mass M_{200c}, assuming an NFW halo profile and using the redshift distribution of source galaxies (Wright & Brainerd 2000). Miscentering, halo triaxiality, large-scale structure along the line of sight, and uncertainties in the concentration–mass relation, introduce bias and/or scatter. As introduced in Eq. 3, we assume a relation $M_{\rm WL} = b_{\rm WL} M_{\rm true}$, and use numerical simulations to calibrate the normalization $b_{\rm WL}$ and the scatter about the mean relation. Our WL dataset consists of two subsamples (Megacam and HST) with different measurement and analysis schemes. We expect some systematics to be shared among the entire sample, while others will affect each subsample independently.

We model the WL bias as

$$
\begin{aligned}
b_{{\rm WL},i} = &\, b_{{\rm WL\ mass},i} \\
&+ \delta_{\rm WL, bias}\, \Delta b_{{\rm mass\ model},i} \\
&+ \delta_i\, \Delta b_{{\rm Measurement\ systematics},i}, \\
&\quad i \in \{{\rm Megacam,\ HST}\},
\end{aligned}
\tag{7}
$$

where $b_{\rm WL\ mass}$ is the mean bias due to WL mass modeling, $\Delta b_{\rm WL\ mass\ model}$ is the uncertainty on $b_{\rm WL\ mass}$,

and $\Delta b_{\text{Measurement systematics}}$ is the systematic measurement uncertainty due to multiplicative shear bias and uncertainties in the determination of the source redshift distribution; $\delta_{\text{WL,bias}}$, δ_{Megacam}, and δ_{HST} are free parameters in our likelihood. With this parametrization, we apply Gaussian priors $\mathcal{N}(0,1)$ on the three fit parameters. The numerical values of the different components of the WL bias are given in Table 1.

The (lognormal) scatter that is intrinsic to fitting WL shear profiles against NFW profiles is

$$\sigma_{\text{WL},i} = \sigma_{\text{intrinsic},i} + \delta_{\text{WL,scatter}}\, \Delta\sigma_{\text{intrinsic},i}, \quad (8)$$
$$i \in \{\text{Megacam, HST}\},$$

where $\sigma_{\text{intrinsic}}$ and $\Delta\sigma_{\text{intrinsic}}$ are the mean intrinsic scatter and the error on the mean (given in Table 1); $\delta_{\text{WL,scatter}}$ is a free parameter in our likelihood on which we apply a Gaussian prior $\mathcal{N}(0,1)$.

Finally, the (normal) scatter due to uncorrelated large-scale structure is

$$\sigma_{\text{WL,LSS},i} = \sigma_{\text{LSS},i} + \delta_{\text{WL,LSS},i}\, \Delta\sigma_{\text{LSS},i}, \quad (9)$$
$$i \in \{\text{Megacam, HST}\},$$

with the mean scatter σ_{LSS} and the error on the mean $\Delta\sigma_{\text{LSS}}$ given in Table 1 and where we apply a Gaussian prior $\mathcal{N}(0,1)$ on the fit parameters $\delta_{\text{WL,LSS}_{\text{Megacam}}}$ and $\delta_{\text{WL,LSS}_{\text{HST}}}$.

For reference, the total systematic error in the WL calibration is 5.6% for the Megacam sample (D17) and 9.2% for the HST sample (S18). Given the small sample size of 19 and 13 clusters, our WL mass calibration is still dominated by statistical errors.

3.2. Likelihood Function

The analysis pipeline used in this work evolved from the code originally used in a previous SPT analysis (Bocquet et al. 2015). Since then, we have updated it to the full 2500 deg² survey, included the handling of WL data and the ability to account for correlated scatter among all observables, and modified the X-ray analysis (see Section 3.2.2). The pipeline is written as a module for CosmoSIS (Zuntz et al. 2015) and was also used for other WL scaling relation studies of SPT-SZ clusters (D17; Stern et al. 2018).

We start from a multi-observable Poisson log-likelihood

$$\ln\mathcal{L}(\boldsymbol{p}) = \sum_i \ln \frac{dN(\xi, Y_{\text{X}}, g_{\text{t}}, z | \boldsymbol{p})}{d\xi\, dY_{\text{X}}\, dg_{\text{t}}\, dz}\Big|_{\xi_i, Y_{\text{X}_i}, g_{\text{t}_i}, z_i}$$
$$- \iiiint d\xi\, dY_{\text{X}}\, dg_{\text{t}}\, dz\, [\quad\quad (10)$$
$$\frac{dN(\xi, Y_{\text{X}}, g_{\text{t}}, z | \boldsymbol{p})}{d\xi\, dY_{\text{X}}\, dg_{\text{t}}\, dz}\Theta_{\text{s}}\,]$$
$$+ \text{const.}$$

where the sum runs over all clusters i in the sample, and Θ_{s} is the survey selection function; in our case $\Theta_{\text{s}} = \Theta(\xi > 5, z > 0.25)$.

As discussed in Bocquet et al. (2015) and explicitly shown in their Appendix, we rewrite the first term in Eq. 10 as $P(Y_{\text{X}}, g_{\text{t}} | \xi_i, z_i, \boldsymbol{p})\big|_{Y_{\text{X}_i}, g_{\text{t}_i}} \times \frac{dN(\xi, z | \boldsymbol{p})}{d\xi dz}\big|_{\xi_i, z_i}$. The second term in Eq. 10 represents the total number of clusters in the survey, which are selected in ξ and z (and without any selection based on the follow-up observables). Therefore, this term reduces to $\int d\xi dz \Theta_{\text{s}} dN(\xi, z | \boldsymbol{p})/d\xi dz$. With these modifications, and after explicitly setting the survey selection, the likelihood function becomes

$$\ln\mathcal{L}(\boldsymbol{p}) = \sum_i \ln \frac{dN(\xi, z | \boldsymbol{p})}{d\xi dz}\Big|_{\xi_i, z_i}$$
$$- \int_{z_{\text{cut}}}^{\infty} dz \int_{\xi_{\text{cut}}}^{\infty} d\xi \frac{dN(\xi, z | \boldsymbol{p})}{d\xi dz} \quad (11)$$
$$+ \sum_j \ln P(Y_{\text{X}}, g_{\text{t}} | \xi_j, z_j, \boldsymbol{p})\big|_{Y_{\text{X}_j}, g_{\text{t}_j}}$$

up to a constant. The first sum runs over all clusters i in the sample, and the second sum runs over all clusters j with Y_{X} and/or WL g_{t} measurements.

The first two terms in Eq. 11 can be interpreted as the likelihood of the abundance (or number counts) of SZ clusters, while the third term represents the information from follow-up mass calibration. These two components are also visualized in the analysis flowchart in Fig. 3: the number counts on the lower left side use the distribution of clusters in (ξ, z) space, and the mass calibration on the lower right also uses all available WL and X-ray follow-up data.

3.2.1. Implementation of the Likelihood Function

We compute the individual terms in Eq. 11 as follows.

$$\frac{dN(\xi, z | \boldsymbol{p})}{d\xi dz} = \iint dM\, d\zeta\, [\ P(\xi|\zeta)P(\zeta|M, z, \boldsymbol{p})$$
$$\frac{dN(M, z | \boldsymbol{p})}{dM dz}\Omega(z, \boldsymbol{p})\ ] \quad (12)$$

where $\Omega(z, \boldsymbol{p})$ is the survey volume and $dN(M, z | \boldsymbol{p})/dM dz$ is the HMF. We evaluate Eq. 12 in the space (ξ, z) by convolving the HMF with the intrinsic scatter in $P(\zeta|M, z, \boldsymbol{p})$ and the measurement uncertainty in $P(\xi|\zeta)$.

The first term in Eq. 11 is computed by evaluating Eq. 12 at each cluster's measured (ξ_i, z_i), marginalizing over photometric redshift errors where present. The second term is a simple two-dimensional integral over Eq. 12.

Our cluster sample contains 21 SZ detections for which no optical counterparts were found; these were assigned lower redshift limits z_{lim} in Bleem et al. (2015). We used simulations to determine the expected false-detection rate $dN_{\text{false}}(\xi)/d\xi$ given survey specifics (see Section 2.2
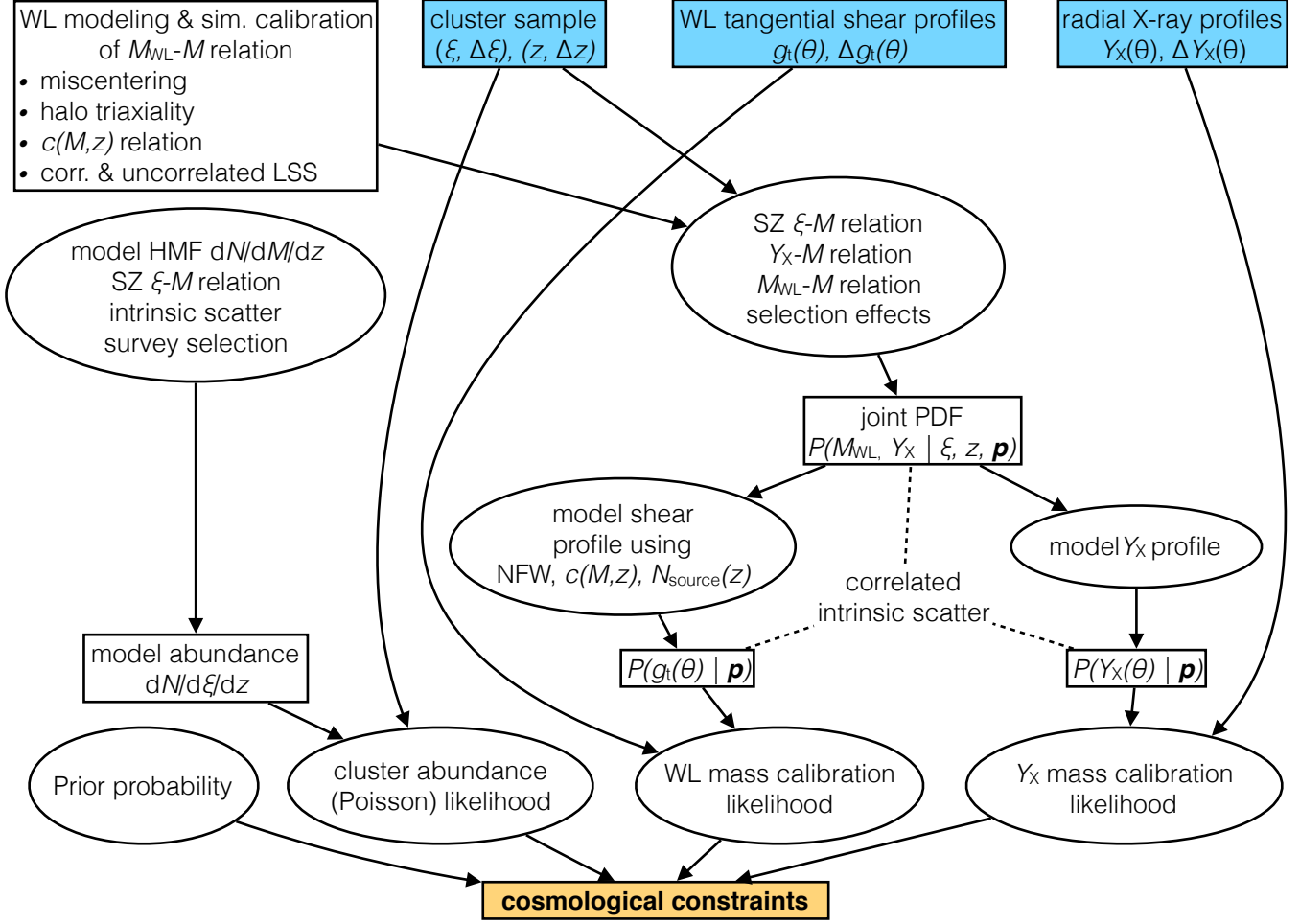
Figure 3. Analysis flowchart showing how the cluster data (blue boxes) are used to obtain cosmological constraints (orange box). White boxes show model predictions, ellipses show functions that use or create those models. The number count analysis is performed using the full SPT-SZ catalog, while the mass calibration is performed using the subset of clusters for which follow-up data is available.

and Table 1 in dH16). For each unconfirmed cluster candidates, we evaluate a modified version of the first term in Eq. 11

$$\frac{dN_{\text{unconf. cand.}}(\xi, z|\boldsymbol{p})}{d\xi dz} = \frac{dN_{\text{cluster}}(\xi, z|\boldsymbol{p})}{d\xi dz} + \frac{dN_{\text{false}}(\xi)}{d\xi} \quad (13)$$

and marginalize over the candidate's allowed redshift range $z_{\text{lim}} < z < \infty$. Note that the total expected number of false detections $\int d\xi dN_{\text{false}}(\xi)/d\xi$ is independent of $\boldsymbol{p}$ and is therefore neglected in Eq. 11. The expected number of false detections in the SPT-SZ survey is 18±4, which is consistent with our 21 unconfirmed candidates (dH16). In practice, we obtain essentially unchanged results if we simply discard the 21 optically-unconfirmed SZ detections from the catalog.

The mass calibration term in Eq. 11 is computed as

$$P(Y_{\text{X}}^{\text{obs}}, g_{\text{t}}^{\text{obs}}|\xi, z, \boldsymbol{p}) =$$
$$\iiiint dM \, d\zeta \, dY_{\text{X}} \, dM_{\text{WL}} \, [\quad (14)$$
$$P(Y_{\text{X}}^{\text{obs}}|Y_{\text{X}})P(g_{\text{t}}^{\text{obs}}|M_{\text{WL}})P(\xi|\zeta)$$
$$P(\zeta, Y_{\text{X}}, M_{\text{WL}}|M, z, \boldsymbol{p})P(M|z, \boldsymbol{p}) \,]$$

with the HMF $P(M|z, \boldsymbol{p})$ and the multi-observable scaling relation $P(\zeta, Y_{\text{X}}, M_{\text{WL}}|M, z, \boldsymbol{p})$ that includes the effects of correlated scatter. Computing this multi-dimensional integral in the $(\zeta, Y_{\text{X}}, M_{\text{WL}})$ space is expensive. We minimize the computational cost of this step by i) only considering parts of the $(\zeta, Y_{\text{X}}, M_{\text{WL}})$ space that have non-negligible probability densities; we estimate this sub-space from the measurements and $\boldsymbol{p}$, ii) using Fast Fourier Transform convolutions, and iii) only performing this computation for clusters that actually have both follow-up measurements Y_{X} and M_{WL}; other-

wise, we restrict the computation to the much cheaper two-dimensional (Y_X, ζ) or (M_{WL}, ζ) spaces. The mass calibration term does not need to be computed at all for clusters that have no X-ray or WL follow-up data.

3.2.2. *Update of the X-ray Analysis Scheme*

The X-ray observable is a measurement of the radial Y_X profile. The scaling relation on the other hand predicts a value of the observable integrated out to r_{500} for a given M_{500}. In a self-consistent analysis, the likelihood should be extracted by comparing the data and the model prediction at the same radius.

In previous SPT analyses, a Y_X value was extracted from the profile by iteratively solving for the radius r_{iter} at which the measured Y_X and the X-ray scaling relation prediction from Eq. 2 match (the scaling relation is evaluated at $M_{500} \equiv 4\pi/3 r_{iter}^3 500\rho_c$). This iteration was repeated for each set of parameters $\boldsymbol{p}$, but within a fixed reference cosmology. However, this method introduces a bias, because r_{iter} is not equal to the radius r_{500} at which the scaling relation $P(\zeta, Y_X, M_{WL}|M_{500}, z, \boldsymbol{p})$ in Eq. 14 is evaluated.

We choose a different approach, and evaluate both the (integrated) measured profile and the model prediction at a fixed fiducial radius r_{fid}. We define r_{fid} for each cluster by computing $r_{500,fid}$ from its SZ significance ξ using a fiducial set of SZ scaling relation parameters, and setting $r_{fid} = r_{500,fid}$. Then, for each set of parameters $\boldsymbol{p}$ in the analysis, we convert the model prediction $Y_X(r_{500})$ from radius r_{500} to r_{fid}. We use the fact that the radial profiles are well-approximated by power laws in radius

$$\frac{Y_X(r)}{Y_X(r_{500})} = \left(\frac{r}{r_{500}}\right)^{d\ln Y_X/d\ln r} \quad (15)$$

where r_{500} is derived from M_{500c}. In our analysis, we assume isothermality (see Section 2.2), and so $d\ln Y_X/d\ln r$ equals the radial slope in gas mass $d\ln M_g/d\ln r$. From our sample we measure

$$d\ln M_g/d\ln r = 1.12 \pm 0.23. \quad (16)$$

We are now able to make a model prediction at r_{fid}, starting from the scaling relation prediction $Y_X(r_{500})$:

$$Y_X(r_{fid}) = Y_X(r_{500}) \left(\frac{r_{fid}}{r_{500}}\right)^{d\ln M_g/d\ln r}. \quad (17)$$

In the analysis, we marginalize over the uncertainty in $d\ln M_g/d\ln r$, which shows negligible correlation with any other parameter. Note that this prescription for the model prediction $Y_X(r_{fid})$ contains an additional dependence on r_{500} and thus on M_{500}.

We note that a similar approach was adopted by other groups (e.g. Mantz et al. 2010a, 2015). We have shown through tests against mock catalogs that the new analysis scheme is unbiased, and that the previous method biased B_{Y_X} low at a level that is comparable to the uncertainty on that parameter, while the effect on other parameters was very small.

3.3. *The Halo Mass Function*

We assume the HMF fit by Tinker et al. (2008). This approach assumes universality of the HMF across the cosmological parameter space considered in this work, and uses a fitting function that was calibrated against N-body simulations. In principle, the HMF is also affected by baryonic effects. However, hydrodynamic simulations suggest that these have negligible impact for clusters with masses as high as those considered here (Velliscig et al. 2014); this was explicitly tested for a simulated and idealized SPT-SZ cluster survey (Bocquet et al. 2016). Finally, note that the Tinker et al. (2008) fit applies to *mean* spherical overdensities in the range $200 \leq \Delta_{mean} \leq 3200$, and we thus convert to $\Delta_{500crit}$ using $\Delta_{mean}(z) = 500/\Omega_m(z)$. As the HMF fit is only calibrated up to $\Delta_{mean} = 3200$, we require $\Omega_m(z) \geq 500/3200 = 0.15625$ for all redshifts $z \geq 0.25$ relevant for our cluster sample.

3.4. *Pipeline Validation on Mock Data*

We have run extensive tests to ensure that our analysis pipeline is unbiased at a level that is much smaller than our total error budget. The primary approach is testing against mock catalogs. Of course such tests are only useful if producing mocks is easier and more reliable than the actual analysis. In our case, the analysis is challenging mainly because of the computation of multi-dimensional integrals. To create one of our mocks on the other hand, one has to compute the halo mass function, apply the observable–mass relations, draw random deviates, and compute WL shear profiles. Using the same code to compute the HMF for the mocks and the analysis would undercut the usefulness of the testing, and so we also created mocks using HMFs computed with independent code. For the same reason, the mock shear profiles were created using independent code. We typically create mock catalogs that contain an order of magnitude more clusters and calibration data than our real sample. We created and analyzed sets of mocks using different random seeds and different sets of input parameters (notably, some with $w \neq -1$). No test indicated any biases in our analysis pipeline at the level relevant for our data set.

3.5. *Quantifying Posterior Distribution (Dis-)Agreement*

We characterize the agreement between constraints obtained from pairs of probes (e.g., clusters and primary CMB anisotropies) by quantifying whether the difference between the two posterior distributions is consistent with zero difference. We draw representative samples $[\boldsymbol{x_1}]$ and $[\boldsymbol{x_2}]$ from the posteriors of the two probes $P_1(\boldsymbol{x})$ and $P_2(\boldsymbol{x})$, compute the difference between all pairs of points $\boldsymbol{\delta} \equiv \boldsymbol{x_1} - \boldsymbol{x_2}$ and then construct the probability distribution D from the ensemble $[\boldsymbol{\delta}]$. The probability value (or p-value) that the two distributions

represent the same underlying quantity is

$$p = \int\limits_{D < D(0)} d\boldsymbol{\delta} D(\boldsymbol{\delta}) \qquad (18)$$

where $D(\mathbf{0})$ is the probability of zero difference. The p-value can be converted into a significance assuming Gaussian statistics. This measure can be applied to one-dimensional and multi-dimensional parameter spaces. The code is publicly available.[3]

3.6. *Parameter Priors and Likelihood Sampling*

In our cosmological fits, we assume spatial flatness and allow the sum of neutrino masses to vary. The comparison of our results with constraints from primary CMB anisotropies is of prime interest—notably, the comparison of constraints on σ_8. For primary CMB anisotropies, σ_8 is strongly degenerate with $\sum m_\nu$ and so the latter should be a free parameter of the model to avoid artificially tight constraints. We refer to the flat ΛCDM model with a varying sum of neutrino masses as $\nu\Lambda$CDM, and to its extension with a free dark energy equation of state parameter as νwCDM.

In the $\nu\Lambda$CDM cosmology, we vary the cosmological parameters $\Omega_{\rm m}$, $\Omega_\nu h^2$, $\Omega_{\rm b} h^2$, A_s, h, n_s; σ_8 is a derived parameter. Our cluster data primarily constrain $\Omega_{\rm m}$ and σ_8, and we marginalize over flat priors on the other parameters. The parameter ranges for $\Omega_{\rm b} h^2$ and n_s are chosen to roughly match the 5σ credibility interval of the *Planck* constraints; h is allowed to vary in the range $0.55 \ldots 0.9$. We assume two massless and one massive neutrino and allow $\Omega_\nu h^2$ to vary in the range $0 \ldots 0.01$; this corresponds to a range in $\sum m_\nu$ of $0 \ldots 0.93$ eV. We note that the minimum allowed sum of neutrino masses from oscillation experiments is $\sum m_\nu > 59.5 \pm 0.5$ meV (Tanabashi et al. 2018). In a departure from previous SPT analyses, we do not apply a BBN prior on $\Omega_{\rm b} h^2$ or constraints from direct measurements of H_0. We remind the reader that the implementation of the theory HMF leads to an effective, hard prior $\Omega_{\rm m}(z) \gtrsim 0.16$ for all redshifts $z > 0.25$ relevant to our survey (see Section 3.3); however, this prior does not affect our results. All parameters and their priors are summarized in Table 2.

The likelihood sampling is done within CosmoSIS using the Metropolis (Metropolis et al. 1953) and MultiNest (Feroz et al. 2009) samplers. We confirmed that they produce consistent results.

4. RESULTS

Our fiducial results are obtained from the SPT-selected clusters with their detection significances and redshifts, together with the WL and X-ray follow-up data where available. We refer to this dataset as SPTcl (SPT-SZ+WL+$Y_{\rm X}$).

---

[3] https://github.com/SebastianBocquet/PosteriorAgreement

Table 2. Summary of cosmological and astrophysical parameters used in our fiducial analysis. The Gaussian prior on $\sigma_{\ln\zeta}$ is only applied when no X-ray data is included in the fit. The parameter ranges for $\Omega_{\rm b} h^2$ and n_s are chosen to roughly match the 5σ interval of the *Planck* ΛCDM results. w is fixed to -1 for ΛCDM, and is allowed to vary for wCDM. The optical depth to reionization τ is only relevant when *Planck* data is included in the analysis. The WL modeling systematics are presented in Table 1.

Parameter	Prior
Cosmological	
$\Omega_{\rm m}$	$\mathcal{U}(0.05, 0.6)$, $\Omega_{\rm m}(z > 0.25) > 0.156$
$\Omega_{\rm b} h^2$	$\mathcal{U}(0.020, 0.024)$
$\Omega_\nu h^2$	$\mathcal{U}(0, 0.01)$
Ω_k	fixed (0)
A_s	$\mathcal{U}(10^{-10}, 10^{-8})$
h	$\mathcal{U}(0.55, 0.9)$
n_s	$\mathcal{U}(0.94, 1.00)$
w	fixed (-1) or $\mathcal{U}(-2.5, -0.33)$
Optical depth to reionization	
τ	fixed or $\mathcal{U}(0.02, 0.14)$
SZ scaling relation	
$A_{\rm SZ}$	$\mathcal{U}(1, 10)$
$B_{\rm SZ}$	$\mathcal{U}(1, 2.5)$
$C_{\rm SZ}$	$\mathcal{U}(-1, 2)$
$\sigma_{\ln\zeta}$	$\mathcal{U}(0.01, 0.5)$ $(\times \mathcal{N}(0.13, 0.13^2))$
X-ray $Y_{\rm X}$ scaling relation	
$A_{Y_{\rm X}}$	$\mathcal{U}(3, 10)$
$B_{Y_{\rm X}}$	$\mathcal{U}(0.3, 0.9)$
$C_{Y_{\rm X}}$	$\mathcal{U}(-1, 0.5)$
$\sigma_{\ln Y_{\rm X}}$	$\mathcal{U}(0.01, 0.5)$
$d\ln M_{\rm g}/d\ln r$	$\mathcal{U}(0.4, 1.8) \times \mathcal{N}(1.12, 0.23^2)$
WL modeling	
$\delta_{\rm WL,bias}$	$\mathcal{U}(-3, 3) \times \mathcal{N}(0, 1)$
$\delta_{\rm Megacam}$	$\mathcal{U}(-3, 3) \times \mathcal{N}(0, 1)$
$\delta_{\rm HST}$	$\mathcal{U}(-3, 3) \times \mathcal{N}(0, 1)$
$\delta_{\rm WL,scatter}$	$\mathcal{U}(-3, 3) \times \mathcal{N}(0, 1)$
$\delta_{\rm WL,LSS_{Megacam}}$	$\mathcal{U}(-3, 3) \times \mathcal{N}(0, 1)$
$\delta_{\rm WL,LSS_{HST}}$	$\mathcal{U}(-3, 3) \times \mathcal{N}(0, 1)$
Correlated scatter	
$\rho_{\rm SZ-WL}$	$\mathcal{U}(-1, 1)$
$\rho_{\rm SZ-X}$	$\mathcal{U}(-1, 1)$
$\rho_{\rm X-WL}$	$\mathcal{U}(-1, 1)$
	$\det(\boldsymbol{\Sigma}) > 0$

Table 3. Constraints on a subset of cosmological and scaling relation parameters. SPTcl stands for the SPT-SZ+WL+$Y_{\rm X}$ dataset, and *Planck* refers to the TT+lowTEB data. The cluster-based posterior distributions for h and $\sum m_\nu$ are poorly constrained and strongly affected by the hard priors applied and we therefore do not quote constraints.

Parameter	$\nu\Lambda$CDM			νwCDM		
	SPT-SZ+WL	SPTcl	*Planck*+SPTcl	SPTcl	*Planck*+SPTcl	*Planck*+BAO+SNIa+SPTcl
$\Omega_{\rm m}$	0.285 ± 0.047	0.276 ± 0.047	0.353 ± 0.027	0.299 ± 0.049	0.347 ± 0.039	0.305 ± 0.008
σ_8	0.763 ± 0.037	0.781 ± 0.037	0.761 ± 0.033	0.766 ± 0.036	0.761 ± 0.027	0.801 ± 0.026
$\sigma_8(\Omega_{\rm m}/0.3)^{0.2}$	0.753 ± 0.025	0.766 ± 0.025	0.786 ± 0.025	0.763 ± 0.024	0.782 ± 0.018	0.803 ± 0.024
$\sigma_8(\Omega_{\rm m}/0.3)^{0.5}$	0.739 ± 0.041	0.745 ± 0.042	0.824 ± 0.020	0.760 ± 0.043	0.816 ± 0.032	0.807 ± 0.023
h	$\cdots$	$\cdots$	0.645 ± 0.019	$\cdots$	0.657 ± 0.039	0.681 ± 0.009
$\sum m_\nu$ [eV]	$\cdots$	$\cdots$	0.39 ± 0.19	$\cdots$	0.50 ± 0.24	0.16 ± 0.10
w	-1	-1	-1	-1.55 ± 0.41	-1.12 ± 0.21	-1.03 ± 0.04
$A_{\rm SZ}$	$5.68^{+0.89}_{-1.03}$	$5.24^{+0.76}_{-0.92}$	$4.58^{+0.63}_{-0.92}$	$4.84^{+0.80}_{-0.97}$	$4.57^{+0.55}_{-0.62}$	$4.07^{+0.62}_{-0.76}$
$B_{\rm SZ}$	$1.519^{+0.087}_{-0.110}$	$1.534^{+0.099}_{-0.100}$	$1.667^{+0.069}_{-0.072}$	$1.601^{+0.098}_{-0.102}$	$1.653^{+0.079}_{-0.081}$	$1.685^{+0.074}_{-0.088}$
$C_{\rm SZ}$	$0.547^{+0.468}_{-0.375}$	$0.465^{+0.492}_{-0.321}$	$0.993^{+0.222}_{-0.218}$	$1.290^{+0.443}_{-0.250}$	$1.117^{+0.221}_{-0.191}$	$0.746^{+0.165}_{-0.169}$
$\sigma_{\ln\zeta}$	$0.152^{+0.066}_{-0.099}$	$0.161^{+0.084}_{-0.075}$	$0.162^{+0.083}_{-0.100}$	$0.169^{+0.082}_{-0.072}$	$0.148^{+0.073}_{-0.106}$	$0.133^{+0.055}_{-0.133}$
$A_{Y_{\rm X}}$	$\cdots$	$6.35^{+0.68}_{-0.69}$	$7.55^{+0.57}_{-0.56}$	$6.33^{+0.69}_{-0.78}$	$7.44^{+0.60}_{-0.68}$	$7.38^{+0.63}_{-0.65}$
$B_{Y_{\rm X}}$	$\cdots$	$0.514^{+0.028}_{-0.042}$	$0.480^{+0.028}_{-0.035}$	$0.499^{+0.032}_{-0.039}$	$0.488^{+0.032}_{-0.037}$	$0.480^{+0.033}_{-0.041}$
$C_{Y_{\rm X}}$	$\cdots$	$-0.310^{+0.140}_{-0.209}$	$-0.464^{+0.131}_{-0.133}$	$-0.669^{+0.120}_{-0.213}$	$-0.525^{+0.141}_{-0.143}$	$-0.371^{+0.123}_{-0.120}$
$\sigma_{\ln Y_{\rm X}}$	$\cdots$	$0.184^{+0.087}_{-0.089}$	$0.180^{+0.095}_{-0.102}$	$0.170^{+0.076}_{-0.094}$	$0.205^{+0.094}_{-0.087}$	$0.181^{+0.102}_{-0.162}$

Constraints on cosmological and scaling relation parameters are summarized in Table 3. We also provide constraints on the parameter combination $\sigma_8(\Omega_{\rm m}/0.3)^{0.2}$ and $\sigma_8(\Omega_{\rm m}/0.3)^{0.5}$; the exponent $\alpha = 0.2$ is chosen as it minimizes the fractional uncertainty on $\sigma_8(\Omega_{\rm m}/0.3)^\alpha$, and $\alpha = 0.5$ is common in other low-redshift cosmological probes.

4.1. $\nu\Lambda$CDM *Cosmology*

From the cluster abundance measurement of our SPTcl (SPT-SZ +WL+$Y_{\rm X}$) dataset we obtain our baseline results

$$\Omega_{\rm m} = 0.276 \pm 0.047 \tag{19}$$
$$\sigma_8 = 0.781 \pm 0.037 \tag{20}$$
$$\sigma_8(\Omega_{\rm m}/0.3)^{0.2} = 0.766 \pm 0.025. \tag{21}$$

The remaining cosmological parameters (including $\sum m_\nu$, see Fig. 9) are not or only weakly constrained by the cluster data. Constraints on scaling relation parameters can be found in Table 3. We note that applying priors on $\Omega_{\rm b}h^2$ and H_0 from BBN and direct measurements of H_0 and/or fixing the sum of neutrino masses to 0.06 eV, approximately the lower limit predicted from terrestrial oscillation experiments, does not affect our constraints on $\Omega_{\rm m}$ and σ_8 in any significant way (see Fig. 15 in the Appendix for the impact of fixing the sum of the neutrino masses).

4.1.1. *Goodness of Fit*

In Fig. 4, we compare the measured distribution of clusters as a function of their redshift and SPT detection significance with the model prediction evaluated for the recovered parameter constraints. This figure does not suggest any problematic feature in the data.

For a more quantitative discussion, we bin our confirmed clusters into a grid of 30×30 in redshift and detection significance, and confront this measurement with the expected number of objects in each two-dimensional bin. The expected (and measured) numbers in each bin are too small to apply Gaussian χ^2 statistics, and we estimate the goodness of fit using a prescription for the Poisson statistic (Kaastra 2017).[4] This approach is similar to our likelihood analysis, which applies Poisson statistics within infinitesimally small bins, instead of the larger bins we assume here. Adopting the maximum-posterior $\nu\Lambda$CDM parameters, we compute the expected number of clusters in each of the 30×30 bins and follow Kaastra (2017) to evaluate the test statistic C. We obtain an expected mean $C_{\rm e}$ and variance $C_{\rm v}$

$$C_{\rm e} = 439.8; \ C_{\rm v} = 26.8^2. \tag{22}$$

---

[4] We use the PYTHON implementation from https://github.com/abmantz/cstat.
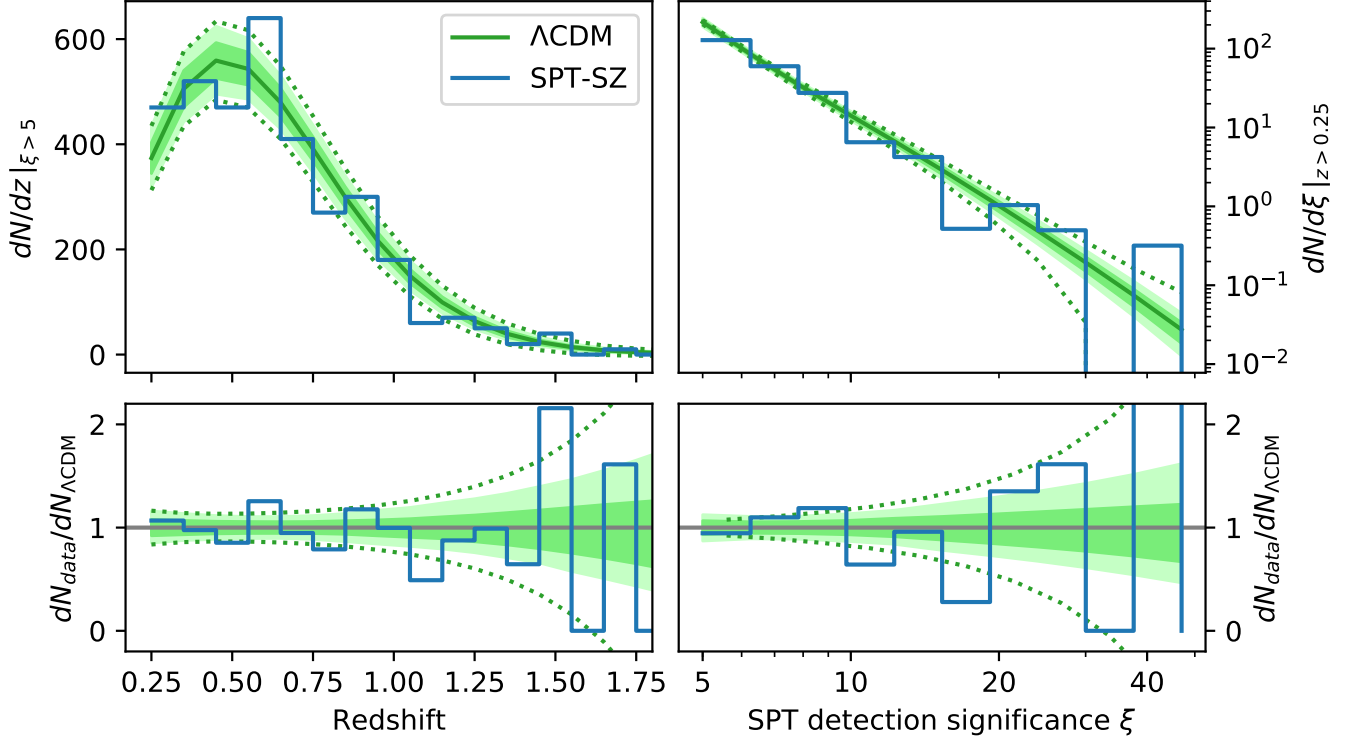
Figure 4. Distribution of clusters as a function of redshift (*left panels*) and detection significance ξ (*right panels*). The *top panels* show the SPT-SZ data and the recovered model predictions for $\nu\Lambda$CDM. The *bottom panels* show the residuals of the data with respect to the model prediction. The different lines and shadings correspond to the mean recovered model and the 1σ and 2σ allowed ranges. The dotted lines show the Poisson error on the mean model prediction. There are no clear outliers and we conclude that the model provides an adequate fit to the data.

For samples that contain at least a few hundred objects—like ours—the statistic C is well approximated by a Gaussian with mean C_e and variance C_v (Kaastra 2017). The data statistic for our sample is

$$C_d = 449.3 \tag{23}$$

in full agreement with the range expected for C_e, indicating that the model provides an adequate fit to the data.

4.1.2. *Comparison with Previous SPT results*

As discussed in the Introduction, this work uses the same SPT-SZ cluster sample (Bleem et al. 2015, now with updated photometric redshifts, see Section 2.1) that was analyzed in dH16, and the key update is the inclusion of WL data. In dH16, the amplitude of the observable–mass relation was set by a prior on the X-ray normalization A_{Y_X}, which in turn was informed by external WL datasets (CCCP and WtG, Applegate et al. 2014; von der Linden et al. 2014; Hoekstra et al. 2015). Gaussian priors were applied to the remaining SZ and X-ray scaling relation parameters, which we dropped for this analysis. In Fig. 5, we compare our constraints on Ω_m-σ_8 with the ones presented in dH16. We recover
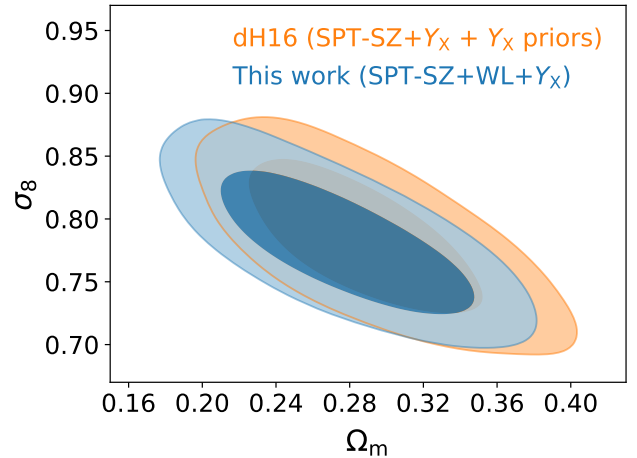
Figure 5. Constraints on Ω_m and σ_8 from this analysis an from a previous analysis that used the same cluster sample (dH16). The consistency (0.2σ) indicates that our internal mass calibration using WL data agrees with the external X-ray mass calibration priors adopted in dH16.

very similar results; in Ω_m-σ_8 space, the agreement is $p = 0.86$ (0.2σ). Since the key difference between dH16
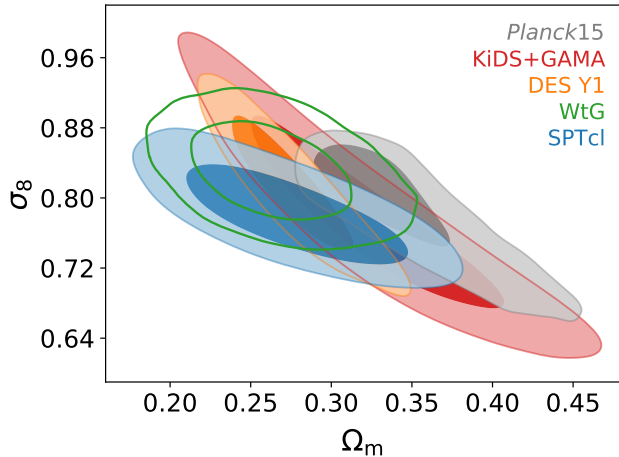
Figure 6. $\nu\Lambda$CDM constraints on Ω_m and σ_8. The SPTcl dataset comprises SPT-SZ+WL+Y_X, *Planck* is TT+lowTEB, KiDS+GAMA and DES Y1 are cosmic shear+galaxy clustering+galaxy-galaxy-lensing. The WtG (X-ray selected clusters) result also contains their f_{gas} measurement.

and this work is the inclusion of WL data, this agreement indirectly confirms that our internal WL mass calibration agrees with the external priors adopted previously. This is expected because the X-ray prior adopted in previous work agrees well with the measurement enabled by our own WL dataset (D17).

4.1.3. *Comparison with External Probes*

In Fig. 6, we show a comparison of our results with constraints from *Planck* (TT+lowTEB) and from combined analyses of cosmic shear, galaxy-galaxy lensing, and galaxy clustering from the Kilo Degree Survey and the Galaxies And Mass Assembly survey (KiDS+GAMA, van Uitert et al. 2018) and the Dark Energy Survey (DES) Year 1 results (Abbott et al. 2018). We also compare our results with another cluster study that used internal WL mass calibration, but a sample based on X-ray selection (Weighing the Giants, or WtG, Mantz et al. 2015). Overall, the constraining power of all probes is roughly similar in this plane. There is good agreement among all probes as the 68% contours all overlap. In particular, the cluster-based constraints yield very similar Ω_m, but WtG favor a somewhat higher σ_8. Interestingly, the degeneracy axis of WtG is slightly tilted with respect to SPTcl, which we attribute to the different redshift and mass ranges spanned by the two samples.

We pay particular attention to a comparison with *Planck*. Our constraint on $\sigma_8(\Omega_m/0.3)^{0.2} = 0.766 \pm 0.025$ is lower than the one from *Planck* ($\sigma_8(\Omega_m/0.3)^{0.2} = 0.814^{+0.041}_{-0.020}$); the agreement between the two measurements is $p = 0.28$ (1.1σ). In the two-dimensional Ω_m-σ_8 space, the agreement is $p = 0.13$ (1.5σ).
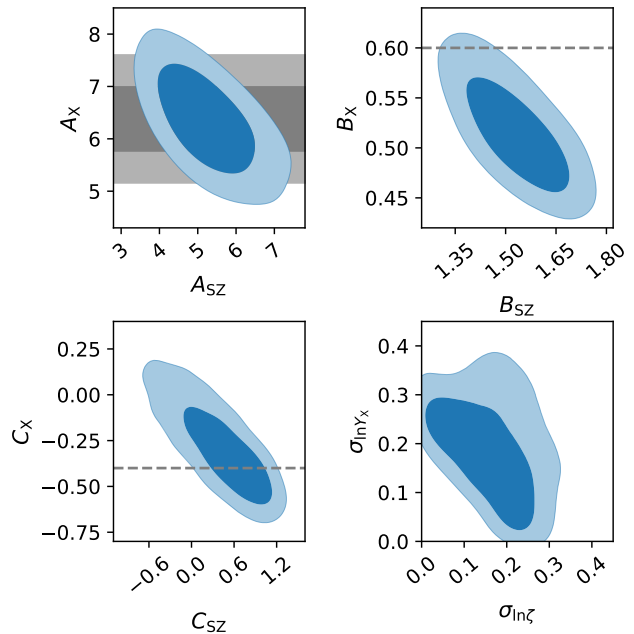
Figure 7. Our dataset is sensitive to the joint SZ-X-ray relation, which leads to correlations between the SZ and X-ray scaling relation amplitudes A (top left), mass-slopes B (top right), redshift evolutions C (bottom left), and intrinsic scatters σ (bottom right). We also show the external WL-informed prior on the X-ray amplitude A_{Y_X} applied in dH16, and the self-similar expectations for the X-ray slope B_{Y_X} and redshift evolution C_{Y_X}.

4.1.4. *Impact of X-ray Follow-up Data*

We compare our baseline results from SPTcl (SPT-SZ+WL+Y_X) with the ones obtained from the SPT-SZ+WL data combination, in which no X-ray follow-up data are included. In this case, we apply an informative Gaussian prior to the SZ scatter $\sigma_{\ln\zeta}$. As in all of this work, no informative priors are applied on the remaining three SZ scaling relation parameters and on the X-ray scaling relation parameters. A figure showing constraints on all relevant parameters can be found in Appendix B (Fig. 16, compare blue and red contours) and Table 3 summarizes parameter constraints. Both data combinations, with and without X-ray data, provide very similar constraints on cosmological and scaling relation parameters. Without informative priors on the X-ray amplitude, mass-slope, or redshift evolution the inclusion of X-ray data does not enable tighter constraints. The use of X-ray data does, however, enables constraints on the SZ and X-ray scatters $\sigma_{\ln\zeta}$ and $\sigma_{\ln Y_X}$, with flat priors applied to both.

Note that our data set is sensitive to the SZ-to-X-ray relation. As defined in Section 3.1, our model consists of two observable–mass relations that each relate one observable to mass. This implies that the amplitudes, mass-slopes, and redshift-evolutions of the two scaling

relations are degenerate, as shown in Fig. 7. The degeneracy between $\sigma_{\ln \zeta}$ and $\sigma_{\ln Y_X}$ is particularly interesting: while the marginalized posterior of either of both parameters has substantial mass near 0 scatter (see Fig. 16), the lower right panel of Fig. 7 shows that 0 *total scatter* is clearly ruled out.

Our dataset is not able to constrain any of the coefficients describing the correlated scatter among the observables. The visual impression of a constraint in Fig. 16 stems from the requirement that the matrix describing the multi-observable scatter must be a valid non-degenerate covariance matrix which prevents combinations of extreme correlation coefficients.

4.1.5. *Constraints on X-ray Scaling Relation Parameters*

Without any informative priors on the X-ray scaling relation parameters, we can use the SPTcl dataset to constrain the Y_X–mass relation. The recovered amplitude

$$A_{Y_X} = 6.35 \pm 0.69 \tag{24}$$

is very close to the WL-informed prior (Hoekstra et al. 2015; Applegate et al. 2014; von der Linden et al. 2014; Mantz et al. 2015) that was used in our previous cosmology analysis ($A_{Y_X} = 6.38 \pm 0.61$, dH16). We constrain the redshift evolution of the Y_X–mass relation to

$$C_{Y_X} = -0.31^{+0.14}_{-0.21}. \tag{25}$$

The self-similar expectation $C_{Y_X} = -0.4$ is well within 1σ. Our measurement of the Y_X scatter

$$\sigma_{\ln Y_X} = 0.18 \pm 0.09 \tag{26}$$

is higher than, but consistent at the 1σ level with the prior 0.12 ± 0.08 adopted in previous SPT analyses. It closely matches the measurement 0.182 ± 0.015 from Mantz et al. (2016), although with larger uncertainty.

The recovered Y_X mass-slope

$$B_{Y_X} = 0.514 \pm 0.037 \tag{27}$$

is lower than the self-similar evolution $B_{Y_X} = 0.6$ and the measurements $B_{Y_X} = 0.57 \pm 0.03$ from Vikhlinin et al. (2009a) and $B_{Y_X} = 1/(1.61 \pm 0.04) = 0.621 \pm 0.015$ from Mantz et al. (2016).[5] From our data, the consistency of B_{Y_X} with the self-similar value is $p = 0.021$, corresponding to 2.3σ. Our data constrain B_{Y_X} through its degeneracy with the SZ mass-slope B_{SZ} (Fig. 7), which in turn is constrained through the process of fitting the cluster abundance against the HMF. This subject was already discussed in dH16, where a prior on B_{Y_X} was adopted from the measurement by Vikhlinin et al. (2009a).

As a cross-check, and because other groups have used the X-ray gas mass as their low-scatter mass proxy, we repeat the analysis replacing the Y_X data with M_{gas} measurements. We apply no informative priors on the four parameters of the M_{gas} scaling relation of Eq. 5. We then analyze this SPT-SZ+WL+M_{gas} dataset. The constraints on the SZ scaling relation parameters and cosmology are very similar to the results from the fiducial SPT-SZ+WL+Y_X analysis, and again we observe an X-ray mass-slope that disagrees with the self-similar evolution. We measure

$$A_{M_g} = 0.116 \pm 0.011 \tag{28}$$
$$B_{M_g} = 1.22 \pm 0.07 \tag{29}$$
$$C_{M_g} = -0.05 \pm 0.17 \tag{30}$$
$$\sigma_{\ln M_g} = 0.11 \pm 0.04. \tag{31}$$

This corresponds to a 2.5σ preference for a slope that is steeper than the self-similar expectation $B_{M_g} = 1$ or the measurement $B_{M_g} = 1.004 \pm 0.014$ from Mantz et al. (2016). The measurement $B_{M_g} = 1.15 \pm 0.02$[6] from Vikhlinin et al. (2009a) is in between the two results, and is 1σ low compared to ours. Because these slopes differ, we compare the measurements of the gas fraction A_{M_g} at the pivot mass in our relation $5 \times 10^{14} M_\odot/h_{70}$, where we obtain Eq. 28. The mean gas fraction at this mass is 0.128 from Mantz et al. (2016) and 0.114 from Vikhlinin et al. (2009a). Both values are contained within the 1σ range of our measurement. Finally, as for Y_X, our measurement of the redshift evolution encompasses the self-similar evolution ($C_{M_g} = 0$) within 1σ.

For an extensive discussion of the mass and redshift trends in the M_{gas}–mass and Y_X–mass relations for SPT selected clusters and how they compare to previously published results, we refer the reader to two recent studies where SZ based mass information was adopted using the posterior distributions of the SZ ζ–mass relation parameters presented in dH16 (Chiu et al. 2018; Bulbul et al. 2018). Bulbul et al. (2018) used X-ray data from *XMM-Newton* while we use data from *Chandra*; their recovered constraints on the X-ray mass slopes and redshift evolutions are consistent with our findings at the 1σ level which confirms a consistent X-ray analysis. Here we note that most measurements of X-ray scaling relations have been performed using samples at low redshifts $z \lesssim 0.5$, and so it is of particular interest to examine the mass slopes for the low redshift half of our sample.

We therefore split our cluster sample (and all follow-up data) into two subsamples above and below redshift of $z = 0.6$, the median redshift of our sample. Constraints on the most relevant parameters are shown in Fig. 16 in the Appendix, and Fig. 8 shows the con-

---

[5] The scaling relation in Mantz et al. (2016) is defined as a power law in mass, whereas we use a power law in Y_X.

[6] Vikhlinin et al. (2009a) use the functional form $f_{gas} = f_{gas,0} + \alpha \ln M$. The mass dependence α is converted into a power-law exponent in Chiu et al. (2018).
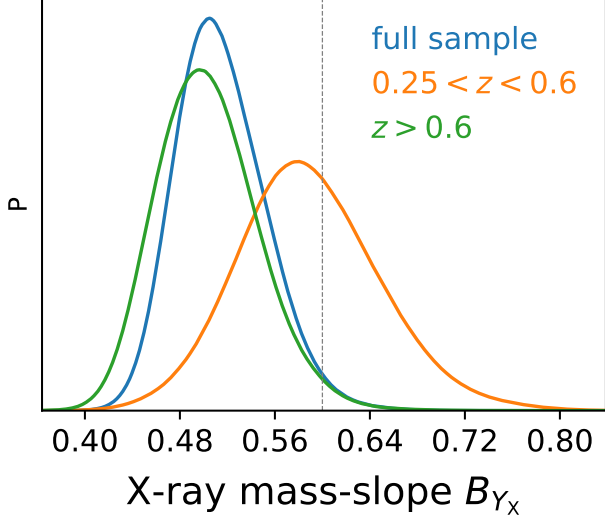
Figure 8. Constraint on the X-ray Y_X slope B_{Y_X} from the full sample, and from the low- and high-z halves. The self-similar expectation $B_{Y_X} = 0.6$ is 2.3σ off the result from the full sample, but within 1σ of the low-z result.

straints on B_{Y_X}. Interestingly, the low-redshift subsample prefers a higher value

$$B_{Y_X}(0.25 < z < 0.6) = 0.583^{+0.054}_{-0.069} \qquad (32)$$

that is closer to the self-similar evolution $B_{Y_X} = 0.6$. As expected, the value obtained from the high-z subsample

$$B_{Y_X}(z > 0.6) = 0.503^{+0.037}_{-0.047} \qquad (33)$$

is lower than the one obtained from the full sample. However, note that the low-redshift and high-redshift constraints on B_{Y_X} only differ with $p = 0.44$ (0.8σ).

We perform the same splits in redshift using the SPT-SZ+WL+$M_{\rm gas}$ dataset. Here as well, our measurement using the low-redshift subsample

$$B_{M_g}(0.25 < z < 0.6) = 1.12 \pm 0.09 \qquad (34)$$

is closer to the self-similar evolution, while the high-redshift half yields a steeper slope

$$B_{M_g}(z > 0.6) = 1.36 \pm 0.11. \qquad (35)$$

To capture a possible redshift dependence of the slope of the X-ray scaling relations, we analyzed models with an extended scaling relation model of the form

$$
\begin{aligned}
\ln \mathcal{O}_{\rm X\text{-}ray} = &\ln A + B \ln \left(\frac{M_{500c}\, h_{70}}{5 \times 10^{14} M_\odot} \right) \\
&+ C \ln \left(\frac{E(z)}{E(0.6)} \right) \\
&+ E \ln \left(\frac{E(z)}{E(0.6)} \right) \ln \left(\frac{M_{500c}\, h_{70}}{5 \times 10^{14} M_\odot} \right)
\end{aligned}
\qquad (36)
$$
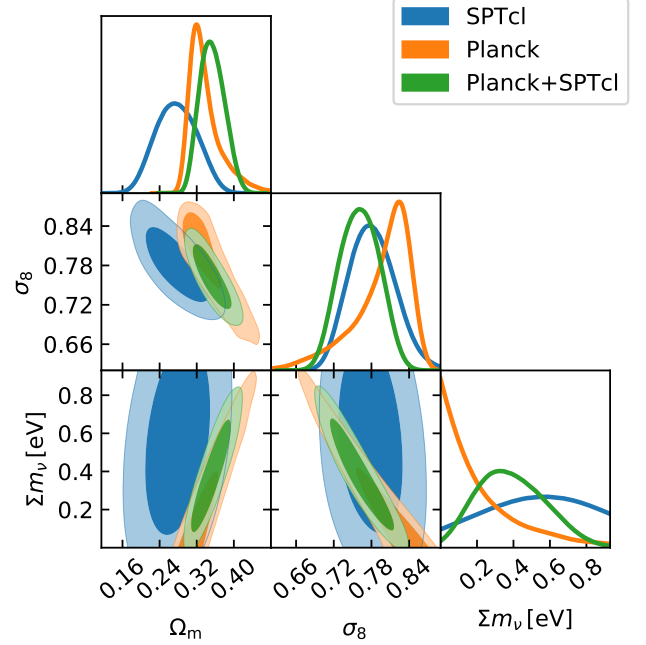
Figure 9. $\nu\Lambda$CDM constraints on $\Omega_{\rm m}$, σ_8, and $\sum m_\nu$. The SPTcl dataset comprises (SPT-SZ+WL+Y_X), *Planck* uses TT+lowTEB. Note that the cluster data constrain $\Omega_{\rm m}$ and σ_8 almost independently of $\sum m_\nu$.

that allows for additional freedom and the mass- and redshift-dependences. However, we do not observe any significant departure in E from 0, in agreement with Bulbul et al. (2018).

4.2. *Constraints on the Sum of Neutrino Masses*

Having quantified the consistency between our cluster dataset and *Planck* in Section 4.1.3, we proceed and combine the two probes. The SPTcl+*Planck* dataset yields

$$\Omega_{\rm m} = 0.353 \pm 0.027 \qquad (37)$$

$$\sigma_8 = 0.761 \pm 0.033 \qquad (38)$$

$$\sigma_8(\Omega_{\rm m}/0.3)^{0.2} = 0.786 \pm 0.025 \qquad (39)$$

$$\sum m_\nu = 0.39 \pm 0.19 \text{ eV} \qquad (40)$$

$$\sum m_\nu < 0.74 \text{ eV (95\% upper limit).} \qquad (41)$$

Compared to constraints from *Planck* alone, the combination with SPTcl shrinks the errors on $\Omega_{\rm m}$, σ_8, and $\sigma_8(\Omega_{\rm m}/0.3)^{0.2}$ by 3%, 12%, and 20%. By breaking parameter degeneracies (notably between σ_8 and $\sum m_\nu$, see Fig. 9), the addition of cluster data to the primary CMB measurements by *Planck* affects the inferred sum of neutrino masses. If interpreted as a Gaussian probability distribution (i.e., ignoring the hard cut $\sum m_\nu > 0$), our joint measurement corresponds to a 2.0σ preference for a non-zero sum of neutrino masses.
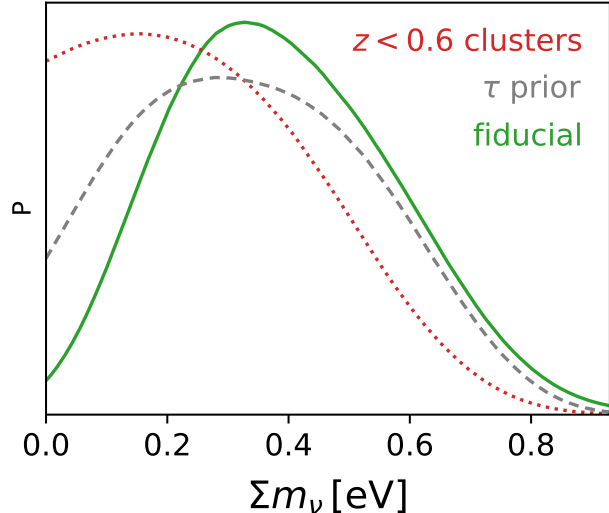
Figure 10. Constraints on $\sum m_\nu$ from the joint analysis of SPTcl and *Planck* data. Our fiducial analysis favors a non-zero sum of neutrino masses. However, when only using the low-redshift half $z < 0.6$ of our cluster sample or when replacing *Planck* TT+lowTEB with *Planck* TT + a prior $\tau \sim \mathcal{N}(0.054, 0.007^2)$ this preference diminishes.

The *Planck* collaboration recently presented an updated analysis of primary CMB anisotropies (Planck Collaboration et al. 2018). Most notably, the optical depth decreased to $\tau = 0.054 \pm 0.007$. As the updated *Planck* likelihood code is not available yet, we estimate the impact of the updated *Planck* analysis on our results and especially our constraint on $\sum m_\nu$ by analyzing the *Planck* 2015 TT data (without lowTEB) with a prior on $\tau \sim \mathcal{N}(0.054, 0.007^2)$. We analyze the joint SPTcl+*Planck* TT+τprior dataset and obtain

$$\sum m_\nu = 0.35 \pm 0.21 \text{ eV}. \qquad (42)$$

The recovered constraint is lower than our fiducial constraint using the (SPTcl+*Planck* TT+lowTEB) dataset and the 95% credible interval runs against the hard prior $\sum m_\nu = 0$. The preference for a non-zero sum of neutrino masses reduces to 1.7σ. We caution the reader that this result is only preliminary due to the way it depends on the prior on τ that we adopted. The full analysis will require analyzing our cluster sample jointly with the latest *Planck* analysis.

We explain the shift in $\sum m_\nu$ toward lower values as follows. In ΛCDM, the relationship between A_s and σ_8 is essentially fixed. However, in $\nu\Lambda$CDM, the additional degree o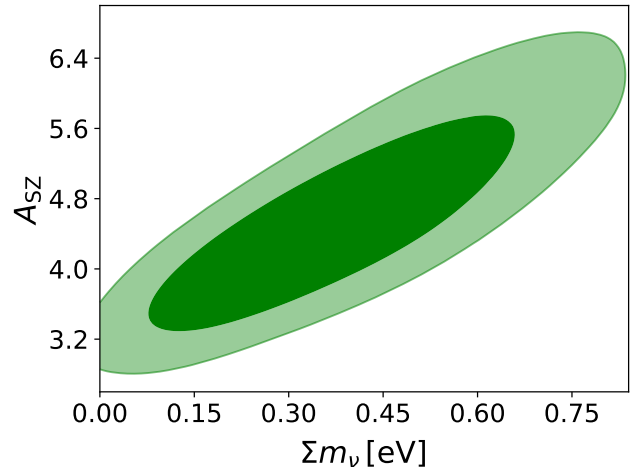f freedom $\sum m_\nu$ allows for different values of σ_8 at a fixed A_s. In any joint analysis of *Planck*+low-redshift growth-of-structure-probe as SPTcl, $\sum m_\nu$ is constrained to accommodate the *Planck* measurement of A_s with the low-redshift measurement of σ_8. As has been pointed out many times, the *Planck*15 measure-

Figure 11. Parameter correlation between the sum of neutrino masses $\sum m_\nu$ and the amplitude of the SZ observable–mass relation $A_{\rm SZ}$ for the SPTcl+*Planck* dataset. An improved cluster mass calibration will enable tighter constraints on neutrino properties.

ment of A_s implies a higher σ_8 in ΛCDM than obtained from local measurements, which leads to an apparent detection of $\sum m_\nu$ in $\nu\Lambda$CDM. Meanwhile, CMB temperature fluctuations are sensitive to the combination $A_s e^{-2\tau}$—i.e., A_s and τ are positively correlated in TT parameter constraints—so imposing a τ prior with a lower central value results in a lower inferred value of A_s. In ΛCDM, this shifts the *Planck*-inferred σ_8 to lower values. Finally, when analyzing *Planck* TT+τ+SPTcl in $\nu\Lambda$CDM, σ_8 is dominated by the local constraint from SPTcl, and the lower A_s implies that $\sum m_\nu$ need not be as high as in our fiducial analysis.

We further test the impact of using only the low-redshift half of our cluster sample. The SPTcl(0.25 < $z < 0.6$)+*Planck* dataset yields

$$\sum m_\nu = 0.29^{+0.09}_{-0.29} \text{ eV}. \qquad (43)$$

The probability distribution in $\sum m_\nu$ runs against the hard prior $\sum m_\nu > 0$ which shifts the mean recovered value away from the mode; the 68% credible interval starts at $\sum m_\nu = 0$. In conclusion, all preference for a non-zero sum of neutrino masses vanishes when only considering the low-redshift half of our cluster sample. Fig. 10 shows the constraints on $\sum m_\nu$ as obtained in our fiducial analysis, the analysis with the τ prior and the analysis where we only use the low-redshift cluster data.

The sum of neutrino masses is degenerate with the amplitude of the SZ scaling relation $A_{\rm SZ}$ with a correlation coefficient $\rho_{A_{\rm SZ}-\sum m_\nu} = 0.83$, see Fig. 11. Therefore, an improved (WL) mass calibration will improve the constraints on $\sum m_\nu$. Also note that the effect of massive neutrinos on the HMF depends (weakly) on mass and

redshift (Ichiki & Takada 2012). Therefore, an improved mass calibration covering the entire cluster sample will in principle allow for measurements of the sum of neutrino masses from clusters alone.

4.3. νwCDM *Cosmology*

We consider an extension to modeling dark energy as a cosmological constant by allowing for an equation of state parameter w that is different from $w = -1$. This modification impacts the expansion history of the Universe $E(z)$ and the growth of structure; both affect the cluster abundance. Therefore, as noted in, e.g., Haiman et al. (2001), measuring the abundance over a range of redshifts allows for a measurement of w. Using our SPTcl dataset we obtain

$$w = -1.55 \pm 0.41 \tag{44}$$
$$\Omega_{\mathrm{m}} = 0.299 \pm 0.049 \tag{45}$$
$$\sigma_8 = 0.766 \pm 0.036, \tag{46}$$

as shown by the blue contours in Fig. 12. Constraints on scaling relation parameters can be found in Table 3. The consistency of our recovered constraint on w with a cosmological constant $w = -1$ has a p-value 0.076 (1.8σ). Note that the SPTcl contours in the $\Omega_{\mathrm{m}} - \sigma_8 - w$ space close.

Our constraint on w is in general agreement with the result obtained from the SPT-SZ+Y_{X}+X-ray priors data combination $w = -1.28 \pm 0.31$ as presented in dH16. In that earlier analysis, informative (Gaussian) priors were applied on the scaling relation parameters A_{SZ}, B_{SZ}, C_{SZ}, $\sigma_{\ln \zeta}$, $A_{Y_{\mathrm{X}}}$, $B_{Y_{\mathrm{X}}}$, $C_{Y_{\mathrm{X}}}$, $\sigma_{\ln Y_{\mathrm{X}}}$, whereas we marginalize over flat priors and use our internal WL mass calibration. However, even when analyzing the same data combination used in dH16 (without WL data) and applying the same priors, our analysis pipeline gives a more negative value of $w = -1.53^{+0.36}_{-0.25}$. As described in Section 3.4, we have extensively tested our analysis pipeline, including tests against mock catalogs with input values of $w \neq -1$. The analysis pipeline used in dH16 was not subjected to that test. Using our internal WL mass calibration shifts the constraints on w toward even more negative values. Finally, the cluster photometric redshifts were updated since the dH16 analysis (see Section 2.1), with the net impact being a shift in w toward less negative values of similar magnitude to the shift due to our WL mass calibration. In the end, some of these shifts in w partially cancel out, and the final constraint we present here is 0.7σ low in comparison to that in dH16.

We proceed and analyze the joint SPTcl+*Planck* dataset. The cluster data break some of the *Planck* parameter degeneracies shown in Fig. 12 and we mea-

sure

$$w = -1.12 \pm 0.21 \tag{47}$$
$$\Omega_{\mathrm{m}} = 0.347 \pm 0.039 \tag{48}$$
$$\sigma_8 = 0.761 \pm 0.027 \tag{49}$$
$$\sum m_\nu = 0.50 \pm 0.24 \text{ eV}. \tag{50}$$

Interestingly, while the individual constraints on w are both centered on $w \approx -1.5$, the joint analysis provides a constraint that is offset closer toward $w = -1$. This is due to the different orientations of the $w - \sigma_8$ degeneracies in Fig. 12 which overlap close to $w = -1$. Compared to the results obtained in $\nu\Lambda$CDM, the constraints on σ_8 and $\sigma_8(\Omega_{\mathrm{m}}/0.3)^{0.2}$ do not degrade. However, the constraining power on the remaining cosmological parameters weakens (see Table 3).

Fig. 12 further shows the constraints obtained from BAO and SNIa. Neither of the two are affected by σ_8 and $\sum m_\nu$.[7] However, they both exhibit narrow parameter degeneracies that cut through the region of parameter space that is allowed by *Planck*. Therefore, the joint analyses of *Planck*+BAO and *Planck*+SNIa allow for constraints on νwCDM that are tighter than the ones from *Planck*+SPTcl (see Fig. 13).

Finally, we analyze the joint *Planck*+BAO+SNIa+SPTcl dataset (see constraints in Table 3). In comparison to *Planck*+BAO+SNIa, the addition of the SPTcl dataset leads to a shift $\Delta\sigma_8 = -0.031$. The constraints on Ω_{m}, h, and w are negligibly affected. However, note that the 95% upper limit on $\sum m_\nu$ from *Planck*+BAO+SNIa increases by 63% when adding SPTcl. A similar effect was seen in the DES 3x2 pt analysis (Abbott et al. 2018), where the upper limit on $\sum m_\nu$ from *Planck*+BAO+SNIa increased by a similar amount when adding the DES data. Both effects are due to the lower clustering amplitude measured by SPTcl and DES relative to the prediction by *Planck*+BAO+SNIa.

4.3.1. νwCDM: *Robustness of our Results to Data Cuts*

In the Appendix (Fig. 17), we show the parameter constraints that we recover when cutting our cluster sample in half at redshift 0.6, or when choosing a higher SZ selection threshold $\xi > 6.5$. There are no significant departures from our fiducial results for any data subset. However, both the low-redshift half of the data and the subsample above $\xi > 6.5$ yield constraints on w that are

---

[7] We note an unexpected shape of the BAO posterior on h, with a peak at $h \approx 0.68$ and a rising tail toward the edge of the prior $h < 0.9$. This is caused by the subsamples of BAO providing different results: The 6dF+SDSS posterior peaks at $h \approx 0.68$ and exhibits an approximately flat, non-zero tail in the range $0.8 < h < 0.9$. The posterior from BOSS increases monotonically throughout the entire allowed range in h and peaks at $h = 0.9$. Therefore, the joint BAO dataset peaks at the 6dF+SDSS location but then rises again toward $h = 0.9$ due to the BOSS constraint.
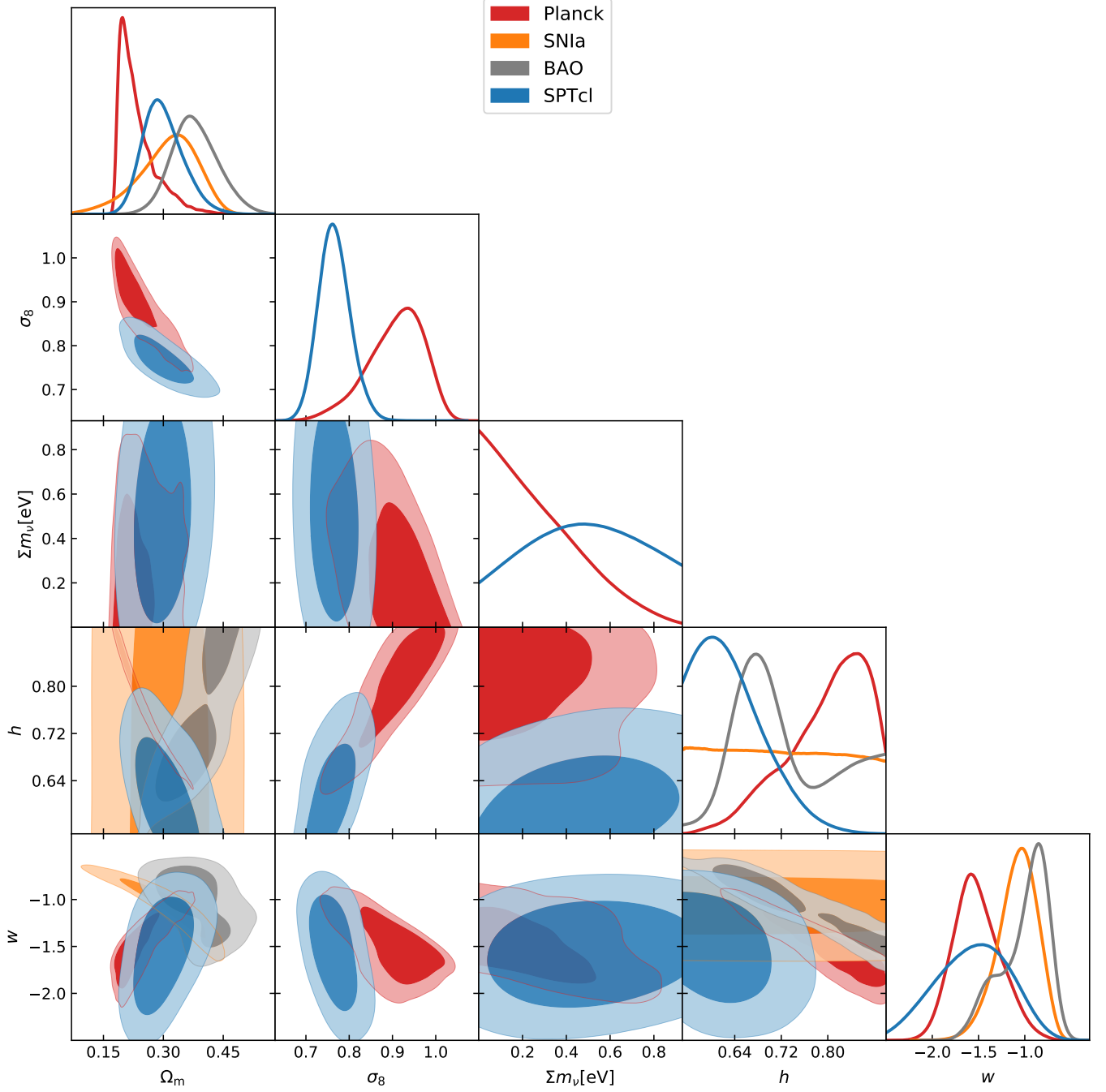
Figure 12. Constraints on νwCDM from SPT clusters, *Planck*, BAO, and SNIa. The 95% credibility contours all overlap. The biggest differences appear between SPTcl and *Planck* in the σ_8 and h parameters.

closer to the cosmological constant $w = -1$:

$$w(0.25 < z < 0.6) = -1.01^{+0.41}_{-0.25} \qquad (51)$$

$$w(\xi > 6.5) = -1.21^{+0.42}_{-0.29}. \qquad (52)$$

Conversely, the high-redshift half of the data gives

$$w(z > 0.6) = -1.58 \pm 0.46. \qquad (53)$$

We note that the constraints on w from the full sample is quite similar to this constraint from the high-redshift half of the data.

Fig. 17 further shows a strong degeneracy between w and the redshift evolution parameters of the scaling relations C_{SZ} and $C_{Y_{\mathrm{X}}}$. To tighten the dark energy constraints in future analyses it will therefore be important to improve the mass calibration over the entire redshift range of the cluster sample.

Bocquet et al.
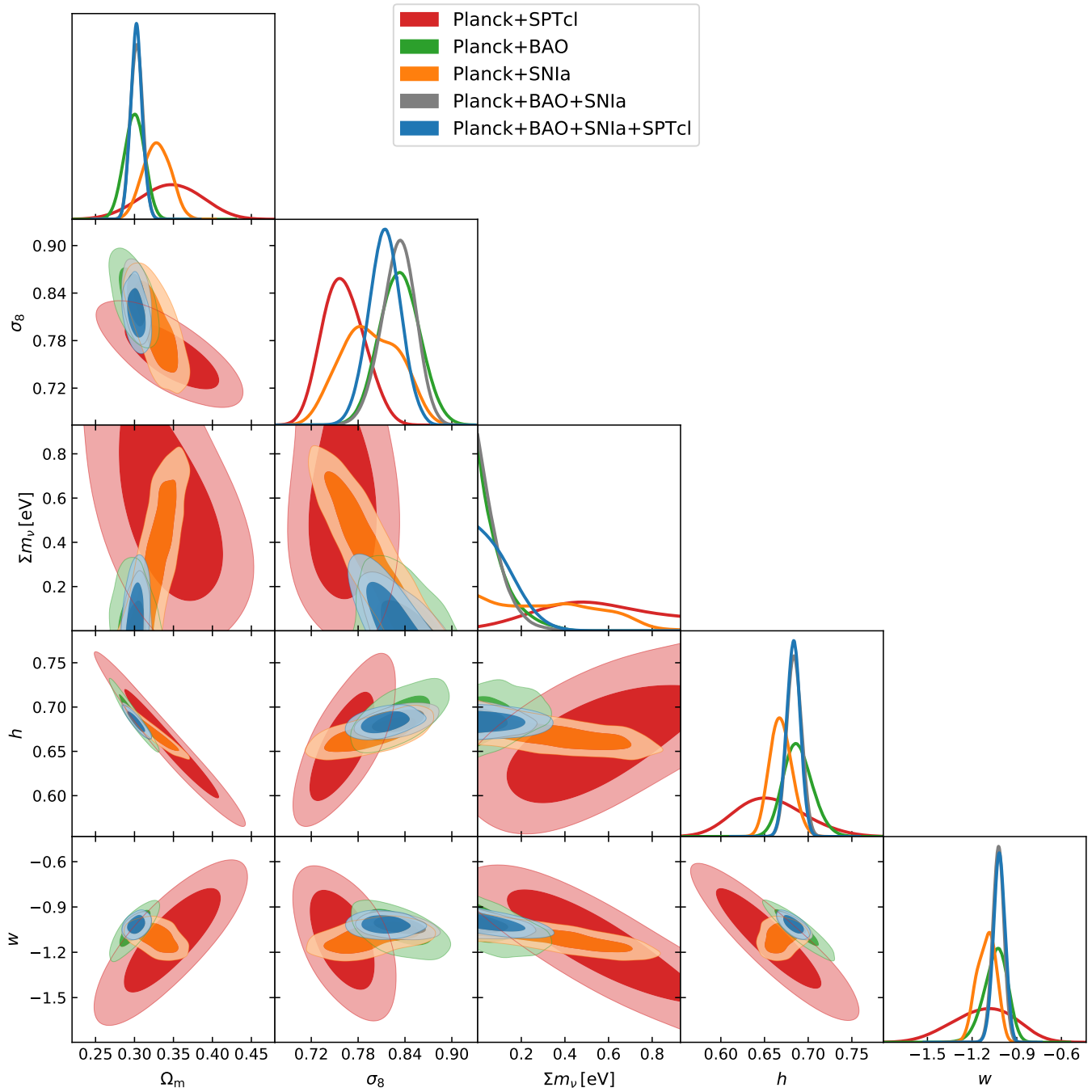
Figure 13. Constraints on νwCDM from joint analyses of *Planck* with SPTcl, BAO, or SNIa. We also show *Planck*+BAO+SNIa and the full joint analysis *Planck*+BAO+SNIa+SPTcl. When combining with *Planck*, our cluster dataset does not contribute as much additional information as do the other two external probes BAO and SNIa.

4.4. Growth of Structure: Measuring $\sigma_8(z)$

We consider another extension to ΛCDM where we do not alter the background expansion, but change the growth of structure. Clusters have been used to constrain modified structure growth by, for example, fitting for the growth index γ, which is defined by the relation $d\ln\delta/d\ln a \equiv \Omega_{\rm m}^\gamma(a)$ (e.g., Peebles 1980). A value of $\gamma \approx 0.55$ corresponds approximately to the growth rate in ΛCDM, and clusters allow for constraints on γ at the $\sim 40\%$ level (e.g., Rapetti et al. 2013; Bocquet et al. 2015; Mantz et al. 2015).

Instead of modeling linear deviations from GR via the growth index, we pursue a different route and constrain the growth of structure by directly measuring the linear amplitude of the density fluctuations, σ_8, as a function of redshift. We can then compare the measured $\sigma_8(z)$ with predictions from $\nu\Lambda$CDM, νwCDM, and more exotic models. This approach is non-parametric in that it does not assume a specific description for modified growth of structure, but rather assumes a $\nu\Lambda$CDM model (with its parameters allowed to vary) within each redshift bin.

We start from the $\nu\Lambda$CDM model and modify the amplitude of the linear matter power spectrum $P(k,z)$ within different redshift bins. We introduce an additional model parameter $\sigma_8(z_i)$ in each bin and normalize $P(k,z)$ within each redshift bin i to match $\sigma_8(z_i)$. The HMF is then computed from the modified $P(k,z)$ in the usual way. We define four redshift bins such that all bins contain approximately equal numbers of SPT clusters. We choose bin limits ($z = 0.25, 0.45, 0.6, 0.75, 1.7$). We include *Planck* primary CMB data in the fit. By construction, in our model the *Planck* data only constrain the background cosmology (expansion history $E(z)$), but do not contribute to constraining $\sigma_8(z)$. For simplicity, we do not use any X-ray data here and thus use the joint SPT-SZ+WL+*Planck* dataset; we apply the simulation prior on the SZ scatter.

We explore two scenarios: i) We assume our fiducial SZ scaling relation model across the entire redshift range. This means that the mass calibration will be correlated across the four redshift bins. ii) We additionally introduce independent normalizations of the SZ scaling relation $A_{\rm SZ,i}$ in each redshift bin i. This way, the amplitude of the SZ scaling relation is independently determined in each redshift bin (up to the shared WL systematics that are, however, sub-dominant here given the low number of clusters with WL constraints). We call the first scenario "coupled", and the second "decoupled", in reference to the treatment of the normalization of the SZ observable–mass relation.

Constraints on $A_{\rm SZ}$ and $\sigma_8(z)$ for the coupled and decoupled analyses are shown in Table 4. In the coupled analysis, the four measurements of $\sigma_8(z)$ are quite correlated with correlation coefficients $\rho(\sigma_8(z)) = 0.55-0.60$ because they are limited by the uncertainty in the observable–mass scaling relation that is shared across

the entire redshift range. In the decoupled analysis, however, the $\sigma_8(z)$ parameters are much less correlated ($\rho(\sigma_8(z)) = 0.06-0.12$) as mass calibration in each bin is done almost independently, and each $\sigma_8(z_i)$ is mostly degenerate with the corresponding normalization parameter $A_{\rm SZ}(z_i)$. As expected, the decoupled analysis leads to weaker constraints.

In Fig. 14, we show measurements of σ_8 as a function of redshift. The red bands shows the *prediction* for $\sigma_8(z)$ assuming $\nu\Lambda$CDM and *Planck* cosmological parameters. Blue and orange data points show *measurements* of $\sigma_8(z)$ using our clusters (with *Planck* priors on the background cosmology). The cluster measurements are all slightly lower than the predictions using *Planck* data, which simply reflects the difference in σ_8 discussed above for the $\nu\Lambda$CDM model (see Fig. 9). We emphasize that this offset is roughly constant throughout the entire range in redshift. In particular, the two bins above $z > 0.6$ that are leading to some shifts in cosmology and scaling relations as described in earlier sections do not seem to provide constraints that are qualitatively different from those obtained from the low-redshift bins.

Our measurements of $\sigma_8(z)$ are limited by the determination of $A_{\rm SZ}$, especially in the "decoupled" analysis. The three low-redshift bins will benefit from including cluster WL data from the Dark Energy Survey (Paulus et al., in prep.). The highest-redshift bin can only be improved with deep, high-resolution WL data, e.g., from the *Hubble Space Telescope*, or with lensing information from the CMB (e.g., Baxter et al. 2018). On the other hand, our cluster sample together with this technique allow us to place competitive constraints on the growth of structure over a wide range in redshifts.

4.5. Implications for SZ-Based Cluster Halo Masses

For the $\nu\Lambda$CDM and νwCDM analyses discussed above, Table 3 also presents constraints on the SZ scaling relation parameters. These, together with Eqs. 1 and 6 allow one to compute mass estimates $P(M_{500c}|\xi, z, \boldsymbol{p})$ for each cluster in our sample. Moreover, the scaling relation parameter constraints provide another point of comparison with past analyses.

The results in Table 3 exhibit a range of parameters across the six different analyses, but in no case are the parameter differences statistically significant. This indicates that the best estimates of the cluster masses are consistent among the different combinations of data and within the different cosmological models. As an example, the addition of the *Planck* dataset as an external prior leads to preferred values of the amplitude parameter $A_{\rm SZ}$ that are lower, corresponding to $\sim 8\%$ and $\sim 4\%$ higher masses at the pivot in $\nu\Lambda$CDM and νwCDM, respectively. These mass shifts are smaller than those presented by Bocquet et al. (2015), where the impact of external priors was first discussed. Interestingly, the redshift slope $C_{\rm SZ}$ prefers higher values in the νwCDM model, which corresponds to high-redshift masses that
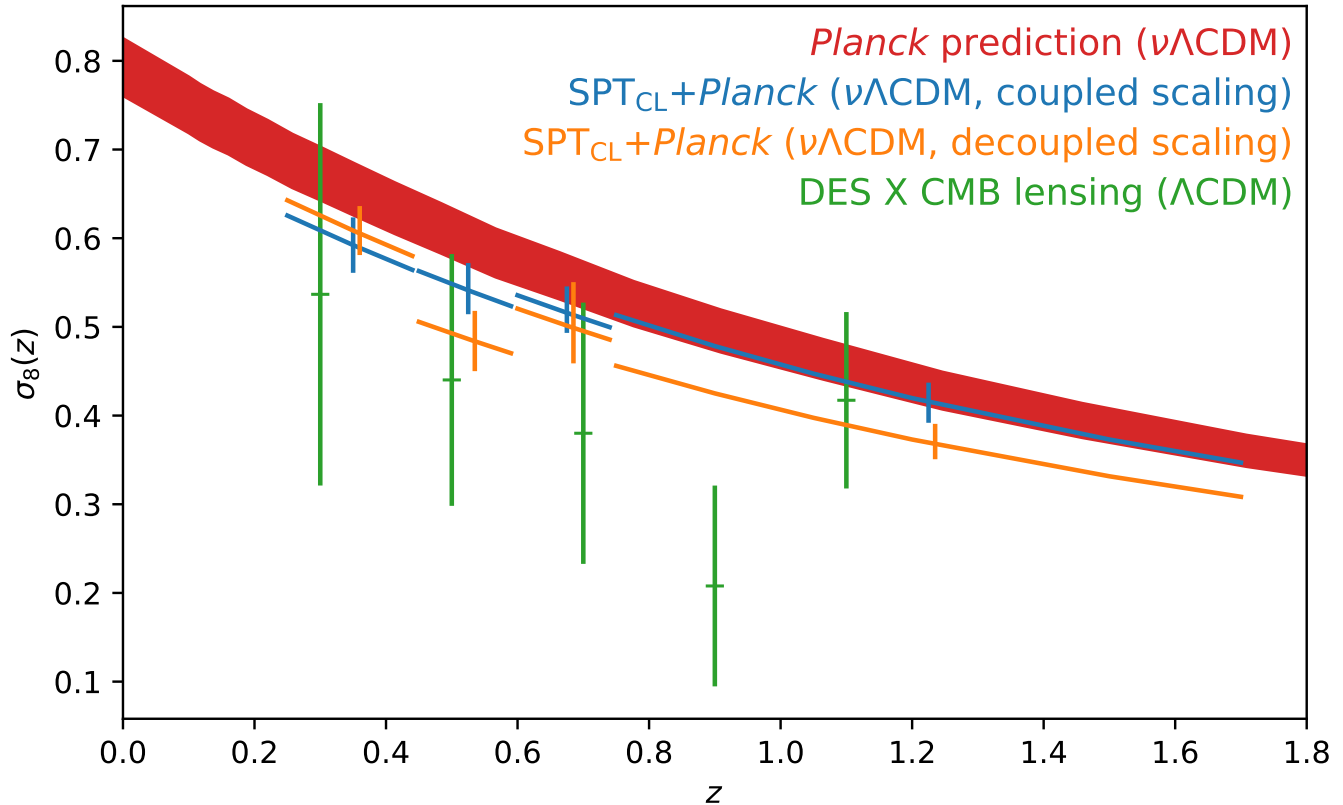
Figure 14. The evolution of σ_8 as a function of redshift. The *red band* shows the 1σ interval of the prediction obtained from *Planck* in the $\nu\Lambda$CDM cosmology. The *blue data points* are obtained in a joint SPTcl+*Planck* analysis, where $\sigma_8(z)$ is constrained only by the cluster sample. *Orange data points* are obtained from a similar analysis that allows for more freedom in the SZ scaling relation (see Section 4.4). The nearly horizontal error bars on the blue and orange data points indicate the extent of the redshift bins and are shaped to follow the evolution of σ_8 in the $\nu\Lambda$CDM model. For comparison, *green data points* show constraints from the cross-correlation of the galaxy density in the Dark Energy Survey Science Verification data with CMB lensing from SPT (Giannantonio et al. 2016).

are smaller relative to clusters with the same ξ at low redshift. In the νwCDM model these same values of $C_{\rm SZ} \sim 1$ are preferred with or without *Planck* priors, but shift back to a lower value when BAO+SNIa constraints are added. In comparison, in the results for ΛCDM presented in Table 3 of dH16, the amplitude parameter for the SPTcl+*Planck*+BAO analysis was $A_{\rm SZ} = 3.53 \pm 0.27$, which is significantly lower than the values presented here. Note, however, that massive neutrinos were not marginalized over in the baseline analysis in dH16.

Given the consistency in the implied masses across all six analyses presented here, we adopt the $\nu\Lambda$CDM results for the baseline SPTcl dataset in calculating mean masses and mass uncertainties (Table 3 column 3). The mass uncertainties include the ξ measurement and intrinsic scatter uncertainties (together these correspond to $\sim 20\%$ uncertainty for a cluster near our selection threshold) as well as marginalization over the posterior parameter distributions for $A_{\rm SZ}$, $B_{\rm SZ}$, $C_{\rm SZ}$ and $\sigma_{\ln\zeta}$ and

over the cosmological parameters (this corresponds to an additional $\sim 15\%$ uncertainty due to the remaining uncertainties in the mass calibration of the SPT-SZ sample). These masses are calculated by sampling the distribution

$$P(M|\xi, z, \boldsymbol{p}) = \iint dM d\zeta P(\xi|\zeta) P(\zeta|M, z, \boldsymbol{p}) P(M|z, \boldsymbol{p})$$
(54)

at each step in the likelihood analysis.

Table 5 contains a list of all cluster candidates in our sample with the associated sky location, SPT detection significance ξ, redshift and halo mass $M_{\rm 500c}$. In addition, we present the mass $M_{\rm 200c}$ for each system, assuming the concentration–mass relation from Duffy et al. (2008).

5. SUMMARY AND OUTLOOK

We present an analysis of the SPT-SZ cluster sample, supplemented with optical WL data and X-ray $Y_{\rm X}$ measurements. We set up a self-consistent analysis frame-

Table 4. Constraints on σ_8 and the SZ scaling relation normalization $A_{\rm SZ}$ as a function of redshift, measured in four redshift bins. In the *coupled analysis* we assume a single $A_{\rm SZ}$ parameter. In the *decoupled analysis* we fit for $A_{\rm SZ}$ separately in each redshift bin; this decorrelates the measurements of $\sigma_8(z)$ as evidenced by $\rho(\sigma_8(z))$.

Parameter	Coupled analysis	Decoupled analysis	*Planck* (TT+lowTEB)
$A_{\rm SZ}$	$5.40^{+0.80}_{-1.15}$	$\cdots$	$\cdots$
$A_{\rm SZ}(0.25 < z < 0.45)$	$\cdots$	$4.90^{+0.88}_{-1.09}$	$\cdots$
$A_{\rm SZ}(0.45 < z < 0.6)$	$\cdots$	$10.29^{+2.56}_{-4.23}$	$\cdots$
$A_{\rm SZ}(0.6 < z < 0.75)$	$\cdots$	$7.29^{+1.66}_{-4.47}$	$\cdots$
$A_{\rm SZ}(0.75 < z < 1.7)$	$\cdots$	$10.63^{+2.19}_{-3.08}$	$\cdots$
$\sigma_8(z = 0.35)$	0.592 ± 0.031	0.609 ± 0.028	0.656 ± 0.029
$\sigma_8(z = 0.525)$	0.543 ± 0.029	0.484 ± 0.034	0.597 ± 0.028
$\sigma_8(z = 0.675)$	0.519 ± 0.026	0.505 ± 0.046	0.555 ± 0.026
$\sigma_8(z = 1.225)$	0.415 ± 0.023	0.371 ± 0.020	0.432 ± 0.021
$\rho(\sigma_8(z))$	$0.55 - 0.60$	$0.06 - 0.12$	$\cdots$

work in which cosmology, scaling relations, a possible correlated scatter among cluster mass proxies, and other nuisance parameters are fit simultaneously. Within this framework, the WL data is used to constrain the normalization of the observable–mass relations (at various redshifts and cluster masses). We use numerical simulations to calibrate the relation between the unobserved, true halo mass, and the observed radial WL shear profiles. Wide, non-informative priors are assumed on the parameters of the SZ and X-ray scaling relations. At present, our mass calibration is limited by the number of clusters with WL data; the systematic uncertainties in the WL analysis are sub-dominant with 5.6% in mass for our ground-based data and 9.2% for the HST sample (D17; S18).

Our main findings are:

- Assuming simulation-based priors on the relation between true mass and WL mass $M_{\rm WL}$, we are able to simultaneously fit for cosmology (constraining $\Omega_{\rm m}$, σ_8, w) while constraining the amplitudes, mass-slopes, redshift-evolutions, and intrinsic scatter of the SZ and X-ray observable–mass relations. We marginalize over flat priors on $\Omega_\nu h^2$, $\Omega_{\rm b} h^2$, n_s, h which are not constrained from cluster data alone.

- Assuming the $\nu\Lambda{\rm CDM}$ model, our cluster-based constraint on $\sigma_8(\Omega_{\rm m}/0.3)^{0.2} = 0.766 \pm 0.025$ is lower than the one obtained from primary CMB fluctuations by *Planck*. The agreement between the two measurements is $p = 0.28$, or 1.1σ.

- We constrain the redshift evolution of the X-ray $Y_{\rm X}$–mass relation to $C_{Y_{\rm X}} = -0.31^{+0.14}_{-0.21}$ and the

redshift evolution of the $M_{\rm gas}$–mass relation to $C_{M_{\rm g}} = -0.05 \pm 0.17$. The self-similar evolution -0.4 for $Y_{\rm X}$–mass and 0 for $M_{\rm gas}$–mass is encompassed in the 1σ interval in both cases.

- We find the mass-dependence of the X-ray $Y_{\rm X}$–mass relation $B_{Y_{\rm X}} = 0.514 \pm 0.037$ to be steeper than the self-similar expectation $B_{Y_{\rm X}} = 0.6$ with a p-value of $p = 0.021$ (2.3σ). Interestingly, this difference is resolved when we only consider the low-redshift half of our sample at $z < 0.6$, where we measure $B_{Y_{\rm X}} = 0.583^{+0.054}_{-0.069}$. Conversely, the high-redshift half of our sample favors a steeper slope ($B_{Y_{\rm X}} = 0.503^{+0.037}_{-0.047}$), see also Fig. 8. The slope of the $M_{\rm gas}$–mass relation $B_{M_{\rm g}} = 1.22 \pm 0.07$ is also steeper than the self-similar evolution $B_{M_{\rm g}} = 1$. Here as well, the measurement of $B_{M_{\rm g}}$ at low redshift below $z = 0.6$ is closer to the self-similar value ($B_{M_{\rm g}} = 1.12 \pm 0.09$) than the high-redshift measurement ($B_{M_{\rm g}} = 1.36 \pm 0.11$).

- The joint dataset combining our clusters and primary CMB measurements from *Planck* allows for a constraint on the sum of neutrinos masses $\sum m_\nu = 0.39 \pm 0.19$ eV ($\sum m_\nu < 0.74$ eV (95% C.L.)). This preference for a non-zero sum of neutrino masses diminishes when combining *Planck* with only the low-redshift ($z < 0.6$) half of our cluster sample or when adopting a lower value of τ as suggested by Planck Collaboration et al. (2018). Due to parameter degeneracies, an improved cluster mass calibration will directly translate into tighter constraints on neutrino masses.

- Our constraint on $w = -1.55 \pm 0.41$ is somewhat lower than a cosmological constant, with $p = 0.076$ (1.8σ). The SPTcl contours in the $\Omega_{\rm m} - \sigma_8 - w$ space are closed, see Fig. 12. This reflects the fact that our cluster sample is able to constrain the three parameters simultaneously. When only considering the high-redshift $z > 0.6$ subsample, we obtain $w = -1.58 \pm 0.46$, whereas we obtain a less negative constraint $w = -1.01^{+0.41}_{-0.25}$ from the low-redshift subsample at $0.25 < z < 0.6$.

- We employ a new approach to measuring the linear growth of structure using clusters. This allows us to track the evolution of structure growth since redshift $z \sim 1.7$. Fig. 14 shows that structure formation evolved in agreement with the $\nu\Lambda$CDM prediction, although with a somewhat lower amplitude than predicted assuming cosmological parameters from *Planck*.

The validity of our cluster-based constraints relies on an accurate prediction of the HMF throughout the entire parameter space considered. However, the HMF fit by Tinker et al. (2008), is calibrated using N-body simulations for cosmologies that are close to WMAP results, and the extrapolation to other cosmologies is performed assuming the universality of the HMF. Ongoing analyses of cosmological simulations will provide accurate predictions of the HMF for a much broader range of cosmologies (Heitmann et al. 2016; McClintock et al. 2018b, Bocquet et al., in prep.).

We discuss the departure from self-similarity of the X-ray $Y_{\rm X}$ and $M_{\rm gas}$ mass-slopes. There is a suggestion of an evolution of the $Y_{\rm X}$ mass slope with redshift, where it exhibits more self-similar results in the low-redshift half cluster sample. Similar results have been presented in the previous SPT cosmology analysis (dH16) as well as in X-ray observable–mass scaling relation studies that rely on SZ based cluster masses (Chiu et al. 2016, 2018; Bulbul et al. 2018), where masses are calculated using the mass calibration results from previous SPT cluster cosmology analyses (Bocquet et al. 2015, dH16). This could be a sign that X-ray scaling relations depart from self-similarity in this mass and redshift range (e.g., the ICM mass fraction varies with cluster mass as shown first in Mohr et al. 1999), or there could be additional effects not captured by our model that affect e.g., the SZ scaling relation or selection. Larger SZ-selected cluster samples and more extensive follow-up data are necessary to discern these effects.

In upcoming analyses, we will expand our SPT-SZ cluster sample with data from SPTpol. This will both increase our sample of high-mass clusters, and push down to lower cluster masses in the deeper fields of the survey. At the same time, it is important to pursue our WL campaign at all redshifts covered by our sample. Indeed, the strategic overlap with the DES (Dark Energy Survey Collaboration et al. 2016) will allow for a robust mass-calibration at moderate redshifts (Melchior et al. 2017; Stern et al. 2018; McClintock et al. 2018a). To exploit the full potential of the SPT cluster sample, it will be crucial to also tighten the WL mass constraints at higher redshifts. At intermediate redshifts this can be achieved with deep ground-based $K_{\rm s}$ imaging (Schrabback et al. 2018b), but at high redshifts $z > 1$ these measurements critically require additional HST observations or ultimately the datasets from Euclid (Laureijs et al. 2011) and LSST (Ivezic et al. 2008). With the current and next generation of high-resolution CMB experiments such as SPT-3G (Benson et al. 2014; Bender et al. 2018), Advanced ACTpol (De Bernardis et al. 2016), or CMB-S4 (Abazajian et al. 2016), CMB lensing will provide another means of accurate mass calibration out to redshifts well beyond $z \sim 1$.

REFERENCES

Abazajian, K. N., Adshead, P., Ahmed, Z., et al. 2016, ArXiv e-prints, arXiv:1610.02743

Abbott, T. M. C., Abdalla, F. B., Alarcon, A., et al. 2018, PhRvD, 98, 043526

Alam, S., Ata, M., Bailey, S., et al. 2017, MNRAS, 470, 2617

Allen, S. W., Evrard, A. E., & Mantz, A. B. 2011, ARA&A, 49, 409

Applegate, D. E., von der Linden, A., Kelly, P. L., et al. 2014, MNRAS, 439, 48

Astropy Collaboration, Price-Whelan, A. M., Sipőcz, B. M., et al. 2018, AJ, 156, 123

Baxter, E. J., Raghunathan, S., Crawford, T. M., et al. 2018, MNRAS, 476, 2674

Bayliss, M. B., Ruel, J., Stubbs, C. W., et al. 2016, ApJS, 227, 3

Bender, A. N., Ade, P. A. R., Ahmed, Z., et al. 2018, in Society of Photo-Optical Instrumentation Engineers (SPIE) Conference Series, Vol. 10708, Society of Photo-Optical Instrumentation Engineers (SPIE) Conference Series, 1070803

Benson, B. A., de Haan, T., Dudley, J. P., et al. 2013, ApJ, 763, 147

Benson, B. A., Ade, P. A. R., Ahmed, Z., et al. 2014, in Society of Photo-Optical Instrumentation Engineers (SPIE) Conference Series, Vol. 9153, Society of Photo-Optical Instrumentation Engineers (SPIE) Conference Series

Beutler, F., Blake, C., Colless, M., et al. 2011, MNRAS, 416, 3017

Bleem, L. E., Stalder, B., de Haan, T., et al. 2015, ApJS, 216, 27

Bocquet, S., & Carter, F. W. 2016, The Journal of Open Source Software, 1, doi:10.21105/joss.00046

Bocquet, S., Saro, A., Dolag, K., & Mohr, J. J. 2016, MNRAS, 456, 2361

Bocquet, S., Saro, A., Mohr, J. J., et al. 2015, ApJ, 799, 214

Bulbul, E., Chiu, I., Mohr, J. J., et al. 2018, ArXiv e-prints, arXiv:1807.02556

Carlstrom, J. E., Ade, P. A. R., Aird, K. A., et al. 2011, PASP, 123, 568

Chiu, I., Mohr, J., McDonald, M., et al. 2016, MNRAS, 455, 258

Chiu, I., Mohr, J. J., McDonald, M., et al. 2018, MNRAS, 478, 3072

Dark Energy Survey Collaboration, Abbott, T., Abdalla, F. B., et al. 2016, MNRAS, 460, 1270

De Bernardis, F., Stevens, J. R., Hasselfield, M., et al. 2016, in Proc. SPIE, Vol. 9910, Observatory Operations: Strategies, Processes, and Systems VI, 991014

de Haan, T., Benson, B. A., Bleem, L. E., et al. 2016, ApJ, 832, 95

Dietrich, J. P., Bocquet, S., Schrabback, T., et al. 2017, ArXiv e-prints, arXiv:1711.05344

Duffy, A. R., Schaye, J., Kay, S. T., & Dalla Vecchia, C. 2008, MNRAS, 390, L64

Feroz, F., Hobson, M. P., & Bridges, M. 2009, MNRAS, 398, 1601

Giannantonio, T., Fosalba, P., Cawthon, R., et al. 2016, MNRAS, 456, 3213

Gralla, M. B., Gladders, M. D., Yee, H. K. C., & Barrientos, L. F. 2011, ApJ, 734, 103

Gupta, N., Saro, A., Mohr, J. J., Dolag, K., & Liu, J. 2017a, MNRAS, 469, 3069

Gupta, N., Saro, A., Mohr, J. J., et al. 2017b, MNRAS, 467, 3737

Haiman, Z., Mohr, J. J., & Holder, G. P. 2001, ApJ, 553, 545

Heitmann, K., Bingham, D., Lawrence, E., et al. 2016, ApJ, 820, 108

Hennig, C., Mohr, J. J., Zenteno, A., et al. 2017, MNRAS, 467, 4015

Hilton, M., Hasselfield, M., Sifón, C., et al. 2018, ApJS, 235, 20

Hoekstra, H., Herbonnet, R., Muzzin, A., et al. 2015, MNRAS, 449, 685

Hunter, J. D. 2007, Computing In Science & Engineering, 9, 90

Ichiki, K., & Takada, M. 2012, PhRvD, 85, 063521

---

[8] https://github.com/cmbant/getdist
[9] https://github.com/SebastianBocquet/pygtc

Ivezic, Z., Tyson, J. A., Abel, B., et al. 2008, ArXiv e-prints, arXiv:0805.2366

Jones, E., Oliphant, T., Peterson, P., et al. 2001–, SciPy: Open source scientific tools for Python, ,

Kaastra, J. S. 2017, A&A, 605, A51

Kaiser, N. 1986, MNRAS, 222, 323

Khullar, G., Bleem, L. E., Bayliss, M. B., et al. 2018, ArXiv e-prints, arXiv:1806.01962

Kravtsov, A. V., & Borgani, S. 2012, ARA&A, 50, 353

Kravtsov, A. V., Vikhlinin, A., & Nagai, D. 2006, ApJ, 650, 128

Laureijs, R., Amiaux, J., Arduini, S., et al. 2011, ArXiv e-prints, arXiv:1110.3193

Le Brun, A. M. C., McCarthy, I. G., Schaye, J., & Ponman, T. J. 2014, MNRAS, 441, 1270

Lin, Y., Partridge, B., Pober, J. C., et al. 2009, ApJ, 694, 992

Majumdar, S., & Mohr, J. J. 2004, ApJ, 613, 41

Mantz, A., Allen, S. W., Ebeling, H., Rapetti, D., & Drlica-Wagner, A. 2010a, MNRAS, 406, 1773

Mantz, A., Allen, S. W., Rapetti, D., & Ebeling, H. 2010b, MNRAS, 406, 1759

Mantz, A. B., von der Linden, A., Allen, S. W., et al. 2015, MNRAS, 446, 2205

Mantz, A. B., Allen, S. W., Morris, R. G., et al. 2016, MNRAS, 463, 3582

McClintock, T., Varga, T. N., Gruen, D., et al. 2018a, ArXiv e-prints, arXiv:1805.00039

McClintock, T., Rozo, E., Becker, M. R., et al. 2018b, ArXiv e-prints, arXiv:1804.05866

McDonald, M., Benson, B. A., Vikhlinin, A., et al. 2013, ApJ, 774, 23

McDonald, M., Allen, S. W., Bayliss, M., et al. 2017, ApJ, 843, 28

Melchior, P., Gruen, D., McClintock, T., et al. 2017, MNRAS, 469, 4899

Melin, J.-B., Bartlett, J. G., & Delabrouille, J. 2006, A&A, 459, 341

Metropolis, N., Rosenbluth, A. W., Rosenbluth, M. N., Teller, A. H., & Teller, E. 1953, JChPh, 21, 1087

Mohr, J. J., Mathiesen, B., & Evrard, A. E. 1999, ApJ, 517, 627

Peebles, P. 1980, The Large Scale Structure of the Universe (Princeton: Princeton University Press)

Planck Collaboration, Ade, P. A. R., Aghanim, N., et al. 2016a, A&A, 594, A13

—. 2016b, A&A, 594, A24

Planck Collaboration, Aghanim, N., Akrami, Y., et al. 2018, ArXiv e-prints, arXiv:1807.06209

Rapetti, D., Blake, C., Allen, S. W., et al. 2013, MNRAS, 432, 973

Reichardt, C. L., Stalder, B., Bleem, L. E., et al. 2013, ApJ, 763, 127

Ross, A. J., Samushia, L., Howlett, C., et al. 2015, Monthly Notices of the Royal Astronomical Society, 449, 835

Rykoff, E. S., Rozo, E., Hollowood, D., et al. 2016, ApJS, 224, 1

Saro, A., Bocquet, S., Rozo, E., et al. 2015, MNRAS, 454, 2305

Saro, A., Bocquet, S., Mohr, J., et al. 2017, MNRAS, 468, 3347

Schrabback, T., Applegate, D., Dietrich, J. P., et al. 2018a, MNRAS, 474, 2635

Schrabback, T., Schirmer, M., van der Burg, R. F. J., et al. 2018b, A&A, 610, A85

Scolnic, D. M., Jones, D. O., Rest, A., et al. 2018, ApJ, 859, 101

Sehgal, N., Bode, P., Das, S., et al. 2010, ApJ, 709, 920

Stalder, B., Stark, A. A., Amato, S. M., et al. 2014, in Proc. SPIE, Vol. 9147, Ground-based and Airborne Instrumentation for Astronomy V, 91473Y

Stern, C., Dietrich, J. P., Bocquet, S., et al. 2018, ArXiv e-prints, arXiv:1802.04533

Strazzullo, V., Pannella, M., Mohr, J. J., et al. 2018, ArXiv e-prints, arXiv:1807.09768

Sunyaev, R. A., & Zel'dovich, Y. B. 1972, Comments on Astrophysics and Space Physics, 4, 173

Tanabashi, M., Hagiwara, K., Hikasa, K., et al. 2018, Phys. Rev. D, 98, 030001

Tinker, J., Kravtsov, A. V., Klypin, A., et al. 2008, ApJ, 688, 709

van der Walt, S., Colbert, S. C., & Varoquaux, G. 2011, Computing in Science & Engineering, 13, 22

van Uitert, E., Joachimi, B., Joudaki, S., et al. 2018, MNRAS, arXiv:1706.05004

Vanderlinde, K., Crawford, T. M., de Haan, T., et al. 2010, ApJ, 722, 1180

Velliscig, M., van Daalen, M. P., Schaye, J., et al. 2014, MNRAS, 442, 2641

Vikhlinin, A., Burenin, R. A., Ebeling, H., et al. 2009a, ApJ, 692, 1033

Vikhlinin, A., Kravtsov, A. V., Burenin, R. A., et al. 2009b, ApJ, 692, 1060

von der Linden, A., Allen, M. T., Applegate, D. E., et al. 2014, MNRAS, 439, 2

Williamson, R., Benson, B. A., High, F. W., et al. 2011, ApJ, 738, 139

Wright, C. O., & Brainerd, T. G. 2000, ApJ, 534, 34

Zuntz, J., Paterno, M., Jennings, E., et al. 2015, Astronomy and Computing, 12, 45
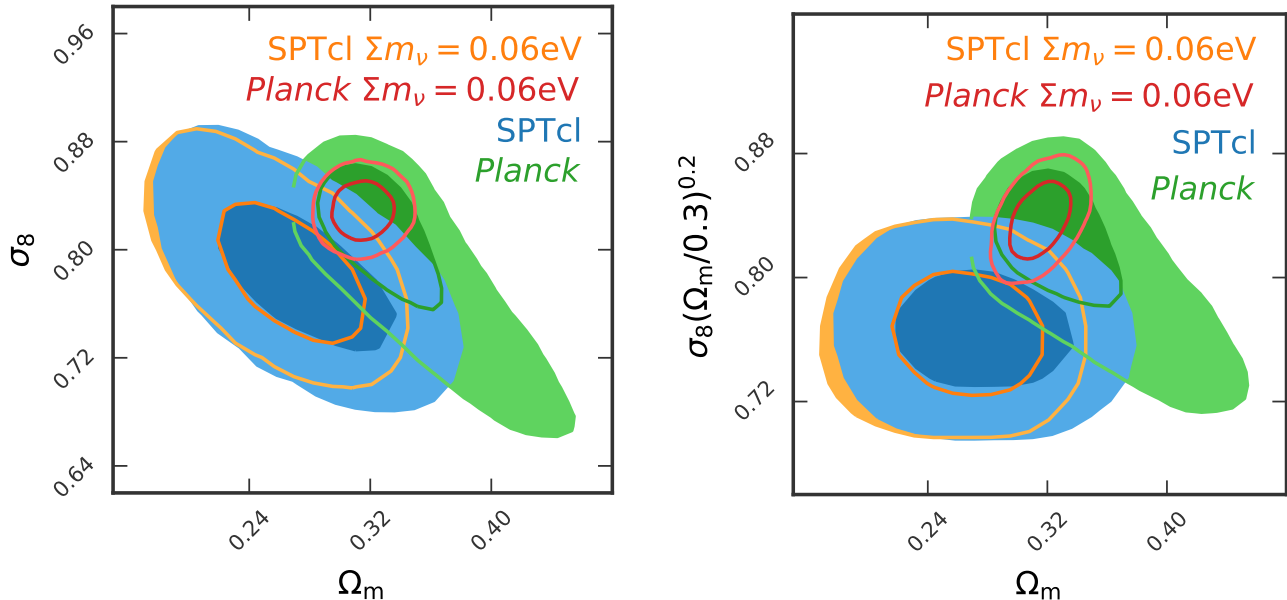
Figure 15. Impact of marginalization over $\Omega_\nu h^2$: The cluster constraints are weakly affected, whereas the *Planck* constraints significantly tighten when $\Omega_\nu h^2$ is fixed. Nevertheless, the level of (dis)agreement between these data sets is not substantially changed by marginalizing over $\Omega_\nu h^2$.

APPENDIX

A. IMPACT OF MARGINALIZATION OVER THE SUM OF NEUTRINO MASSES

Our baseline analysis is carried out marginalizing over the sum of neutrino masses (by allowing $\Omega_\nu h^2$ to vary in the range $0 \ldots 0.01$). In Fig. 15, we show that instead fixing the sum of neutrino masses to the minimum allowed value from oscillation experiments (0.06 eV, corresponding to $\Omega_\nu h^2 = 6.5 \times 10^{-4}$) does not qualitatively change the constraints in the $\Omega_m - \sigma_8$ space from our SPTcl data set. However, as is well known, the constraints from *Planck* tighten significantly when $\Omega_\nu h^2$ is fixed. We note that this tightening does not significantly affect the agreement between the two probes.

B. ΛCDM RESULTS: ROBUSTNESS TO SPLITS IN REDSHIFT AND IMPACT OF X-RAY DATA

Our baseline results are obtained from the SPTcl (SPT-SZ+WL+Y_X) data combination. Here, we show the impact on scaling relation parameters and cosmology from different cuts. Fig. 16 shows the most relevant subset of scaling relation and cosmological parameters for i) the baseline analysis, ii) an analysis of the low-redshift half of the cluster data ($0.25 < z < 0.6$), iii) the high-redshift half of the sample ($z > 0.6$), iv) the SPT-SZ+WL data combination, without any X-ray data, but where an informative Gaussian prior is applied on the SZ scatter ($\sigma_{\ln \zeta} = \mathcal{N}(0.13, 0.13^2)$).

Importantly, the cosmological constraints on $\Omega_m - \sigma_8$ are not much affected by the choice of subsample, and they only vary mildly along the degeneracy axis.

The low-redshift half of the sample only provides weak constraints on the redshift-evolution of the X-ray scaling relation C_{Y_X}. We discussed the constraints on the X-ray mass-slope B_{Y_X} in Section 4.1.5.

C. WCDM RESULTS: ROBUSTNESS TO DATA CUTS AND IMPACT OF X-RAY DATA

As in the previous section, here we discuss the impact of various data cuts on cosmological constraints, but this time in the context of the νwCDM model. Fig. 17 shows the most relevant subset of scaling relation and cosmological parameters for analyses of i) the baseline cluster sample, ii) the low-redshift half of the cluster data ($0.25 < z < 0.6$), iii) the high-redshift half of the sample ($z > 0.6$), iv) a subsample selected above SPT detection significance $\xi > 6.5$, and v) the SPT-SZ+WL data combination, without any X-ray data, but where an informative Gaussian prior is applied on the SZ scatter ($\sigma_{\ln \zeta} = \mathcal{N}(0.13, 0.13^2)$).

As discussed above for the $\nu\Lambda$CDM analysis, we see some shifts in the X-ray slope B_{Y_X} and redshift-evolution C_{Y_X}. The constraints on Ω_m and σ_8 are again not much affected by the choice of subsample. However, while not statistically
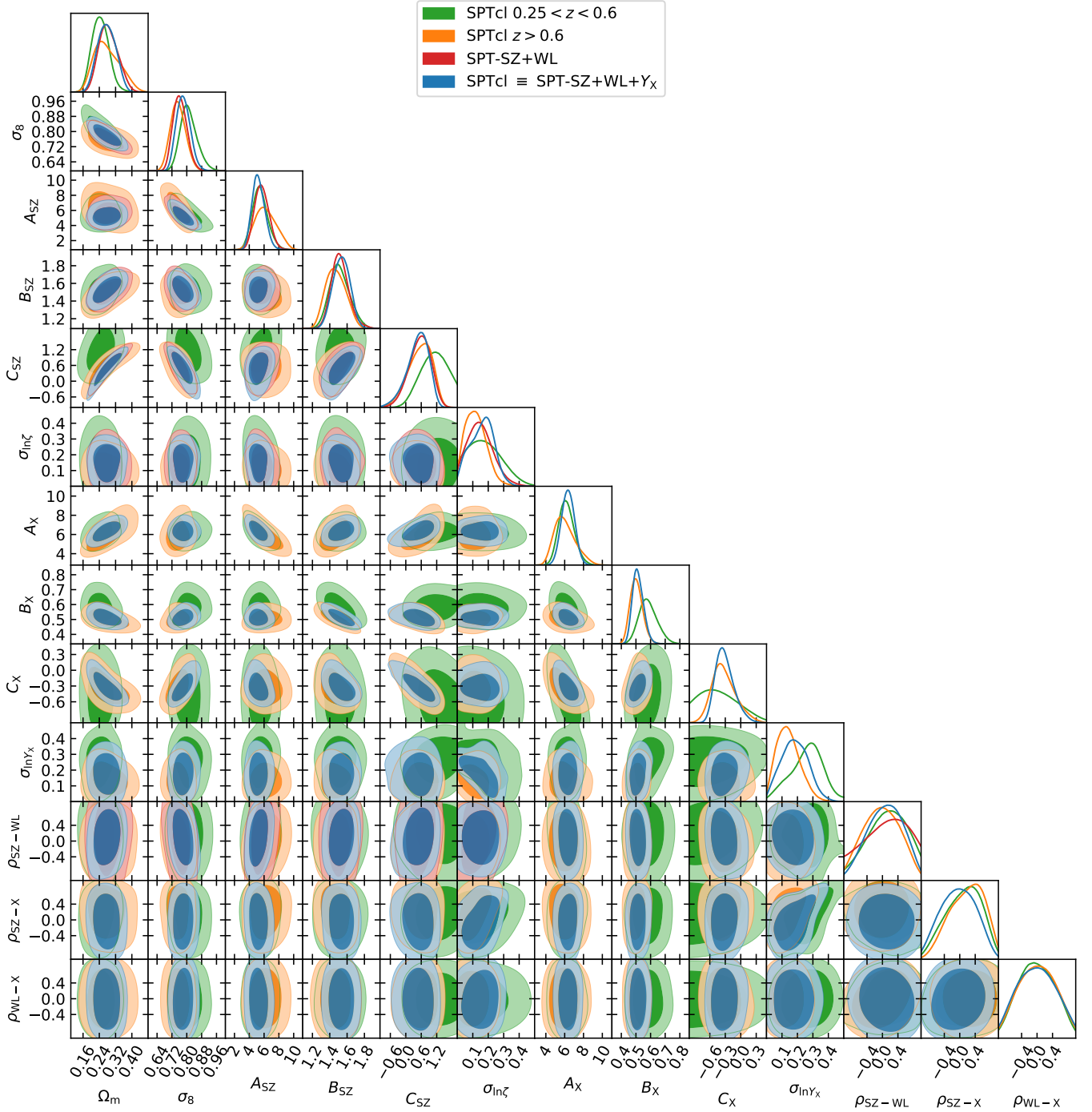
Figure 16. $\nu\Lambda$CDM constraints on a subset of cosmology and scaling relation parameters. The full set of fit parameters is listed in Table 2. *Blue contours* are obtained from the SPTcl (SPT-SZ+WL+$Y_{\rm X}$) dataset, *green contours* are obtained using all clusters in the redshift range $0.25 < z < 0.6$, and *orange contours* are obtained from the high-redshift counterpart $z > 0.6$, and *red contours* are obtained using SPT-SZ+WL, without any X-ray data, but with a Gaussian prior applied on $\sigma_{\ln\zeta}$. The inclusion of X-ray does not lead to improved cosmological constraints, but allows us to drop the prior on scatter $\sigma_{\ln\zeta}$ and to constrain the X-ray scaling relation. Our current dataset is not able to constrain any of the correlated scatter coefficients ρ. The visual impression that the ρ parameters are constrained is mostly due to the prior that the covariance matrix must be positive definite.

BOCQUET ET AL.
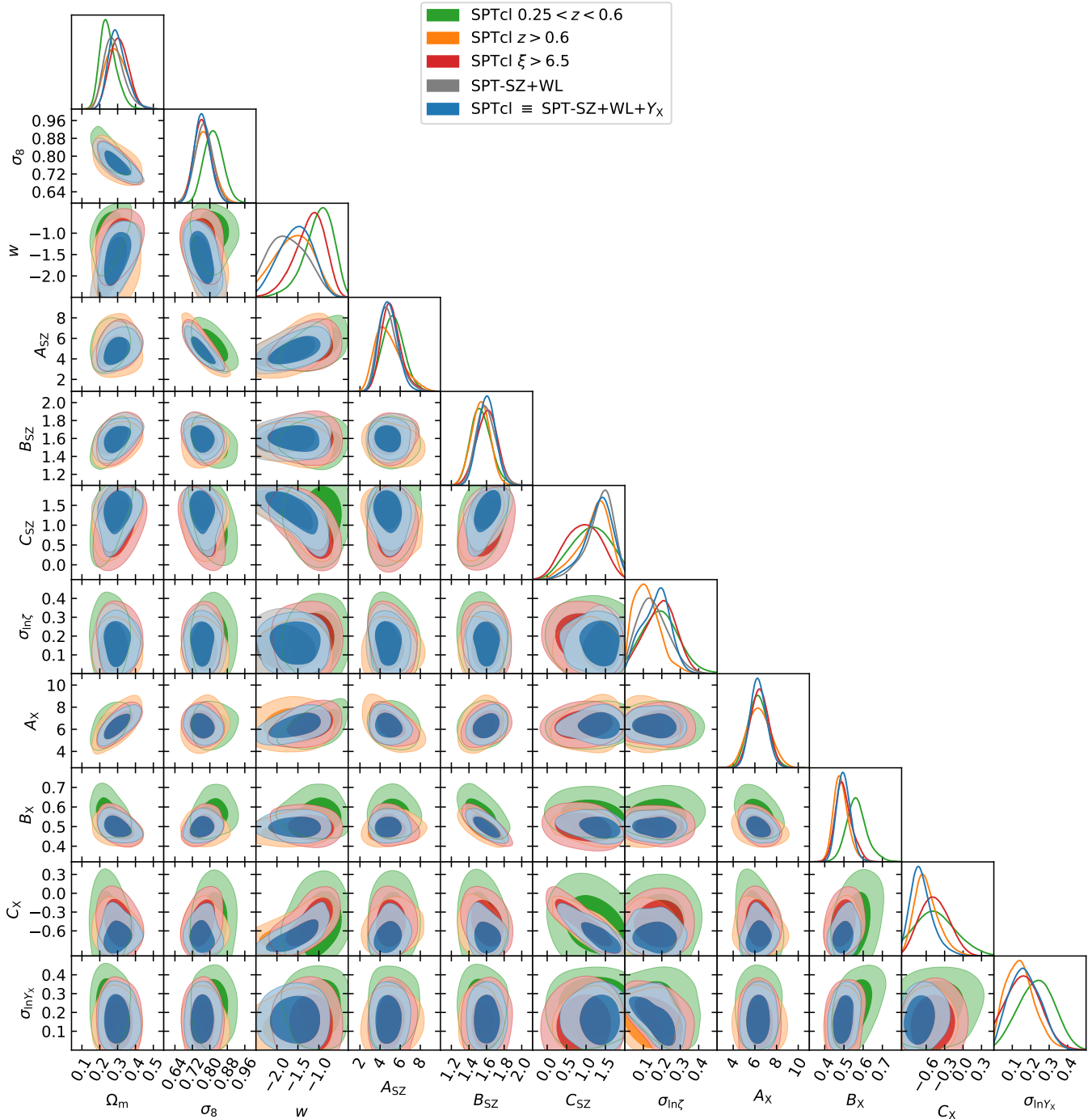
Figure 17. νwCDM constraints on a subset of cosmology and scaling relation parameters. The full set of fit parameters is listed in Table 2. *Blue contours* are obtained from the SPTcl (SPT-SZ+WL+Y_X) dataset, *green contours* are obtained using all clusters in the redshift range $0.25 < z < 0.6$, *orange contours* are obtained from the high-redshift counterpart $z > 0.6$, *red contours* are obtained from the subsample of clusters above SPT detection significance $\xi > 6.5$, and *gray contours* are obtained using SPT-SZ+WL without any X-ray data, but with a Gaussian prior applied on $\sigma_{\ln \zeta}$. Both the low-redshift half of the sample and the $\xi > 6.5$ subsample favor a less negative w in better agreement with a cosmological constant.

significant, there are differences in the recovered values for w. Using the SPT-SZ+WL data combination provides the weakest constraint on w, and its posterior distribution is shifted toward more negative values, running against the hard prior at $w = -2.5$. Then, as already discussed in Section 4.3, both the low-redshift half of the sample and the higher-mass $\xi > 6.5$ subsamples prefer slightly higher w, with $w(z < 0.6) = -1.01^{+0.41}_{-0.25}$ and $w(\xi > 6.5) = -1.21^{+0.42}_{-0.29}$. The high-redshift half of the sample provides constraints $w(z > 0.6) = -1.58 \pm 0.46$ that are very similar to those from the full sample $w = -1.55 \pm 0.41$.

D. THE CHOICE OF PRIORS: SAMPLING FROM A_S VS. SAMPLING FROM $\ln A_S$

In this work, we sample from a flat prior on A_s, following previous SPT analyses and e.g., the DES Y1 analysis (Abbott et al. 2018). In primary CMB studies however, it is common practice to sample from $\ln 10^{10} A_s$. We test the impact of this choice of priors by analyzing mock catalogs sampling from a flat prior on either A_s or $\ln 10^{10} A_s$. Fig. 18 shows that a flat prior on A_s performs better in terms of recovering the mock input parameters. This choice of prior does not matter in the limit where A_s (and/or $\ln 10^{10} A_s$) are tightly constrained and we thus expect the impact of this prior choice to become less important as the constraining power of our datasets increases. Sampling from a flat prior on σ_8 instead produces results that are essentially identical to those obtained when sampling from $\ln 10^{10} A_s$.
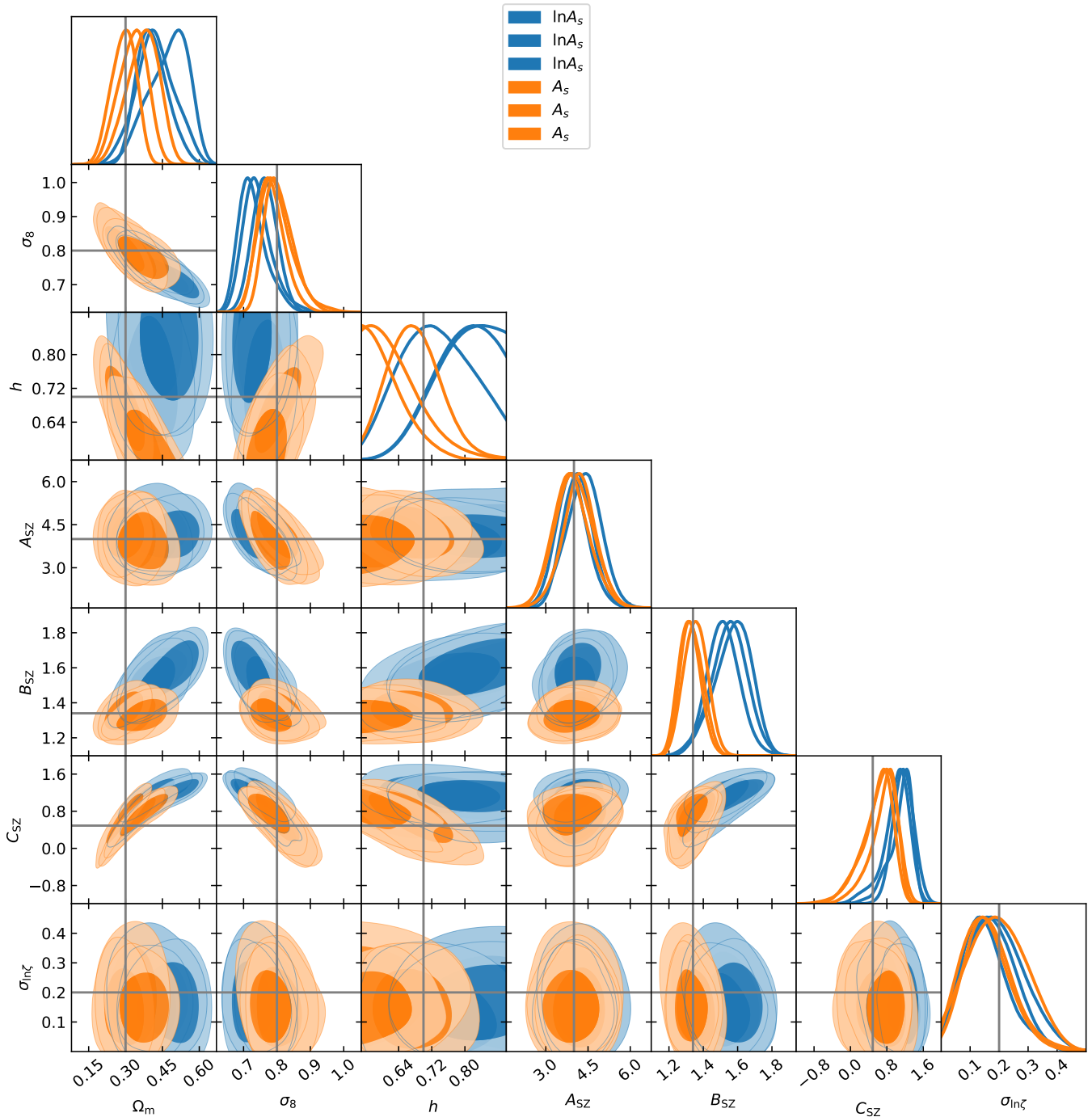
Figure 18. Constraints obtained running our analysis pipeline on three realizations of mock data. For simplicity, the mass calibration is replaced by Gaussian priors on $A_{\mathrm{SZ}} = \mathcal{N}(4, 0.8^2)$ and $\sigma_{\ln\zeta} = \mathcal{N}(0.13, 0.13^2)$. *Blue contours* are obtained sampling from a flat prior on $\ln(10^{10} A_s) = 1 \ldots 4$, *orange contours* are obtained sampling from a flat prior $A_s = 10^{-10} \ldots 10^{-8}$. The other parameters are sampled from flat priors. Solid lines show the mock catalog input parameters. Sampling from A_s performs better in terms of recovering the input values and we choose this prior throughout this analysis.

E. THE CLUSTER CATALOG

Table 5. Galaxy clusters with $\xi > 5$ and $z > 0.25$ in the SPT-SZ survey. Clusters with follow-up WL and/or X-ray data that we use in this work are marked with "WL" and/or "X". The positions, ξ, core radii θ_c, and Y_{SZ} are the same as presented in Bleem et al. (2015), while the redshifts marked with * have been updated. Spectroscopic redshifts are quoted without uncertainties. The mean mass estimates and mass uncertainties take the intrinsic and measurement scatter into account. We quote redshift lower limits for unconfirmed SZ detections. The mass estimates M_{500c} and M_{200c} are derived from the SPTcl dataset in the $\nu\Lambda$CDM model (Table 3 column 3) and are fully marginalized over cosmology and scaling relation parameter uncertainties. The estimates $M_{500c}^{\rm no\ syst.}$ are computed assuming a fixed cosmology and using the best-fit scaling relation parameters obtained from fitting the SPT-SZ number counts against that fixed cosmology (this approach was also adopted in Bleem et al. 2015). The full catalog with $\xi > 4.5$ can be found at https://pole.uchicago.edu/public/data/sptsz-clusters.

SPT ID	R.A.	DEC.	ξ	θ_c	Y_{SZ}	Redshift	M_{500c}	M_{200c}	$M_{500c}^{\rm no\ syst.}$
	(J2000)	(J2000)		arcmin	10^{-6}arcmin^2		$[10^{14}M_\odot/h_{70}]$	$[10^{14}M_\odot/h_{70}]$	$[10^{14}M_\odot/h_{70}]$
SPT-CL J0000-4356	0.0663	−43.9494	5.92	0.25	77 ± 21	$0.73 \pm 0.05^*$	$3.55^{+0.69}_{-0.81}$	$5.56^{+1.09}_{-1.30}$	$4.01^{+0.67}_{-0.74}$
SPT-CL J0000-5748$^{\rm WL,\ X}$	0.2499	−57.8064	8.49	0.50	83 ± 13	0.702	$4.36^{+0.65}_{-0.83}$	$6.83^{+1.03}_{-1.34}$	$4.88^{+0.59}_{-0.71}$
SPT-CL J0001-4024	0.3610	−40.4108	5.42	0.75	60 ± 13	$0.83 \pm 0.03^*$	$3.13^{+0.61}_{-0.82}$	$4.96^{+0.98}_{-1.33}$	$3.62^{+0.64}_{-0.73}$
SPT-CL J0001-4842	0.2768	−48.7132	5.69	1.25	78 ± 13	$0.33 \pm 0.02^*$	$3.90^{+0.79}_{-0.91}$	$5.91^{+1.22}_{-1.41}$	$4.48^{+0.75}_{-0.83}$
SPT-CL J0001-5440	0.4059	−54.6697	5.69	1.00	60 ± 13	$0.82 \pm 0.08^*$	$3.37^{+0.60}_{-0.86}$	$5.35^{+0.97}_{-1.39}$	$3.88^{+0.67}_{-0.75}$
SPT-CL J0002-5557	0.5138	−55.9621	5.20	0.25	55 ± 18	1.15 ± 0.10	$2.87^{+0.56}_{-0.80}$	$4.60^{+0.91}_{-1.32}$	$3.19^{+0.56}_{-0.68}$
SPT-CL J0011-4614	2.9779	−46.2351	5.12	0.75	63 ± 17	$0.54 \pm 0.04^*$	$3.39^{+0.65}_{-0.84}$	$5.23^{+1.02}_{-1.33}$	$3.87^{+0.67}_{-0.82}$
SPT-CL J0013-4906$^{\rm X}$	3.3290	−49.1151	11.22	0.75	135 ± 13	0.407	$6.35^{+0.94}_{-1.10}$	$9.82^{+1.48}_{-1.75}$	$7.12^{+0.76}_{-0.93}$
SPT-CL J0013-5714	3.3029	−57.2373	5.11	1.50	60 ± 13	> 0.86	$\cdots$	$\cdots$	$\cdots$
SPT-CL J0014-4036	3.7433	−40.6031	9.72	0.25	113 ± 15	$0.52 \pm 0.04^*$	$5.41^{+0.81}_{-1.00}$	$8.43^{+1.28}_{-1.60}$	$6.14^{+0.69}_{-0.84}$
SPT-CL J0014-4952$^{\rm X}$	3.6969	−49.8772	8.87	0.25	124 ± 27	0.752	$5.05^{+0.76}_{-0.98}$	$7.98^{+1.23}_{-1.58}$	$5.60^{+0.65}_{-0.79}$
SPT-CL J0015-6000	3.8824	−60.0001	5.11	0.25	68 ± 20	$0.70 \pm 0.04^*$	$3.18^{+0.61}_{-0.81}$	$4.96^{+0.97}_{-1.30}$	$3.62^{+0.63}_{-0.76}$
SPT-CL J0019-4051	4.7600	−40.8596	9.67	0.50	114 ± 14	$0.48 \pm 0.04^*$	$5.52^{+0.85}_{-0.98}$	$8.53^{+1.33}_{-1.56}$	$6.18^{+0.69}_{-0.85}$
SPT-CL J0019-5527	4.8313	−55.4528	6.21	0.25	90 ± 20	$0.91 \pm 0.03^*$	$3.59^{+0.67}_{-0.83}$	$5.69^{+1.07}_{-1.35}$	$4.01^{+0.64}_{-0.71}$
SPT-CL J0021-4902	5.3811	−49.0360	5.32	0.50	68 ± 13	$0.64 \pm 0.04^*$	$3.42^{+0.67}_{-0.86}$	$5.32^{+1.05}_{-1.36}$	$3.87^{+0.67}_{-0.80}$
SPT-CL J0022-4144	5.5489	−41.7366	5.14	0.50	65 ± 12	$0.30 \pm 0.02^*$	$3.48^{+0.71}_{-0.87}$	$5.26^{+1.09}_{-1.35}$	$4.05^{+0.71}_{-0.84}$
SPT-CL J0025-4133	6.4915	−41.5540	6.59	0.50	83 ± 16	$0.54 \pm 0.04^*$	$4.09^{+0.69}_{-0.85}$	$6.34^{+1.09}_{-1.34}$	$4.64^{+0.68}_{-0.77}$
SPT-CL J0027-4742	6.9158	−47.7151	6.40	0.50	84 ± 16	0.75 ± 0.05	$3.90^{+0.69}_{-0.86}$	$6.13^{+1.09}_{-1.39}$	$4.40^{+0.67}_{-0.75}$
SPT-CL J0027-5015	6.8228	−50.2524	5.00	0.50	25 ± 10	0.145	$3.61^{+0.74}_{-0.91}$	$5.38^{+1.11}_{-1.39}$	$4.24^{+0.74}_{-0.89}$
SPT-CL J0033-6326$^{\rm X}$	8.4767	−63.4463	7.50	0.75	82 ± 14	0.597	$4.49^{+0.73}_{-0.92}$	$6.99^{+1.15}_{-1.47}$	$5.08^{+0.66}_{-0.78}$
SPT-CL J0036-4411	9.1758	−44.1849	5.66	0.75	74 ± 22	0.869	$3.32^{+0.64}_{-0.82}$	$5.25^{+1.02}_{-1.33}$	$3.70^{+0.64}_{-0.72}$
SPT-CL J0037-5047$^{\rm X}$	9.4441	−50.7971	6.93	0.25	88 ± 15	1.026	$3.91^{+0.67}_{-0.93}$	$6.26^{+1.10}_{-1.52}$	$4.33^{+0.63}_{-0.70}$
SPT-CL J0040-4407$^{\rm X}$	10.2048	−44.1329	19.34	0.50	219 ± 14	0.350	$8.91^{+1.23}_{-1.49}$	$13.81^{+1.94}_{-2.37}$	$9.81^{+0.95}_{-1.21}$
SPT-CL J0041-4428	10.2513	−44.4785	8.84	0.50	101 ± 12	0.33 ± 0.02	$5.29^{+0.79}_{-0.99}$	$8.09^{+1.22}_{-1.54}$	$6.05^{+0.71}_{-0.86}$
SPT-CL J0043-4843	10.9696	−48.7235	5.17	0.75	60 ± 13	$0.88 \pm 0.03^*$	$3.15^{+0.66}_{-0.86}$	$4.96^{+1.06}_{-1.38}$	$3.53^{+0.60}_{-0.75}$
SPT-CL J0047-4506	11.8207	−45.1131	7.55	0.50	88 ± 15	$0.47 \pm 0.04^*$	$4.66^{+0.75}_{-0.92}$	$7.15^{+1.17}_{-1.45}$	$5.24^{+0.68}_{-0.80}$
SPT-CL J0048-5244	12.0901	−52.7487	6.31	0.25	83 ± 23	$0.98 \pm 0.09^*$	$3.66^{+0.62}_{-0.90}$	$5.83^{+1.01}_{-1.47}$	$4.06^{+0.64}_{-0.71}$
SPT-CL J0048-6416	12.2372	−64.2690	5.57	0.25	67 ± 15	$0.90 \pm 0.03^*$	$3.23^{+0.63}_{-0.83}$	$5.13^{+1.02}_{-1.35}$	$3.65^{+0.62}_{-0.73}$
SPT-CL J0049-5315	12.3825	−53.2505	6.35	0.25	76 ± 13	$0.66 \pm 0.04^*$	$3.97^{+0.73}_{-0.85}$	$6.20^{+1.17}_{-1.37}$	$4.48^{+0.69}_{-0.77}$
SPT-CL J0051-4834	12.7905	−48.5776	7.39	1.25	81 ± 12	0.187	$4.88^{+0.86}_{-0.96}$	$7.36^{+1.32}_{-1.48}$	$5.69^{+0.75}_{-0.87}$
SPT-CL J0052-4551	13.1930	−45.8605	5.09	0.25	69 ± 15	$0.36 \pm 0.02^*$	$3.54^{+0.71}_{-0.88}$	$5.38^{+1.09}_{-1.37}$	$4.06^{+0.71}_{-0.85}$
SPT-CL J0054-4046	13.5908	−40.7759	5.44	0.75	64 ± 13	$0.41 \pm 0.04^*$	$3.56^{+0.70}_{-0.84}$	$5.43^{+1.09}_{-1.31}$	$4.11^{+0.71}_{-0.80}$
SPT-CL J0058-6145$^{\rm X}$	14.5799	−61.7635	7.52	0.25	98 ± 25	0.82 ± 0.03	$4.24^{+0.68}_{-0.89}$	$6.74^{+1.10}_{-1.45}$	$4.78^{+0.63}_{-0.74}$
SPT-CL J0102-4603$^{\rm X}$	15.6690	−46.0647	7.33	0.25	100 ± 24	0.840^*	$4.27^{+0.68}_{-0.90}$	$6.77^{+1.09}_{-1.47}$	$4.76^{+0.64}_{-0.74}$
SPT-CL J0102-4915$^{\rm WL,\ X}$	15.7294	−49.2611	39.91	0.75	487 ± 12	0.870	$13.11^{+2.08}_{-2.85}$	$21.37^{+3.45}_{-4.76}$	$13.52^{+1.31}_{-1.57}$
SPT-CL J0103-4250	15.9144	−42.8334	6.60	0.25	86 ± 22	$0.71 \pm 0.04^*$	$3.93^{+0.67}_{-0.84}$	$6.16^{+1.07}_{-1.36}$	$4.42^{+0.66}_{-0.74}$
SPT-CL J0104-4351	16.1290	−43.8640	7.35	0.25	97 ± 24	$0.85 \pm 0.08^*$	$4.06^{+0.68}_{-0.89}$	$6.46^{+1.10}_{-1.45}$	$4.62^{+0.62}_{-0.72}$

Table 5 continued

BOCQUET ET AL.

Table 5 *(continued)*

SPT ID	R.A. (J2000)	DEC. (J2000)	ξ	θ_c arcmin	Y_{SZ} 10^{-6}arcmin^2	Redshift	M_{500c} $[10^{14}M_\odot/h_{70}]$	M_{200c} $[10^{14}M_\odot/h_{70}]$	$M_{500c}^{\text{no syst.}}$ $[10^{14}M_\odot/h_{70}]$
SPT-CL J0106-5943[X]	16.6152	−59.7214	9.57	0.50	115 ± 16	0.348	$5.62^{+0.82}_{-1.00}$	$8.62^{+1.27}_{-1.57}$	$6.40^{+0.72}_{-0.88}$
SPT-CL J0107-5833	16.9102	−58.5520	5.10	0.25	71 ± 22	1.23 ± 0.10	$2.77^{+0.53}_{-0.79}$	$4.45^{+0.87}_{-1.31}$	$3.07^{+0.52}_{-0.67}$
SPT-CL J0108-4659	17.1387	−46.9955	5.20	0.25	73 ± 22	1.20 ± 0.10	$2.89^{+0.53}_{-0.83}$	$4.64^{+0.86}_{-1.37}$	$3.21^{+0.56}_{-0.69}$
SPT-CL J0110-4445	17.5861	−44.7596	7.91	1.50	82 ± 12	$0.36 \pm 0.02^*$	$4.85^{+0.76}_{-0.91}$	$7.44^{+1.18}_{-1.43}$	$5.57^{+0.69}_{-0.83}$
SPT-CL J0111-5424	17.7686	−54.4151	5.31	1.25	54 ± 13	$0.48 \pm 0.04^*$	$3.57^{+0.67}_{-0.86}$	$5.48^{+1.04}_{-1.35}$	$4.06^{+0.71}_{-0.82}$
SPT-CL J0114-4123	18.6812	−41.3968	11.43	1.50	128 ± 12	$0.39 \pm 0.04^*$	$6.25^{+0.90}_{-1.08}$	$9.64^{+1.40}_{-1.71}$	$7.03^{+0.74}_{-0.92}$
SPT-CL J0117-6032	19.3645	−60.5403	6.87	0.75	78 ± 16	$0.99 \pm 0.09^*$	$3.77^{+0.65}_{-0.90}$	$6.04^{+1.05}_{-1.47}$	$4.26^{+0.60}_{-0.70}$
SPT-CL J0118-5156	19.5990	−51.9434	5.97	0.25	81 ± 21	0.705	$3.70^{+0.72}_{-0.88}$	$5.80^{+1.14}_{-1.41}$	$4.19^{+0.69}_{-0.76}$
SPT-CL J0118-5638	19.5385	−56.6339	5.10	1.25	54 ± 13	0.21 ± 0.04	$3.56^{+0.73}_{-0.90}$	$5.34^{+1.11}_{-1.38}$	$4.15^{+0.73}_{-0.86}$
SPT-CL J0119-5919	19.9065	−59.3293	5.01	1.00	60 ± 18	0.62 ± 0.03	$3.18^{+0.63}_{-0.82}$	$4.92^{+0.98}_{-1.31}$	$3.64^{+0.62}_{-0.79}$
SPT-CL J0123-4821[X]	20.7923	−48.3588	6.92	0.25	91 ± 14	0.655^*	$4.25^{+0.72}_{-0.90}$	$6.65^{+1.14}_{-1.45}$	$4.80^{+0.67}_{-0.77}$
SPT-CL J0124-4301	21.1454	−43.0208	5.25	1.25	62 ± 13	0.47 ± 0.04	$3.42^{+0.67}_{-0.83}$	$5.25^{+1.05}_{-1.30}$	$3.93^{+0.68}_{-0.81}$
SPT-CL J0124-5937	21.1988	−59.6255	5.88	0.50	63 ± 14	0.21 ± 0.03	$3.98^{+0.76}_{-0.93}$	$5.98^{+1.17}_{-1.44}$	$4.65^{+0.80}_{-0.93}$
SPT-CL J0129-6432	22.4347	−64.5449	10.25	1.25	101 ± 12	0.326	$5.91^{+0.89}_{-1.06}$	$9.06^{+1.39}_{-1.66}$	$6.73^{+0.75}_{-0.90}$
SPT-CL J0131-5604	22.9331	−56.0821	6.60	0.75	82 ± 13	$0.75 \pm 0.05^*$	$3.84^{+0.72}_{-0.86}$	$6.06^{+1.15}_{-1.39}$	$4.41^{+0.66}_{-0.73}$
SPT-CL J0131-5921	22.8565	−59.3617	5.95	0.25	89 ± 19	$1.02 \pm 0.09^*$	$3.34^{+0.63}_{-0.86}$	$5.32^{+1.01}_{-1.41}$	$3.73^{+0.62}_{-0.70}$
SPT-CL J0133-6434	23.4103	−64.5668	9.15	2.00	109 ± 13	$0.32 \pm 0.02^*$	$5.50^{+0.84}_{-1.01}$	$8.39^{+1.31}_{-1.57}$	$6.26^{+0.73}_{-0.88}$
SPT-CL J0135-5902	23.7918	−59.0361	5.05	0.25	65 ± 17	0.51 ± 0.04	$3.31^{+0.66}_{-0.80}$	$5.09^{+1.03}_{-1.27}$	$3.79^{+0.66}_{-0.81}$
SPT-CL J0139-5204	24.8989	−52.0825	5.12	0.25	72 ± 22	$0.93 \pm 0.03^*$	$3.09^{+0.62}_{-0.85}$	$4.89^{+1.00}_{-1.38}$	$3.44^{+0.59}_{-0.74}$
SPT-CL J0142-5032	25.5452	−50.5438	10.12	0.75	117 ± 13	0.679^*	$5.45^{+0.77}_{-1.01}$	$8.58^{+1.24}_{-1.63}$	$6.05^{+0.68}_{-0.82}$
SPT-CL J0143-4452	25.8853	−44.8741	5.03	1.50	57 ± 13	0.27 ± 0.03	$3.45^{+0.69}_{-0.88}$	$5.21^{+1.05}_{-1.36}$	$4.00^{+0.69}_{-0.84}$
SPT-CL J0144-4157	26.1463	−41.9601	5.16	0.50	55 ± 14	> 0.79	$\cdots$	$\cdots$	$\cdots$
SPT-CL J0145-5301	26.2645	−53.0295	7.37	2.50	84 ± 17	0.117	$4.79^{+0.83}_{-0.97}$	$7.17^{+1.27}_{-1.49}$	$5.61^{+0.73}_{-0.87}$
SPT-CL J0145-6033	26.2958	−60.5594	10.76	0.50	119 ± 17	0.179	$6.27^{+0.94}_{-1.10}$	$9.50^{+1.44}_{-1.70}$	$7.17^{+0.78}_{-0.95}$
SPT-CL J0148-4518	27.0985	−45.3023	5.12	0.50	59 ± 19	$0.57 \pm 0.04^*$	$3.25^{+0.68}_{-0.81}$	$5.02^{+1.07}_{-1.29}$	$3.73^{+0.64}_{-0.79}$
SPT-CL J0150-4511	27.6483	−45.1894	7.19	1.25	81 ± 12	$0.31 \pm 0.02^*$	$4.57^{+0.78}_{-0.92}$	$6.96^{+1.21}_{-1.44}$	$5.28^{+0.71}_{-0.82}$
SPT-CL J0151-5954[X]	27.8597	−59.9059	7.73	0.25	104 ± 27	$0.97 \pm 0.03^*$	$4.16^{+0.68}_{-0.95}$	$6.67^{+1.11}_{-1.57}$	$4.68^{+0.60}_{-0.71}$
SPT-CL J0152-5303	28.2342	−53.0540	6.87	0.75	78 ± 14	$0.61 \pm 0.04^*$	$4.21^{+0.72}_{-0.85}$	$6.53^{+1.13}_{-1.35}$	$4.70^{+0.66}_{-0.76}$
SPT-CL J0154-4824	28.5911	−48.4068	5.47	0.25	79 ± 21	$1.28 \pm 0.10^*$	$2.87^{+0.54}_{-0.81}$	$4.64^{+0.88}_{-1.35}$	$3.19^{+0.55}_{-0.65}$
SPT-CL J0156-5541[X]	29.0449	−55.6980	6.98	0.25	97 ± 25	1.288^*	$3.44^{+0.84}_{-0.92}$	$5.59^{+1.39}_{-1.54}$	$3.96^{+0.57}_{-0.65}$
SPT-CL J0157-4007	29.4494	−40.1263	5.75	1.50	63 ± 12	$0.57 \pm 0.04^*$	$3.63^{+0.67}_{-0.85}$	$5.61^{+1.05}_{-1.35}$	$4.12^{+0.69}_{-0.76}$
SPT-CL J0157-6442	29.4831	−64.7060	5.65	0.25	75 ± 22	$0.86 \pm 0.03^*$	$3.30^{+0.67}_{-0.83}$	$5.21^{+1.07}_{-1.35}$	$3.75^{+0.64}_{-0.72}$
SPT-CL J0200-4852[X]	30.1436	−48.8757	7.38	0.75	84 ± 13	0.498	$4.50^{+0.73}_{-0.89}$	$6.96^{+1.14}_{-1.40}$	$5.11^{+0.68}_{-0.79}$
SPT-CL J0201-6051	30.3953	−60.8586	5.06	0.25	66 ± 19	> 1.50	$\cdots$	$\cdots$	$\cdots$
SPT-CL J0202-5401	30.5756	−54.0242	5.65	1.00	59 ± 12	0.55 ± 0.04	$3.58^{+0.68}_{-0.84}$	$5.53^{+1.06}_{-1.32}$	$4.07^{+0.70}_{-0.78}$
SPT-CL J0205-5829[X]	31.4428	−58.4852	10.40	0.25	132 ± 29	1.322	$4.56^{+0.77}_{-1.13}$	$7.47^{+1.28}_{-1.90}$	$5.06^{+0.55}_{-0.68}$
SPT-CL J0205-6432	31.2794	−64.5457	5.83	0.50	66 ± 14	0.744	$3.40^{+0.61}_{-0.81}$	$5.33^{+0.97}_{-1.30}$	$3.84^{+0.64}_{-0.71}$
SPT-CL J0212-4657[X]	33.1061	−46.9502	10.05	0.75	115 ± 14	0.654	$5.45^{+0.78}_{-1.00}$	$8.56^{+1.24}_{-1.62}$	$6.06^{+0.67}_{-0.82}$
SPT-CL J0214-4638	33.7017	−46.6483	6.50	1.75	63 ± 12	$0.30 \pm 0.02^*$	$4.26^{+0.75}_{-0.90}$	$6.45^{+1.15}_{-1.39}$	$4.90^{+0.72}_{-0.81}$
SPT-CL J0216-4219	34.0628	−42.3281	5.82	0.75	60 ± 13	0.62 ± 0.04	$3.59^{+0.63}_{-0.87}$	$5.58^{+0.99}_{-1.38}$	$4.07^{+0.68}_{-0.75}$
SPT-CL J0216-4830	34.0723	−48.5147	6.23	0.50	71 ± 15	0.47 ± 0.03	$3.93^{+0.80}_{-0.84}$	$6.05^{+1.19}_{-1.36}$	$4.52^{+0.70}_{-0.78}$
SPT-CL J0216-5730	34.1384	−57.5095	5.05	0.50	57 ± 12	> 0.80	$\cdots$	$\cdots$	$\cdots$
SPT-CL J0216-6409	34.1743	−64.1559	5.35	0.25	59 ± 16	0.65 ± 0.04	$3.23^{+0.61}_{-0.80}$	$5.02^{+0.96}_{-1.27}$	$3.67^{+0.65}_{-0.74}$
SPT-CL J0217-4310	34.4138	−43.1819	6.54	1.75	69 ± 12	$0.57 \pm 0.04^*$	$4.02^{+0.68}_{-0.84}$	$6.24^{+1.08}_{-1.33}$	$4.55^{+0.67}_{-0.76}$
SPT-CL J0217-5245[X]	34.3035	−52.7560	6.46	0.50	78 ± 14	0.343	$4.18^{+0.76}_{-0.87}$	$6.37^{+1.18}_{-1.36}$	$4.82^{+0.71}_{-0.68}$
SPT-CL J0218-4315	34.5775	−43.2606	9.85	0.75	109 ± 12	$0.63 \pm 0.04^*$	$5.37^{+0.79}_{-1.01}$	$8.42^{+1.25}_{-1.62}$	$6.00^{+0.67}_{-0.82}$
SPT-CL J0219-4934	34.8102	−49.5762	6.38	0.25	81 ± 17	$0.55 \pm 0.04^*$	$3.94^{+0.70}_{-0.85}$	$6.11^{+1.10}_{-1.35}$	$4.52^{+0.70}_{-0.76}$
SPT-CL J0221-4446	35.4173	−44.7792	5.23	0.25	69 ± 18	$0.50 \pm 0.04^*$	$3.33^{+0.66}_{-0.83}$	$5.15^{+1.04}_{-1.31}$	$3.85^{+0.67}_{-0.68}$
SPT-CL J0225-4155	36.4770	−41.9177	6.92	1.75	93 ± 13	0.220	$4.48^{+0.77}_{-0.93}$	$6.76^{+1.18}_{-1.44}$	$5.21^{+0.72}_{-0.83}$
SPT-CL J0225-4327	36.2951	−43.4567	5.37	0.25	58 ± 13	0.23 ± 0.03	$3.65^{+0.72}_{-0.88}$	$5.49^{+1.09}_{-1.35}$	$4.25^{+0.73}_{-0.83}$
SPT-CL J0230-6028	37.6418	−60.4689	6.01	0.25	74 ± 18	$0.67 \pm 0.04^*$	$3.54^{+0.66}_{-0.79}$	$5.53^{+1.04}_{-1.27}$	$4.02^{+0.66}_{-0.72}$

Table 5 continued

Table 5 *(continued)*

SPT ID	R.A.	DEC.	ξ	θ_c	Y_{SZ}	Redshift	M_{500c}	M_{200c}	$M_{500c}^{\text{no syst.}}$
	(J2000)	(J2000)		arcmin	10^{-6}arcmin^2		$[10^{14}M_\odot/h_{70}]$	$[10^{14}M_\odot/h_{70}]$	$[10^{14}M_\odot/h_{70}]$
SPT-CL J0231-4427	37.7508	−44.4640	5.42	0.50	63 ± 14	$0.60 \pm 0.04^*$	$3.38^{+0.67}_{-0.80}$	$5.24^{+1.05}_{-1.27}$	$3.86^{+0.67}_{-0.77}$
SPT-CL J0231-5403	37.7768	−54.0563	5.22	0.50	60 ± 13	0.59 ± 0.04	$3.33^{+0.66}_{-0.84}$	$5.15^{+1.03}_{-1.32}$	$3.77^{+0.66}_{-0.78}$
SPT-CL J0232-4421$^{\text{X}}$	38.0701	−44.3541	23.96	1.00	254 ± 13	0.284	$10.39^{+1.46}_{-1.73}$	$16.06^{+2.30}_{-2.74}$	$11.30^{+1.11}_{-1.36}$
SPT-CL J0232-5257$^{\text{X}}$	38.1876	−52.9578	8.65	0.75	97 ± 12	0.556	$5.00^{+0.76}_{-0.95}$	$7.78^{+1.21}_{-1.51}$	$5.63^{+0.66}_{-0.81}$
SPT-CL J0233-5819	38.2552	−58.3274	6.55	1.25	73 ± 12	0.664	$3.82^{+0.65}_{-0.81}$	$5.96^{+1.03}_{-1.29}$	$4.33^{+0.65}_{-0.72}$
SPT-CL J0234-5831$^{\text{WL, X}}$	38.6786	−58.5214	14.66	0.50	169 ± 14	0.415	$7.13^{+0.99}_{-1.20}$	$11.06^{+1.57}_{-1.90}$	$7.93^{+0.80}_{-0.99}$
SPT-CL J0235-5121$^{\text{X}}$	38.9468	−51.3516	9.78	2.00	116 ± 19	0.278	$5.74^{+0.89}_{-1.04}$	$8.76^{+1.38}_{-1.62}$	$6.56^{+0.73}_{-0.89}$
SPT-CL J0236-4938	39.2477	−49.6356	5.80	1.00	67 ± 12	0.334	$3.81^{+0.72}_{-0.86}$	$5.79^{+1.11}_{-1.34}$	$4.42^{+0.77}_{-0.78}$
SPT-CL J0238-4904	39.6994	−49.0710	5.77	1.00	63 ± 13	$0.52 \pm 0.04^*$	$3.68^{+0.67}_{-0.86}$	$5.66^{+1.05}_{-1.36}$	$4.18^{+0.71}_{-0.78}$
SPT-CL J0240-5946$^{\text{WL}}$	40.1606	−59.7697	8.84	0.75	100 ± 12	0.400	$5.08^{+0.74}_{-0.96}$	$7.81^{+1.16}_{-1.50}$	$5.79^{+0.69}_{-0.82}$
SPT-CL J0242-4150	40.5347	−41.8360	5.04	0.50	60 ± 14	0.70 ± 0.04	$3.09^{+0.57}_{-0.79}$	$4.82^{+0.90}_{-1.27}$	$3.53^{+0.60}_{-0.76}$
SPT-CL J0242-4944	40.5470	−49.7376	6.25	0.25	83 ± 22	$0.75 \pm 0.05^*$	$3.66^{+0.64}_{-0.85}$	$5.77^{+1.02}_{-1.38}$	$4.18^{+0.66}_{-0.72}$
SPT-CL J0243-4833	40.9139	−48.5602	13.90	0.75	153 ± 12	0.498	$6.97^{+1.01}_{-1.21}$	$10.87^{+1.61}_{-1.93}$	$7.74^{+0.79}_{-0.97}$
SPT-CL J0243-5930$^{\text{X}}$	40.8615	−59.5124	7.67	0.25	95 ± 21	0.635	$4.34^{+0.70}_{-0.89}$	$6.78^{+1.12}_{-1.42}$	$4.92^{+0.64}_{-0.75}$
SPT-CL J0244-4857	41.0310	−48.9606	5.93	1.75	72 ± 14	$0.41 \pm 0.04^*$	$3.77^{+0.74}_{-0.83}$	$5.79^{+1.15}_{-1.31}$	$4.41^{+0.72}_{-0.80}$
SPT-CL J0249-5658	42.4065	−56.9770	5.45	1.00	61 ± 12	0.235	$3.56^{+0.73}_{-0.85}$	$5.36^{+1.12}_{-1.30}$	$4.19^{+0.72}_{-0.82}$
SPT-CL J0252-4824$^{\text{X}}$	43.1881	−48.4124	7.03	0.25	86 ± 15	0.421	$4.40^{+0.75}_{-0.90}$	$6.77^{+1.17}_{-1.41}$	$5.04^{+0.69}_{-0.80}$
SPT-CL J0254-5857$^{\text{WL}}$	43.5729	−58.9526	14.13	1.50	151 ± 12	0.438	$6.93^{+1.00}_{-1.17}$	$10.76^{+1.58}_{-1.87}$	$7.72^{+0.78}_{-0.97}$
SPT-CL J0254-6051	43.6007	−60.8641	6.55	1.00	70 ± 12	0.44 ± 0.04	$4.00^{+0.71}_{-0.86}$	$6.15^{+1.11}_{-1.35}$	$4.60^{+0.68}_{-0.77}$
SPT-CL J0256-4243	44.0543	−42.7329	5.09	0.75	63 ± 12	$0.63 \pm 0.04^*$	$3.24^{+0.63}_{-0.79}$	$5.02^{+0.99}_{-1.25}$	$3.64^{+0.63}_{-0.77}$
SPT-CL J0256-4736	44.2405	−47.6110	7.04	0.75	77 ± 13	0.23 ± 0.03	$4.56^{+0.78}_{-0.91}$	$6.90^{+1.20}_{-1.41}$	$5.29^{+0.72}_{-0.84}$
SPT-CL J0256-5617$^{\text{X}}$	44.0997	−56.2980	7.45	0.50	87 ± 14	$0.64 \pm 0.04^*$	$4.31^{+0.65}_{-0.86}$	$6.71^{+1.03}_{-1.37}$	$4.83^{+0.64}_{-0.74}$
SPT-CL J0257-4817	44.4463	−48.2970	5.13	0.25	66 ± 15	$0.44 \pm 0.04^*$	$3.34^{+0.65}_{-0.83}$	$5.12^{+1.02}_{-1.30}$	$3.89^{+0.68}_{-0.81}$
SPT-CL J0257-5732	44.3506	−57.5426	5.04	0.25	60 ± 14	0.434	$3.19^{+0.64}_{-0.83}$	$4.88^{+0.98}_{-1.30}$	$3.73^{+0.65}_{-0.79}$
SPT-CL J0257-5842	44.3934	−58.7107	5.33	1.00	61 ± 12	$0.42 \pm 0.04^*$	$3.37^{+0.64}_{-0.84}$	$5.16^{+0.99}_{-1.31}$	$3.91^{+0.69}_{-0.79}$
SPT-CL J0259-4556	44.9007	−45.9352	5.74	0.50	73 ± 14	$0.43 \pm 0.04^*$	$3.78^{+0.73}_{-0.86}$	$5.76^{+1.13}_{-1.35}$	$4.28^{+0.71}_{-0.79}$
SPT-CL J0304-4401$^{\text{X}}$	46.0702	−44.0314	15.69	1.00	173 ± 15	0.458	$7.59^{+1.06}_{-1.26}$	$11.83^{+1.69}_{-2.01}$	$8.37^{+0.84}_{-1.03}$
SPT-CL J0304-4748	46.1503	−47.8115	6.38	0.25	76 ± 18	0.51 ± 0.03	$3.98^{+0.69}_{-0.86}$	$6.14^{+1.08}_{-1.37}$	$4.56^{+0.69}_{-0.78}$
SPT-CL J0304-4921$^{\text{X}}$	46.0619	−49.3612	12.75	1.25	135 ± 13	0.392	$6.72^{+0.92}_{-1.16}$	$10.40^{+1.46}_{-1.84}$	$7.53^{+0.77}_{-0.96}$
SPT-CL J0307-4123	46.8782	−41.3903	5.22	1.00	56 ± 17	$0.59 \pm 0.04^*$	$3.28^{+0.64}_{-0.81}$	$5.07^{+1.01}_{-1.29}$	$3.75^{+0.65}_{-0.77}$
SPT-CL J0307-5042$^{\text{X}}$	46.9516	−50.7071	8.44	0.50	95 ± 13	0.55 ± 0.03	$4.92^{+0.77}_{-0.93}$	$7.66^{+1.22}_{-1.47}$	$5.56^{+0.66}_{-0.80}$
SPT-CL J0307-6225$^{\text{WL, X}}$	46.8336	−62.4327	8.46	0.75	92 ± 12	0.580	$4.76^{+0.71}_{-0.89}$	$7.41^{+1.13}_{-1.42}$	$5.36^{+0.64}_{-0.77}$
SPT-CL J0309-4958	47.2623	−49.9741	5.66	0.50	64 ± 17	$0.55 \pm 0.04^*$	$3.58^{+0.68}_{-0.84}$	$5.52^{+1.07}_{-1.33}$	$4.08^{+0.69}_{-0.78}$
SPT-CL J0310-4647	47.6291	−46.7834	7.12	0.50	80 ± 13	0.707	$4.18^{+0.68}_{-0.87}$	$6.56^{+1.09}_{-1.40}$	$4.70^{+0.65}_{-0.74}$
SPT-CL J0311-6354	47.8289	−63.9073	7.16	1.00	74 ± 12	0.284^*	$4.45^{+0.75}_{-0.91}$	$6.74^{+1.14}_{-1.41}$	$5.14^{+0.69}_{-0.80}$
SPT-CL J0313-5334$^{\text{X}}$	48.4809	−53.5781	6.09	0.25	77 ± 22	1.474^*	$2.96^{+0.53}_{-0.86}$	$4.84^{+0.89}_{-1.45}$	$3.31^{+0.55}_{-0.61}$
SPT-CL J0317-5935$^{\text{WL}}$	49.3216	−59.5851	6.26	0.25	70 ± 17	0.469	$3.85^{+0.69}_{-0.82}$	$5.93^{+1.08}_{-1.29}$	$4.41^{+0.68}_{-0.76}$
SPT-CL J0324-6236$^{\text{X}}$	51.0530	−62.6021	8.75	0.50	97 ± 13	0.750^*	$4.68^{+0.74}_{-0.90}$	$7.38^{+1.19}_{-1.46}$	$5.24^{+0.62}_{-0.74}$
SPT-CL J0328-5541	52.1675	−55.6957	7.32	1.25	82 ± 12	0.084	$4.64^{+0.79}_{-0.97}$	$6.92^{+1.19}_{-1.48}$	$5.47^{+0.71}_{-0.85}$
SPT-CL J0330-5228	52.7287	−52.4698	11.57	1.50	121 ± 11	0.442	$6.01^{+0.84}_{-1.02}$	$9.30^{+1.33}_{-1.61}$	$6.75^{+0.73}_{-0.87}$
SPT-CL J0334-4659$^{\text{X}}$	53.5464	−46.9932	9.20	1.00	96 ± 12	0.485	$5.08^{+0.77}_{-0.92}$	$7.86^{+1.21}_{-1.46}$	$5.76^{+0.67}_{-0.80}$
SPT-CL J0334-4815	53.7097	−48.2638	7.22	0.25	87 ± 17	$0.64 \pm 0.04^*$	$4.13^{+0.74}_{-0.82}$	$6.43^{+1.17}_{-1.31}$	$4.66^{+0.63}_{-0.73}$
SPT-CL J0336-4005	54.1568	−40.0972	5.10	1.75	51 ± 12	0.52 ± 0.04	$3.28^{+0.65}_{-0.85}$	$5.05^{+1.01}_{-1.34}$	$3.76^{+0.66}_{-0.79}$
SPT-CL J0336-4704	54.1214	−47.0692	5.96	0.75	64 ± 12	$0.81 \pm 0.03^*$	$3.33^{+0.60}_{-0.80}$	$5.26^{+0.97}_{-1.29}$	$3.81^{+0.63}_{-0.70}$
SPT-CL J0337-4928	54.4573	−49.4738	5.57	1.50	61 ± 13	$0.49 \pm 0.04^*$	$3.39^{+0.67}_{-0.80}$	$5.23^{+1.05}_{-1.27}$	$3.94^{+0.68}_{-0.76}$
SPT-CL J0337-6207	54.4708	−62.1175	5.03	1.75	56 ± 15	> 1.30	$\cdots$	$\cdots$	$\cdots$
SPT-CL J0337-6300	54.4692	−63.0103	5.16	0.25	56 ± 17	$0.47 \pm 0.04^*$	$3.24^{+0.64}_{-0.82}$	$4.97^{+0.99}_{-1.28}$	$3.76^{+0.66}_{-0.78}$
SPT-CL J0339-3952	54.7862	−39.8734	5.45	0.25	14 ± 3	> 0.59	$\cdots$	$\cdots$	$\cdots$
SPT-CL J0339-4545	54.8908	−45.7535	5.34	0.75	58 ± 12	$0.86 \pm 0.03^*$	$3.02^{+0.57}_{-0.79}$	$4.76^{+0.91}_{-1.28}$	$3.42^{+0.59}_{-0.70}$
SPT-CL J0341-5731	55.3981	−57.5238	5.27	0.25	67 ± 18	$0.64 \pm 0.04^*$	$3.18^{+0.58}_{-0.81}$	$4.94^{+0.92}_{-1.29}$	$3.64^{+0.65}_{-0.74}$
SPT-CL J0341-6143	55.3487	−61.7193	5.68	3.00	88 ± 16	$0.61 \pm 0.04^*$	$3.40^{+0.64}_{-0.81}$	$5.27^{+1.01}_{-1.29}$	$3.90^{+0.66}_{-0.74}$

Table 5 continued

BOCQUET ET AL.

Table 5 *(continued)*

SPT ID	R.A.	DEC.	ξ	$\theta_{\rm c}$	$Y_{\rm SZ}$	Redshift	M_{500c}	M_{200c}	$M_{500c}^{\rm no\ syst.}$
	(J2000)	(J2000)		arcmin	10^{-6}arcmin^2		$[10^{14} M_\odot/h_{70}]$	$[10^{14} M_\odot/h_{70}]$	$[10^{14} M_\odot/h_{70}]$
SPT-CL J0342-4028	55.5604	−40.4785	6.91	0.50	79 ± 12	0.44 ± 0.04*	$4.23^{+0.71}_{-0.88}$	$6.54^{+1.12}_{-1.40}$	$4.92^{+0.68}_{-0.79}$
SPT-CL J0342-5354	55.5220	−53.9118	5.54	1.00	56 ± 11	0.52 ± 0.04*	$3.37^{+0.65}_{-0.79}$	$5.19^{+1.02}_{-1.25}$	$3.90^{+0.66}_{-0.76}$
SPT-CL J0343-5518	55.7617	−55.3032	6.01	0.25	71 ± 17	0.54 ± 0.04*	$3.64^{+0.70}_{-0.80}$	$5.62^{+1.10}_{-1.26}$	$4.19^{+0.67}_{-0.75}$
SPT-CL J0344-5452	56.0922	−54.8794	7.98	0.25	97 ± 23	1.05 ± 0.09*	$4.03^{+0.68}_{-0.91}$	$6.47^{+1.11}_{-1.51}$	$4.49^{+0.56}_{-0.67}$
SPT-CL J0344-5518	56.2068	−55.3018	5.18	0.75	85 ± 37	0.36 ± 0.02*	$3.37^{+0.67}_{-0.85}$	$5.10^{+1.03}_{-1.31}$	$3.90^{+0.67}_{-0.80}$
SPT-CL J0345-6419	56.2510	−64.3326	5.54	0.25	61 ± 16	0.94 ± 0.03*	$2.99^{+0.58}_{-0.83}$	$4.76^{+0.93}_{-1.35}$	$3.47^{+0.60}_{-0.69}$
SPT-CL J0346-5439$^{\rm WL,\ X}$	56.7247	−54.6505	9.25	0.75	96 ± 12	0.530	$5.06^{+0.72}_{-0.93}$	$7.86^{+1.14}_{-1.47}$	$5.72^{+0.66}_{-0.80}$
SPT-CL J0348-4515$^{\rm WL,\ X}$	57.0737	−45.2510	10.12	0.75	106 ± 12	0.359	$5.57^{+0.83}_{-0.96}$	$8.55^{+1.29}_{-1.51}$	$6.33^{+0.70}_{-0.85}$
SPT-CL J0350-4620	57.7216	−46.3342	6.44	0.25	72 ± 12	0.72 ± 0.04*	$3.59^{+0.63}_{-0.83}$	$5.66^{+1.01}_{-1.34}$	$4.18^{+0.62}_{-0.72}$
SPT-CL J0351-4109	57.7545	−41.1566	9.05	1.25	101 ± 12	0.62 ± 0.04*	$5.06^{+0.78}_{-0.93}$	$7.93^{+1.24}_{-1.49}$	$5.69^{+0.66}_{-0.80}$
SPT-CL J0352-5647$^{\rm X}$	58.2367	−56.7996	7.13	0.75	79 ± 12	0.649*	$4.12^{+0.67}_{-0.86}$	$6.43^{+1.06}_{-1.38}$	$4.65^{+0.63}_{-0.73}$
SPT-CL J0353-5043	58.3853	−50.7278	5.35	0.25	66 ± 19	> 0.82	⋯	⋯	⋯
SPT-CL J0354-5151	58.6584	−51.8589	5.82	0.25	67 ± 18	0.67 ± 0.04*	$3.43^{+0.65}_{-0.79}$	$5.34^{+1.03}_{-1.26}$	$3.89^{+0.65}_{-0.72}$
SPT-CL J0354-5904	58.5612	−59.0733	6.42	1.25	72 ± 12	0.42 ± 0.04*	$3.98^{+0.69}_{-0.82}$	$6.10^{+1.08}_{-1.28}$	$4.57^{+0.69}_{-0.77}$
SPT-CL J0356-5337	59.0855	−53.6331	6.02	0.25	77 ± 17	1.036*	$3.21^{+0.59}_{-0.81}$	$5.11^{+0.95}_{-1.33}$	$3.59^{+0.59}_{-0.66}$
SPT-CL J0359-5218	59.8362	−52.3157	6.27	0.75	66 ± 14	0.66 ± 0.04*	$3.68^{+0.64}_{-0.79}$	$5.73^{+1.01}_{-1.26}$	$4.15^{+0.65}_{-0.72}$
SPT-CL J0402-4611	60.5770	−46.1891	5.53	1.25	61 ± 12	0.36 ± 0.02*	$3.54^{+0.68}_{-0.82}$	$5.37^{+1.04}_{-1.27}$	$4.07^{+0.71}_{-0.78}$
SPT-CL J0403-5719	60.9681	−57.3237	5.86	0.25	65 ± 16	0.467	$3.63^{+0.69}_{-0.83}$	$5.57^{+1.08}_{-1.30}$	$4.18^{+0.69}_{-0.76}$
SPT-CL J0404-4418	61.1978	−44.3044	7.40	0.25	98 ± 25	0.85 ± 0.03*	$4.07^{+0.69}_{-0.92}$	$6.46^{+1.12}_{-1.50}$	$4.64^{+0.62}_{-0.72}$
SPT-CL J0405-4648	61.2861	−46.8111	6.63	1.00	73 ± 11	0.36 ± 0.04*	$4.07^{+0.72}_{-0.83}$	$6.23^{+1.11}_{-1.30}$	$4.70^{+0.69}_{-0.77}$
SPT-CL J0405-4916	61.4917	−49.2709	7.17	0.75	77 ± 12	0.30 ± 0.02*	$4.38^{+0.70}_{-0.86}$	$6.66^{+1.08}_{-1.34}$	$5.08^{+0.68}_{-0.80}$
SPT-CL J0406-4805$^{\rm X}$	61.7275	−48.0866	8.13	1.00	87 ± 12	0.737	$4.41^{+0.68}_{-0.85}$	$6.94^{+1.09}_{-1.37}$	$4.95^{+0.61}_{-0.73}$
SPT-CL J0406-5455	61.6906	−54.9210	5.91	0.25	74 ± 20	0.72 ± 0.04*	$3.40^{+0.65}_{-0.78}$	$5.32^{+1.03}_{-1.26}$	$3.89^{+0.64}_{-0.71}$
SPT-CL J0410-6343	62.5170	−63.7275	5.61	0.50	63 ± 13	0.53 ± 0.04*	$3.47^{+0.65}_{-0.82}$	$5.34^{+1.01}_{-1.29}$	$3.95^{+0.69}_{-0.75}$
SPT-CL J0411-4819$^{\rm X}$	62.8154	−48.3218	15.26	1.00	160 ± 13	0.424	$7.25^{+0.99}_{-1.22}$	$11.25^{+1.56}_{-1.94}$	$8.04^{+0.81}_{-1.00}$
SPT-CL J0411-6340	62.8597	−63.6804	6.35	0.25	70 ± 13	0.14 ± 0.01	$4.14^{+0.78}_{-0.89}$	$6.20^{+1.19}_{-1.37}$	$4.86^{+0.73}_{-0.81}$
SPT-CL J0412-5106	63.2297	−51.1098	5.15	0.25	56 ± 13	0.24 ± 0.02*	$3.38^{+0.66}_{-0.82}$	$5.10^{+1.00}_{-1.27}$	$3.97^{+0.69}_{-0.81}$
SPT-CL J0412-5743	63.0248	−57.7201	5.30	1.25	59 ± 12	0.34 ± 0.03	$3.42^{+0.69}_{-0.84}$	$5.19^{+1.06}_{-1.31}$	$3.98^{+0.69}_{-0.80}$
SPT-CL J0416-6359	64.1630	−63.9964	6.10	0.50	65 ± 12	0.35 ± 0.02*	$3.89^{+0.73}_{-0.84}$	$5.91^{+1.12}_{-1.31}$	$4.47^{+0.71}_{-0.78}$
SPT-CL J0417-4427	64.4097	−44.4640	9.13	0.50	106 ± 15	0.56 ± 0.04*	$5.15^{+0.77}_{-0.94}$	$8.02^{+1.22}_{-1.49}$	$5.81^{+0.68}_{-0.81}$
SPT-CL J0417-4748$^{\rm X}$	64.3451	−47.8139	14.24	0.25	173 ± 26	0.579	$6.73^{+0.97}_{-1.18}$	$10.57^{+1.55}_{-1.90}$	$7.41^{+0.75}_{-0.92}$
SPT-CL J0418-4552	64.6693	−45.8820	5.51	0.75	59 ± 12	0.67 ± 0.04*	$3.25^{+0.64}_{-0.78}$	$5.06^{+1.01}_{-1.25}$	$3.71^{+0.64}_{-0.73}$
SPT-CL J0421-4845	65.3206	−48.7612	5.82	0.25	77 ± 21	1.51 ± 0.11*	$2.81^{+0.57}_{-0.82}$	$4.57^{+0.93}_{-1.36}$	$3.03^{+0.52}_{-0.59}$
SPT-CL J0422-4608	65.7490	−46.1436	5.05	0.50	56 ± 15	0.66 ± 0.04*	$3.02^{+0.56}_{-0.81}$	$4.68^{+0.89}_{-1.25}$	$3.47^{+0.59}_{-0.74}$
SPT-CL J0422-5140	65.5923	−51.6755	5.86	1.00	60 ± 14	0.59 ± 0.03	$3.50^{+0.67}_{-0.81}$	$5.42^{+1.06}_{-1.29}$	$4.01^{+0.65}_{-0.74}$
SPT-CL J0424-4406	66.0045	−44.1107	6.39	0.75	68 ± 12	0.36 ± 0.02*	$4.02^{+0.72}_{-0.85}$	$6.17^{+1.12}_{-1.34}$	$4.73^{+0.72}_{-0.79}$
SPT-CL J0426-5455$^{\rm WL,\ X}$	66.5199	−54.9197	8.85	0.50	109 ± 13	0.642*	$4.83^{+0.73}_{-0.93}$	$7.57^{+1.16}_{-1.48}$	$5.43^{+0.63}_{-0.78}$
SPT-CL J0428-6049	67.0305	−60.8292	5.11	1.25	54 ± 12	0.70 ± 0.04*	$3.05^{+0.58}_{-0.78}$	$4.75^{+0.92}_{-1.24}$	$3.49^{+0.60}_{-0.74}$
SPT-CL J0430-6251	67.7094	−62.8548	5.29	0.25	59 ± 13	> 1.50	⋯	⋯	⋯
SPT-CL J0431-6126	67.8417	−61.4350	6.19	2.50	177 ± 26	0.058	$4.09^{+0.76}_{-0.94}$	$6.07^{+1.15}_{-1.42}$	$4.84^{+0.75}_{-0.83}$
SPT-CL J0433-5630	68.2541	−56.5025	5.32	1.75	59 ± 12	0.692	$3.17^{+0.63}_{-0.81}$	$4.93^{+1.00}_{-1.29}$	$3.61^{+0.63}_{-0.74}$
SPT-CL J0438-5419$^{\rm X}$	69.5749	−54.3212	22.88	0.50	237 ± 11	0.421	$9.42^{+1.34}_{-1.63}$	$14.70^{+2.13}_{-2.60}$	$10.28^{+1.00}_{-1.25}$
SPT-CL J0439-4600	69.8087	−46.0142	8.28	0.25	98 ± 13	0.33 ± 0.02*	$4.86^{+0.75}_{-0.93}$	$7.42^{+1.16}_{-1.46}$	$5.58^{+0.68}_{-0.81}$
SPT-CL J0439-5330	69.9290	−53.5038	5.61	0.75	61 ± 13	0.41 ± 0.04*	$3.49^{+0.68}_{-0.80}$	$5.33^{+1.06}_{-1.25}$	$4.06^{+0.69}_{-0.77}$
SPT-CL J0440-4657	70.2307	−46.9654	7.13	1.25	79 ± 12	0.31 ± 0.02*	$4.32^{+0.72}_{-0.88}$	$6.60^{+1.11}_{-1.38}$	$5.05^{+0.68}_{-0.79}$
SPT-CL J0441-4855$^{\rm X}$	70.4511	−48.9190	8.56	0.50	92 ± 14	0.74 ± 0.05*	$4.49^{+0.70}_{-0.89}$	$7.12^{+1.13}_{-1.45}$	$5.12^{+0.62}_{-0.74}$
SPT-CL J0444-4352	71.1683	−43.8735	5.01	1.50	58 ± 18	0.53 ± 0.04*	$3.20^{+0.63}_{-0.80}$	$4.94^{+0.98}_{-1.27}$	$3.69^{+0.64}_{-0.79}$
SPT-CL J0444-5603	71.1136	−56.0576	5.18	0.25	71 ± 21	0.94 ± 0.03*	$2.92^{+0.58}_{-0.77}$	$4.61^{+0.94}_{-1.25}$	$3.29^{+0.57}_{-0.69}$
SPT-CL J0445-4230	71.2775	−42.5087	7.07	0.75	79 ± 12	0.41 ± 0.04*	$4.41^{+0.74}_{-0.89}$	$6.77^{+1.15}_{-1.40}$	$5.05^{+0.68}_{-0.80}$
SPT-CL J0446-4606	71.7325	−46.1012	5.71	0.25	78 ± 21	1.70 ± 0.20	$2.63^{+0.52}_{-0.81}$	$4.29^{+0.87}_{-1.36}$	$2.82^{+0.48}_{-0.57}$
SPT-CL J0446-5849	71.5156	−58.8228	7.18	0.25	90 ± 14	1.19 ± 0.10	$3.60^{+0.63}_{-0.89}$	$5.81^{+1.03}_{-1.48}$	$4.01^{+0.57}_{-0.64}$

Table 5 continued

Table 5 (continued)

SPT ID	R.A.	DEC.	ξ	θ_c	Y_{SZ}	Redshift	M_{500c}	M_{200c}	$M_{500c}^{\text{no syst.}}$
	(J2000)	(J2000)		arcmin	10^{-6}arcmin^2		$[10^{14}M_\odot/h_{70}]$	$[10^{14}M_\odot/h_{70}]$	$[10^{14}M_\odot/h_{70}]$
SPT-CL J0447-5055	71.8445	−50.9227	5.96	0.25	65 ± 13	0.40 ± 0.04*	$3.71^{+0.69}_{-0.82}$	$5.67^{+1.07}_{-1.28}$	$4.29^{+0.69}_{-0.77}$
SPT-CL J0449-4901[X]	72.2742	−49.0246	8.91	0.50	96 ± 12	0.792	$4.69^{+0.74}_{-0.92}$	$7.42^{+1.18}_{-1.49}$	$5.20^{+0.61}_{-0.73}$
SPT-CL J0454-4211	73.7352	−42.1839	6.69	0.25	88 ± 21	0.81 ± 0.03*	$3.82^{+0.61}_{-0.87}$	$6.04^{+0.99}_{-1.41}$	$4.33^{+0.64}_{-0.72}$
SPT-CL J0455-4159	73.9973	−41.9931	5.09	0.75	56 ± 14	0.29 ± 0.02*	$3.41^{+0.68}_{-0.84}$	$5.17^{+1.05}_{-1.31}$	$4.01^{+0.70}_{-0.84}$
SPT-CL J0456-4906	74.1212	−49.1056	5.99	0.25	64 ± 12	0.93 ± 0.03	$3.26^{+0.59}_{-0.82}$	$5.18^{+0.95}_{-1.33}$	$3.69^{+0.61}_{-0.67}$
SPT-CL J0456-5116[X]	74.1163	−51.2768	8.58	1.00	90 ± 11	0.562	$4.78^{+0.73}_{-0.87}$	$7.43^{+1.15}_{-1.39}$	$5.39^{+0.65}_{-0.78}$
SPT-CL J0459-4947[X]	74.9269	−49.7872	6.29	0.25	74 ± 17	1.700	$2.68^{+0.50}_{-0.83}$	$4.41^{+0.84}_{-1.41}$	$3.08^{+0.53}_{-0.53}$
SPT-CL J0500-5116	75.2425	−51.2709	5.92	1.50	58 ± 13	0.11 ± 0.03	$3.76^{+0.74}_{-0.88}$	$5.60^{+1.11}_{-1.34}$	$4.46^{+0.72}_{-0.79}$
SPT-CL J0502-6113	75.5450	−61.2321	5.11	0.50	57 ± 12	0.78 ± 0.05*	$3.12^{+0.60}_{-0.79}$	$4.90^{+0.97}_{-1.27}$	$3.52^{+0.61}_{-0.75}$
SPT-CL J0504-4929	76.0069	−49.4854	5.33	0.75	60 ± 14	0.20 ± 0.03	$3.90^{+0.78}_{-0.96}$	$5.86^{+1.18}_{-1.48}$	$4.53^{+0.79}_{-0.89}$
SPT-CL J0505-6145	76.3966	−61.7505	6.90	1.25	81 ± 13	0.29 ± 0.02*	$4.47^{+0.76}_{-0.93}$	$6.77^{+1.17}_{-1.43}$	$5.15^{+0.72}_{-0.83}$
SPT-CL J0509-5342[WL, X]	77.3374	−53.7053	8.50	0.75	92 ± 12	0.461	$4.69^{+0.72}_{-0.84}$	$7.23^{+1.13}_{-1.32}$	$5.35^{+0.64}_{-0.78}$
SPT-CL J0509-6118	77.4741	−61.3067	10.37	1.00	119 ± 12	0.39 ± 0.04*	$5.92^{+0.87}_{-1.08}$	$9.10^{+1.36}_{-1.70}$	$6.65^{+0.72}_{-0.89}$
SPT-CL J0510-4519	77.5805	−45.3270	9.50	1.00	117 ± 13	0.200	$6.04^{+0.95}_{-1.10}$	$9.16^{+1.46}_{-1.70}$	$6.94^{+0.78}_{-0.95}$
SPT-CL J0511-5154	77.9209	−51.9044	7.09	0.25	79 ± 17	0.645	$3.96^{+0.64}_{-0.80}$	$6.18^{+1.01}_{-1.28}$	$4.47^{+0.62}_{-0.71}$
SPT-CL J0512-5139	78.1587	−51.6621	6.21	1.00	64 ± 11	0.57 ± 0.04*	$3.55^{+0.65}_{-0.78}$	$5.50^{+1.02}_{-1.25}$	$4.11^{+0.64}_{-0.72}$
SPT-CL J0516-5430[WL, X]	79.1513	−54.5108	12.41	1.50	153 ± 13	0.295	$6.29^{+0.88}_{-1.06}$	$9.63^{+1.37}_{-1.67}$	$7.12^{+0.74}_{-0.91}$
SPT-CL J0516-5755	79.2398	−57.9167	5.73	0.75	59 ± 12	0.97 ± 0.03*	$3.17^{+0.60}_{-0.76}$	$4.98^{+0.95}_{-1.23}$	$3.42^{+0.58}_{-0.65}$
SPT-CL J0517-6119	79.2844	−61.3181	7.16	0.25	99 ± 24	0.83 ± 0.03*	$4.05^{+0.69}_{-0.88}$	$6.42^{+1.11}_{-1.43}$	$4.59^{+0.62}_{-0.73}$
SPT-CL J0517-6311	79.4094	−63.1989	5.15	0.50	65 ± 12	0.45 ± 0.10*	$3.49^{+0.67}_{-0.86}$	$5.29^{+1.02}_{-1.34}$	$3.90^{+0.69}_{-0.82}$
SPT-CL J0521-5104	80.3012	−51.0766	7.22	1.00	77 ± 11	0.675	$3.97^{+0.68}_{-0.82}$	$6.21^{+1.08}_{-1.32}$	$4.49^{+0.62}_{-0.71}$
SPT-CL J0522-5026	80.5159	−50.4394	5.20	1.75	53 ± 13	0.52 ± 0.03	$3.10^{+0.60}_{-0.78}$	$4.77^{+0.93}_{-1.22}$	$3.60^{+0.62}_{-0.74}$
SPT-CL J0525-4715	81.4555	−47.2556	10.14	1.00	115 ± 13	0.191	$6.36^{+0.93}_{-1.11}$	$9.64^{+1.44}_{-1.72}$	$7.23^{+0.80}_{-0.98}$
SPT-CL J0528-4417	82.0610	−44.2922	5.09	1.75	55 ± 14	0.64 ± 0.04*	$3.41^{+0.67}_{-0.86}$	$5.30^{+1.05}_{-1.37}$	$3.86^{+0.67}_{-0.82}$
SPT-CL J0528-5300[X]	82.0196	−53.0024	6.55	0.50	75 ± 13	0.768	$3.60^{+0.62}_{-0.78}$	$5.65^{+0.98}_{-1.26}$	$4.06^{+0.60}_{-0.68}$
SPT-CL J0529-4138	82.4857	−41.6365	6.24	0.50	79 ± 13	0.78 ± 0.05*	$3.88^{+0.69}_{-0.91}$	$6.14^{+1.10}_{-1.48}$	$4.40^{+0.69}_{-0.77}$
SPT-CL J0529-6051	82.3493	−60.8578	5.58	0.50	71 ± 19	0.73 ± 0.05*	$3.32^{+0.66}_{-0.82}$	$5.24^{+1.06}_{-1.32}$	$3.84^{+0.66}_{-0.74}$
SPT-CL J0530-4139	82.6754	−41.6502	6.19	0.25	84 ± 22	0.78 ± 0.05*	$3.85^{+0.71}_{-0.91}$	$6.07^{+1.14}_{-1.48}$	$4.37^{+0.70}_{-0.77}$
SPT-CL J0532-5450	83.0307	−54.8445	5.24	0.25	58 ± 15	0.43 ± 0.03	$3.21^{+0.64}_{-0.79}$	$4.90^{+0.99}_{-1.23}$	$3.72^{+0.64}_{-0.76}$
SPT-CL J0533-5005[WL, X]	83.4009	−50.0901	7.08	0.25	84 ± 21	0.881	$3.72^{+0.60}_{-0.86}$	$5.89^{+0.96}_{-1.40}$	$4.18^{+0.57}_{-0.67}$
SPT-CL J0535-4801	83.9464	−48.0229	6.34	0.25	85 ± 22	0.93 ± 0.03*	$3.85^{+0.70}_{-0.90}$	$6.12^{+1.13}_{-1.47}$	$4.25^{+0.71}_{-0.72}$
SPT-CL J0535-5956	83.7934	−59.9394	5.20	0.25	60 ± 17	0.62 ± 0.04*	$3.03^{+0.61}_{-0.77}$	$4.70^{+0.95}_{-1.22}$	$3.50^{+0.61}_{-0.72}$
SPT-CL J0536-6109	84.1630	−61.1543	6.39	0.25	89 ± 23	1.09 ± 0.09*	$3.46^{+0.62}_{-0.87}$	$5.55^{+1.02}_{-1.42}$	$3.88^{+0.61}_{-0.67}$
SPT-CL J0537-6504	84.3548	−65.0695	10.54	0.75	122 ± 12	0.20 ± 0.10	$6.14^{+0.92}_{-1.10}$	$9.32^{+1.41}_{-1.71}$	$7.02^{+0.77}_{-0.94}$
SPT-CL J0539-6013	84.9561	−60.2272	5.05	1.75	54 ± 16	> 0.74	$\cdots$	$\cdots$	$\cdots$
SPT-CL J0540-5744	85.0043	−57.7405	6.74	0.25	78 ± 19	0.761	$3.68^{+0.62}_{-0.81}$	$5.79^{+0.99}_{-1.30}$	$4.16^{+0.60}_{-0.69}$
SPT-CL J0542-4100[X]	85.7167	−41.0044	7.92	0.75	97 ± 13	0.640	$4.89^{+0.79}_{-0.93}$	$7.66^{+1.25}_{-1.49}$	$5.48^{+0.68}_{-0.82}$
SPT-CL J0543-4250	85.9447	−42.8379	6.67	1.50	84 ± 15	0.62 ± 0.04*	$4.34^{+0.74}_{-0.90}$	$6.75^{+1.17}_{-1.43}$	$4.85^{+0.71}_{-0.80}$
SPT-CL J0543-6219	85.7564	−62.3252	8.21	0.75	95 ± 14	0.51 ± 0.10*	$5.01^{+0.79}_{-0.93}$	$7.70^{+1.24}_{-1.47}$	$5.53^{+0.68}_{-0.81}$
SPT-CL J0544-3950	86.2456	−39.8453	6.32	0.75	104 ± 13	0.52 ± 0.04*	$4.22^{+0.72}_{-0.94}$	$6.53^{+1.13}_{-1.48}$	$4.78^{+0.73}_{-0.82}$
SPT-CL J0546-5345[WL, X]	86.6525	−53.7625	10.76	0.50	121 ± 15	1.066	$4.84^{+0.76}_{-1.09}$	$7.81^{+1.24}_{-1.81}$	$5.33^{+0.59}_{-0.71}$
SPT-CL J0549-6205	87.3344	−62.0858	25.81	0.25	302 ± 15	0.375	$10.74^{+1.68}_{-1.72}$	$16.74^{+2.67}_{-2.73}$	$11.66^{+1.14}_{-1.40}$
SPT-CL J0550-6358	87.6825	−63.9746	5.53	0.25	69 ± 19	0.69 ± 0.04*	$3.43^{+0.67}_{-0.81}$	$5.35^{+1.07}_{-1.29}$	$3.85^{+0.67}_{-0.76}$
SPT-CL J0551-4339	87.8798	−43.6596	6.00	0.75	71 ± 14	0.33 ± 0.02*	$4.16^{+0.75}_{-0.92}$	$6.34^{+1.16}_{-1.44}$	$4.82^{+0.82}_{-0.82}$
SPT-CL J0551-5709[WL]	87.9041	−57.1557	8.21	0.50	84 ± 11	0.423	$4.61^{+0.69}_{-0.88}$	$7.09^{+1.07}_{-1.38}$	$5.28^{+0.64}_{-0.78}$
SPT-CL J0552-4937	88.1783	−49.6208	5.05	0.25	65 ± 23	> 1.50	$\cdots$	$\cdots$	$\cdots$
SPT-CL J0555-6406[X]	88.8662	−64.1032	12.72	1.25	142 ± 12	0.345	$6.82^{+0.93}_{-1.15}$	$10.50^{+1.45}_{-1.82}$	$7.64^{+0.78}_{-0.97}$
SPT-CL J0556-5403	89.2026	−54.0609	5.77	0.25	70 ± 19	0.93 ± 0.06	$3.06^{+0.62}_{-0.78}$	$4.84^{+0.99}_{-1.26}$	$3.48^{+0.58}_{-0.66}$
SPT-CL J0557-4113	89.4557	−41.2310	5.37	0.75	65 ± 14	0.81 ± 0.03*	$3.41^{+0.67}_{-0.84}$	$5.37^{+1.08}_{-1.36}$	$3.82^{+0.67}_{-0.78}$
SPT-CL J0559-5249[WL, X]	89.9251	−52.8260	10.64	1.00	106 ± 11	0.609	$5.33^{+0.73}_{-0.96}$	$8.34^{+1.17}_{-1.55}$	$5.97^{+0.65}_{-0.80}$
SPT-CL J0559-6022	89.9419	−60.3832	5.67	0.25	80 ± 23	> 1.50	$\cdots$	$\cdots$	$\cdots$

Table 5 continued

BOCQUET ET AL.

Table 5 *(continued)*

SPT ID	R.A.	DEC.	ξ	θ_c	Y_{SZ}	Redshift	M_{500c}	M_{200c}	$M_{500c}^{\text{no syst.}}$
	(J2000)	(J2000)		arcmin	10^{-6}arcmin^2		$[10^{14}M_\odot/h_{70}]$	$[10^{14}M_\odot/h_{70}]$	$[10^{14}M_\odot/h_{70}]$
SPT-CL J0600-4353	90.0614	−43.8879	6.85	0.75	77 ± 15	0.36 ± 0.04	$4.44^{+0.75}_{-0.90}$	$6.79^{+1.16}_{-1.40}$	$5.09^{+0.71}_{-0.82}$
SPT-CL J0603-4714	90.9883	−47.2379	7.65	1.75	85 ± 12	0.274^*	$4.84^{+0.78}_{-0.92}$	$7.39^{+1.21}_{-1.44}$	$5.63^{+0.70}_{-0.85}$
SPT-CL J0607-4448$^{\text{X}}$	91.8984	−44.8033	6.44	0.25	92 ± 25	1.401^*	$3.25^{+0.58}_{-0.91}$	$5.29^{+0.96}_{-1.53}$	$3.60^{+0.57}_{-0.63}$
SPT-CL J0611-4724	92.9212	−47.4111	5.61	0.25	65 ± 16	$0.45 \pm 0.04^*$	$3.65^{+0.69}_{-0.84}$	$5.62^{+1.08}_{-1.33}$	$4.23^{+0.73}_{-0.81}$
SPT-CL J0612-4317	93.0249	−43.2992	6.14	1.75	74 ± 14	$0.64 \pm 0.04^*$	$3.78^{+0.67}_{-0.86}$	$5.89^{+1.07}_{-1.38}$	$4.32^{+0.69}_{-0.76}$
SPT-CL J0613-5627	93.4558	−56.4597	7.04	0.25	100 ± 14	$0.81 \pm 0.06^*$	$4.07^{+0.66}_{-0.89}$	$6.45^{+1.06}_{-1.44}$	$4.60^{+0.63}_{-0.73}$
SPT-CL J0615-5746$^{\text{WL, X}}$	93.9650	−57.7763	26.42	0.25	311 ± 16	0.972	$9.67^{+1.57}_{-2.12}$	$15.76^{+2.61}_{-3.54}$	$10.16^{+0.98}_{-1.20}$
SPT-CL J0616-4407	94.0685	−44.1223	5.62	0.25	73 ± 20	$0.71 \pm 0.04^*$	$3.46^{+0.65}_{-0.84}$	$5.42^{+1.03}_{-1.35}$	$3.92^{+0.67}_{-0.76}$
SPT-CL J0617-5507	94.2808	−55.1321	5.53	0.25	80 ± 15	$0.95 \pm 0.09^*$	$3.24^{+0.63}_{-0.79}$	$5.14^{+1.02}_{-1.29}$	$3.60^{+0.63}_{-0.72}$
SPT-CL J0619-5802	94.9221	−58.0382	6.29	0.25	76 ± 17	$0.55 \pm 0.04^*$	$3.94^{+0.74}_{-0.85}$	$6.10^{+1.17}_{-1.35}$	$4.51^{+0.70}_{-0.77}$
SPT-CL J0620-4715	95.0965	−47.2591	5.22	0.75	63 ± 14	0.23 ± 0.03	$3.63^{+0.73}_{-0.94}$	$5.46^{+1.12}_{-1.44}$	$4.22^{+0.75}_{-0.86}$
SPT-CL J0622-4645	95.7104	−46.7658	5.18	0.25	69 ± 20	$0.60 \pm 0.04^*$	$3.32^{+0.64}_{-0.82}$	$5.14^{+1.01}_{-1.30}$	$3.79^{+0.66}_{-0.79}$
SPT-CL J0625-4330	96.4382	−43.5003	5.18	0.25	76 ± 19	$0.68 \pm 0.04^*$	$3.24^{+0.63}_{-0.85}$	$5.05^{+1.00}_{-1.35}$	$3.71^{+0.64}_{-0.78}$
SPT-CL J0626-4446	96.7411	−44.7748	6.03	1.75	69 ± 14	$0.44 \pm 0.04^*$	$3.93^{+0.70}_{-0.86}$	$6.03^{+1.09}_{-1.35}$	$4.50^{+0.76}_{-0.77}$
SPT-CL J0628-4143	97.2049	−41.7250	13.89	0.75	166 ± 13	0.176	$7.52^{+1.10}_{-1.24}$	$11.42^{+1.70}_{-1.92}$	$8.46^{+0.87}_{-1.07}$
SPT-CL J0636-4942	99.1686	−49.7034	7.40	1.00	79 ± 13	0.35 ± 0.03	$4.70^{+0.76}_{-0.93}$	$7.19^{+1.19}_{-1.46}$	$5.40^{+0.70}_{-0.83}$
SPT-CL J0637-4327	99.2774	−43.4513	5.10	3.00	63 ± 15	> 1.50	$\cdots$	$\cdots$	$\cdots$
SPT-CL J0637-4829	99.3467	−48.4877	10.00	2.75	128 ± 20	0.203	$5.99^{+0.92}_{-1.07}$	$9.08^{+1.41}_{-1.66}$	$6.85^{+0.76}_{-0.93}$
SPT-CL J0637-6112	99.2600	−61.2064	5.10	0.25	67 ± 21	> 1.50	$\cdots$	$\cdots$	$\cdots$
SPT-CL J0638-5358	99.6978	−53.9749	22.69	0.75	262 ± 14	0.226	$10.28^{+1.44}_{-1.71}$	$15.79^{+2.25}_{-2.69}$	$11.29^{+1.10}_{-1.36}$
SPT-CL J0640-5113$^{\text{X}}$	100.0645	−51.2204	6.86	0.50	83 ± 14	1.316^*	$3.51^{+0.61}_{-0.95}$	$5.71^{+1.00}_{-1.58}$	$3.89^{+0.58}_{-0.65}$
SPT-CL J0641-4733	100.2895	−47.5657	7.13	0.25	86 ± 22	$0.78 \pm 0.05^*$	$4.22^{+0.69}_{-0.92}$	$6.63^{+1.10}_{-1.47}$	$4.68^{+0.64}_{-0.74}$
SPT-CL J0641-5950	100.3788	−59.8490	7.11	0.75	79 ± 13	$0.52 \pm 0.04^*$	$4.42^{+0.72}_{-0.87}$	$6.84^{+1.13}_{-1.38}$	$5.02^{+0.69}_{-0.79}$
SPT-CL J0643-4535	100.9332	−45.5978	5.05	0.25	72 ± 20	$0.95 \pm 0.09^*$	$3.01^{+0.57}_{-0.80}$	$4.76^{+0.91}_{-1.30}$	$3.34^{+0.57}_{-0.73}$
SPT-CL J0643-5056	100.9550	−50.9486	5.03	0.75	67 ± 22	> 1.50	$\cdots$	$\cdots$	$\cdots$
SPT-CL J0645-5413	101.3735	−54.2214	18.32	1.25	219 ± 12	0.164	$9.02^{+1.31}_{-1.53}$	$13.74^{+2.03}_{-2.39}$	$10.05^{+1.00}_{-1.24}$
SPT-CL J0646-6236	101.6391	−62.6136	8.67	0.25	110 ± 16	$0.89 \pm 0.03^*$	$4.31^{+0.72}_{-1.02}$	$6.99^{+1.18}_{-1.71}$	$5.17^{+0.62}_{-0.74}$
SPT-CL J0647-5828	101.9843	−58.4801	6.26	1.00	65 ± 13	$0.44 \pm 0.04^*$	$4.00^{+0.74}_{-0.89}$	$6.15^{+1.15}_{-1.40}$	$4.64^{+0.72}_{-0.79}$
SPT-CL J0649-4510	102.4473	−45.1685	5.19	1.50	52 ± 13	$0.55 \pm 0.04^*$	$3.37^{+0.68}_{-0.86}$	$5.20^{+1.07}_{-1.35}$	$3.85^{+0.67}_{-0.80}$
SPT-CL J0650-4503	102.6815	−45.0641	9.25	0.25	112 ± 16	$0.40 \pm 0.04^*$	$5.45^{+0.85}_{-0.98}$	$8.41^{+1.33}_{-1.54}$	$6.22^{+0.71}_{-0.87}$
SPT-CL J0651-4037	102.8193	−40.6273	6.67	1.50	76 ± 12	$0.24 \pm 0.02^*$	$4.41^{+0.75}_{-0.93}$	$6.68^{+1.17}_{-1.44}$	$5.15^{+0.74}_{-0.84}$
SPT-CL J0653-5744	103.3316	−57.7490	7.70	1.25	84 ± 12	0.24 ± 0.03	$4.96^{+0.78}_{-0.96}$	$7.52^{+1.19}_{-1.49}$	$5.71^{+0.72}_{-0.87}$
SPT-CL J0655-5234$^{\text{X}}$	103.9626	−52.5677	7.76	0.50	91 ± 15	0.470	$4.77^{+0.75}_{-0.91}$	$7.37^{+1.18}_{-1.44}$	$5.42^{+0.67}_{-0.82}$
SPT-CL J0655-5541	103.9137	−55.6931	5.64	1.00	76 ± 12	0.29 ± 0.02	$3.80^{+0.74}_{-0.89}$	$5.75^{+1.14}_{-1.38}$	$4.44^{+0.75}_{-0.83}$
SPT-CL J0658-5556$^{\text{X}}$	104.6317	−55.9465	39.05	1.25	491 ± 12	0.296	$14.47^{+2.07}_{-2.45}$	$22.55^{+3.27}_{-3.91}$	$15.38^{+1.48}_{-1.80}$
SPT-CL J0659-5300	104.7763	−53.0114	5.13	0.75	61 ± 13	$0.48 \pm 0.04^*$	$3.39^{+0.66}_{-0.85}$	$5.21^{+1.03}_{-1.33}$	$3.90^{+0.67}_{-0.81}$
SPT-CL J2006-5325	301.6622	−53.4303	5.38	1.00	56 ± 13	> 1.50	$\cdots$	$\cdots$	$\cdots$
SPT-CL J2011-5725	302.8527	−57.4217	5.34	0.75	60 ± 12	0.279	$3.41^{+0.69}_{-0.83}$	$5.15^{+1.05}_{-1.28}$	$3.99^{+0.69}_{-0.79}$
SPT-CL J2012-4130	303.0008	−41.5011	5.71	1.25	64 ± 13	0.150	$3.97^{+0.81}_{-0.93}$	$5.95^{+1.23}_{-1.43}$	$4.67^{+0.82}_{-0.82}$
SPT-CL J2012-5649	303.1128	−56.8298	6.38	2.50	74 ± 49	0.055	$4.10^{+0.76}_{-0.90}$	$6.08^{+1.14}_{-1.36}$	$4.85^{+0.72}_{-0.81}$
SPT-CL J2017-6258	304.4836	−62.9782	6.32	1.50	68 ± 12	0.535	$3.73^{+0.63}_{-0.83}$	$5.76^{+0.98}_{-1.31}$	$4.27^{+0.66}_{-0.74}$
SPT-CL J2019-5642	304.7698	−56.7101	5.36	0.75	59 ± 12	0.23 ± 0.02	$3.46^{+0.69}_{-0.85}$	$5.20^{+1.05}_{-1.30}$	$4.05^{+0.70}_{-0.80}$
SPT-CL J2020-6314	305.0273	−63.2434	5.38	0.25	60 ± 15	0.537	$3.25^{+0.62}_{-0.79}$	$5.00^{+0.97}_{-1.24}$	$3.74^{+0.65}_{-0.74}$
SPT-CL J2022-6323$^{\text{WL}}$	305.5261	−63.3989	6.51	0.25	75 ± 13	0.383	$3.96^{+0.71}_{-0.80}$	$6.05^{+1.10}_{-1.24}$	$4.56^{+0.67}_{-0.77}$
SPT-CL J2023-5535	305.8376	−55.5906	13.63	1.75	158 ± 15	0.232	$6.84^{+0.97}_{-1.16}$	$10.43^{+1.51}_{-1.82}$	$7.77^{+0.79}_{-0.98}$
SPT-CL J2025-5117	306.4837	−51.2901	9.11	0.75	107 ± 15	0.22 ± 0.02	$5.76^{+0.88}_{-1.06}$	$8.74^{+1.35}_{-1.65}$	$6.61^{+0.76}_{-0.92}$
SPT-CL J2026-4513	306.6145	−45.2268	5.24	0.50	66 ± 21	0.689^*	$3.37^{+0.65}_{-0.87}$	$5.25^{+1.03}_{-1.39}$	$3.82^{+0.67}_{-0.80}$
SPT-CL J2030-5638$^{\text{WL}}$	307.7036	−56.6362	5.50	1.00	60 ± 12	0.394	$3.41^{+0.67}_{-0.81}$	$5.20^{+1.03}_{-1.27}$	$3.97^{+0.68}_{-0.77}$
SPT-CL J2031-4037$^{\text{X}}$	307.9669	−40.6197	17.52	0.75	204 ± 13	0.342	$8.58^{+1.25}_{-1.45}$	$13.28^{+1.98}_{-2.30}$	$9.44^{+0.94}_{-1.16}$
SPT-CL J2032-5627$^{\text{WL}}$	308.0807	−56.4580	8.61	1.25	93 ± 12	0.284	$4.97^{+0.80}_{-0.94}$	$7.56^{+1.24}_{-1.46}$	$5.74^{+0.67}_{-0.83}$
SPT-CL J2034-5936$^{\text{X}}$	308.5401	−59.6017	8.53	0.25	101 ± 21	$0.76 \pm 0.03^*$	$4.41^{+0.67}_{-0.91}$	$6.99^{+1.08}_{-1.48}$	$5.03^{+0.61}_{-0.72}$

Table 5 continued

Table 5 *(continued)*

SPT ID	R.A.	DEC.	ξ	θ_c	Y_{SZ}	Redshift	M_{500c}	M_{200c}	$M_{500c}^{\text{no syst.}}$
	(J2000)	(J2000)		arcmin	10^{-6}arcmin^2		$[10^{14}M_\odot/h_{70}]$	$[10^{14}M_\odot/h_{70}]$	$[10^{14}M_\odot/h_{70}]$
SPT-CL J2035-5251[X]	308.8012	−52.8519	9.71	0.75	102 ± 13	0.528	$5.71^{+0.83}_{-0.99}$	$8.89^{+1.32}_{-1.57}$	$6.38^{+0.72}_{-0.87}$
SPT-CL J2040-4451[X]	310.2483	−44.8602	6.72	0.25	94 ± 26	1.478	$3.38^{+0.61}_{-0.94}$	$5.54^{+1.02}_{-1.59}$	$3.76^{+0.58}_{-0.63}$
SPT-CL J2040-5342	310.2194	−53.7116	5.91	0.50	69 ± 19	$0.52 \pm 0.04^*$	$3.88^{+0.74}_{-0.86}$	$6.01^{+1.17}_{-1.36}$	$4.44^{+0.76}_{-0.77}$
SPT-CL J2040-5725[WL]	310.0573	−57.4295	6.24	0.50	67 ± 12	0.930	$3.37^{+0.62}_{-0.80}$	$5.34^{+1.00}_{-1.29}$	$3.78^{+0.59}_{-0.66}$
SPT-CL J2043-5035[X]	310.8284	−50.5938	7.18	0.50	87 ± 17	0.723	$4.39^{+0.70}_{-0.91}$	$6.90^{+1.11}_{-1.47}$	$4.91^{+0.66}_{-0.78}$
SPT-CL J2050-4213	312.5706	−42.2173	7.20	0.75	91 ± 18	$0.50 \pm 0.04^*$	$4.52^{+0.76}_{-0.90}$	$6.99^{+1.19}_{-1.43}$	$5.13^{+0.68}_{-0.80}$
SPT-CL J2051-6256	312.8000	−62.9344	5.03	1.25	48 ± 12	$0.48 \pm 0.04^*$	$3.10^{+0.62}_{-0.80}$	$4.75^{+0.96}_{-1.26}$	$3.60^{+0.62}_{-0.76}$
SPT-CL J2055-5456	313.9957	−54.9368	7.04	0.50	81 ± 12	0.139	$4.84^{+0.84}_{-0.99}$	$7.26^{+1.28}_{-1.51}$	$5.64^{+0.77}_{-0.88}$
SPT-CL J2056-5459	314.2174	−54.9937	6.07	0.50	74 ± 14	0.718	$3.46^{+0.67}_{-0.78}$	$5.41^{+1.07}_{-1.26}$	$3.92^{+0.64}_{-0.70}$
SPT-CL J2058-5608	314.5879	−56.1453	5.01	0.25	65 ± 16	0.606	$3.02^{+0.60}_{-0.77}$	$4.67^{+0.94}_{-1.22}$	$3.47^{+0.60}_{-0.74}$
SPT-CL J2101-5542	315.3077	−55.7038	5.03	1.00	63 ± 14	$0.27 \pm 0.02^*$	$3.27^{+0.63}_{-0.86}$	$4.92^{+0.97}_{-1.31}$	$3.82^{+0.66}_{-0.80}$
SPT-CL J2101-6123	315.4579	−61.3981	5.53	0.50	62 ± 12	$0.70 \pm 0.04^*$	$3.20^{+0.58}_{-0.77}$	$4.99^{+0.92}_{-1.23}$	$3.64^{+0.63}_{-0.71}$
SPT-CL J2106-4421	316.5711	−44.3537	7.59	0.25	104 ± 25	$0.78 \pm 0.08^*$	$4.43^{+0.75}_{-0.89}$	$7.00^{+1.20}_{-1.45}$	$4.93^{+0.65}_{-0.75}$
SPT-CL J2106-5844[WL, X]	316.5206	−58.7451	22.22	0.25	271 ± 43	1.132	$7.73^{+1.23}_{-1.81}$	$12.66^{+2.05}_{-3.05}$	$8.28^{+0.79}_{-0.98}$
SPT-CL J2108-4445	317.1911	−44.7646	5.60	0.50	66 ± 14	$0.80 \pm 0.03^*$	$3.38^{+0.58}_{-0.83}$	$5.33^{+0.93}_{-1.34}$	$3.82^{+0.67}_{-0.75}$
SPT-CL J2109-5040	317.3825	−50.6765	5.55	2.00	61 ± 13	$0.62 \pm 0.04^*$	$3.62^{+0.66}_{-0.90}$	$5.62^{+1.04}_{-1.43}$	$4.10^{+0.72}_{-0.79}$
SPT-CL J2110-5244	317.5514	−52.7492	6.28	0.50	71 ± 14	$0.61 \pm 0.04^*$	$4.00^{+0.74}_{-0.89}$	$6.23^{+1.17}_{-1.42}$	$4.56^{+0.70}_{-0.78}$
SPT-CL J2111-5339	317.9226	−53.6503	5.37	1.00	60 ± 13	0.45 ± 0.04	$3.65^{+0.72}_{-0.90}$	$5.60^{+1.11}_{-1.41}$	$4.19^{+0.73}_{-0.84}$
SPT-CL J2112-4434	318.2129	−44.5807	8.80	0.75	105 ± 13	$0.53 \pm 0.04^*$	$5.20^{+0.82}_{-0.96}$	$8.08^{+1.30}_{-1.53}$	$5.86^{+0.69}_{-0.83}$
SPT-CL J2115-4659	318.8011	−46.9910	5.18	3.00	64 ± 13	0.299	$3.66^{+0.72}_{-0.91}$	$5.55^{+1.11}_{-1.41}$	$4.25^{+0.75}_{-0.87}$
SPT-CL J2118-5055	319.7317	−50.9325	5.54	0.50	68 ± 20	0.625	$3.61^{+0.68}_{-0.88}$	$5.61^{+1.07}_{-1.39}$	$4.09^{+0.71}_{-0.80}$
SPT-CL J2120-4016	320.1371	−40.2730	5.16	0.75	62 ± 14	$0.25 \pm 0.02^*$	$3.56^{+0.71}_{-0.89}$	$5.39^{+1.08}_{-1.38}$	$4.20^{+0.74}_{-0.86}$
SPT-CL J2120-4728	320.1597	−47.4782	5.72	0.25	76 ± 22	$1.03 \pm 0.09^*$	$3.35^{+0.64}_{-0.84}$	$5.34^{+1.03}_{-1.46}$	$3.70^{+0.65}_{-0.73}$
SPT-CL J2121-6335	320.4272	−63.5840	5.58	2.75	77 ± 22	0.217	$3.58^{+0.72}_{-0.84}$	$5.39^{+1.09}_{-1.29}$	$4.21^{+0.70}_{-0.80}$
SPT-CL J2124-6124	321.1462	−61.4102	8.50	0.50	90 ± 12	0.435	$4.80^{+0.75}_{-0.89}$	$7.39^{+1.17}_{-1.40}$	$5.47^{+0.66}_{-0.79}$
SPT-CL J2130-6458	322.7280	−64.9767	7.63	1.00	80 ± 12	0.316	$4.52^{+0.73}_{-0.89}$	$6.89^{+1.13}_{-1.40}$	$5.23^{+0.66}_{-0.79}$
SPT-CL J2131-4019	322.7659	−40.3216	12.51	0.50	152 ± 13	0.45 ± 0.03	$6.73^{+0.92}_{-1.16}$	$10.45^{+1.45}_{-1.84}$	$7.49^{+0.78}_{-0.96}$
SPT-CL J2132-4349	323.1698	−43.8288	6.68	1.00	77 ± 13	$0.52 \pm 0.04^*$	$4.29^{+0.75}_{-0.89}$	$6.60^{+1.17}_{-1.40}$	$4.82^{+0.69}_{-0.79}$
SPT-CL J2134-4109	323.5288	−41.1593	6.80	0.25	89 ± 21	$0.70 \pm 0.04^*$	$4.12^{+0.65}_{-0.89}$	$6.46^{+1.03}_{-1.43}$	$4.65^{+0.67}_{-0.76}$
SPT-CL J2134-4238	323.5020	−42.6438	8.52	0.75	100 ± 14	0.196	$5.41^{+0.87}_{-1.00}$	$8.18^{+1.34}_{-1.54}$	$6.23^{+0.74}_{-0.89}$
SPT-CL J2135-5726[WL, X]	323.9164	−57.4409	10.51	0.50	119 ± 19	0.427	$5.58^{+0.83}_{-0.97}$	$8.62^{+1.30}_{-1.54}$	$6.31^{+0.70}_{-0.84}$
SPT-CL J2136-4704	324.1191	−47.0818	6.24	0.25	80 ± 18	0.425	$4.17^{+0.74}_{-0.89}$	$6.41^{+1.14}_{-1.40}$	$4.78^{+0.74}_{-0.83}$
SPT-CL J2136-6307	324.2346	−63.1244	6.24	0.75	67 ± 13	0.926	$3.36^{+0.61}_{-0.83}$	$5.33^{+0.99}_{-1.34}$	$3.78^{+0.59}_{-0.67}$
SPT-CL J2138-6008[WL]	324.5052	−60.1333	12.64	0.75	136 ± 12	0.319	$6.44^{+0.88}_{-1.07}$	$9.88^{+1.38}_{-1.69}$	$7.27^{+0.76}_{-0.93}$
SPT-CL J2140-5727	325.1391	−57.4576	5.35	0.25	62 ± 14	0.404	$3.33^{+0.62}_{-0.84}$	$5.08^{+0.96}_{-1.30}$	$3.87^{+0.67}_{-0.78}$
SPT-CL J2143-5509	325.8481	−55.1603	5.10	0.25	61 ± 13	> 1.50	$\cdots$	$\cdots$	$\cdots$
SPT-CL J2145-4348	326.3640	−43.8029	5.32	0.25	69 ± 18	$0.49 \pm 0.04^*$	$3.54^{+0.71}_{-0.86}$	$5.44^{+1.10}_{-1.35}$	$4.03^{+0.70}_{-0.81}$
SPT-CL J2145-5644[WL, X]	326.4682	−56.7476	12.60	0.50	142 ± 17	0.480	$6.22^{+0.89}_{-1.06}$	$9.67^{+1.40}_{-1.68}$	$6.97^{+0.73}_{-0.89}$
SPT-CL J2146-4633[X]	326.6462	−46.5500	9.67	0.50	121 ± 13	0.933	$5.19^{+0.80}_{-1.10}$	$8.30^{+1.31}_{-1.80}$	$5.71^{+0.65}_{-0.78}$
SPT-CL J2146-4846	326.5310	−48.7800	5.96	1.00	83 ± 14	0.623	$3.85^{+0.70}_{-0.90}$	$5.98^{+1.10}_{-1.44}$	$4.35^{+0.71}_{-0.79}$
SPT-CL J2146-5736	326.6957	−57.6148	6.19	0.50	71 ± 13	0.603	$3.63^{+0.62}_{-0.83}$	$5.63^{+0.97}_{-1.31}$	$4.13^{+0.64}_{-0.72}$
SPT-CL J2148-6116[X]	327.1812	−61.2780	7.47	0.75	79 ± 12	0.571	$4.23^{+0.69}_{-0.85}$	$6.57^{+1.09}_{-1.36}$	$4.82^{+0.63}_{-0.74}$
SPT-CL J2152-5633	328.1450	−56.5632	5.47	1.75	71 ± 13	> 1.50	$\cdots$	$\cdots$	$\cdots$
SPT-CL J2155-5224	328.8871	−52.4116	5.17	1.75	75 ± 19	$0.55 \pm 0.04^*$	$3.46^{+0.65}_{-0.85}$	$5.34^{+1.02}_{-1.35}$	$3.95^{+0.69}_{-0.82}$
SPT-CL J2155-6048	328.9850	−60.8078	5.74	1.00	61 ± 12	0.539	$3.45^{+0.65}_{-0.79}$	$5.32^{+1.01}_{-1.25}$	$3.95^{+0.67}_{-0.73}$
SPT-CL J2158-5451	329.5415	−54.8501	5.17	1.25	54 ± 13	> 0.95	$\cdots$	$\cdots$	$\cdots$
SPT-CL J2159-6244	329.9910	−62.7414	6.49	1.00	71 ± 12	0.391	$3.92^{+0.72}_{-0.82}$	$6.00^{+1.12}_{-1.28}$	$4.54^{+0.68}_{-0.76}$
SPT-CL J2201-5956	330.4734	−59.9437	15.26	1.75	183 ± 13	0.097	$8.24^{+1.19}_{-1.43}$	$12.44^{+1.82}_{-2.21}$	$9.27^{+0.93}_{-1.16}$
SPT-CL J2203-5047	330.7988	−50.7899	5.66	1.25	68 ± 16	$0.90 \pm 0.05^*$	$3.19^{+0.57}_{-0.90}$	$5.12^{+0.92}_{-1.48}$	$3.79^{+0.66}_{-0.74}$
SPT-CL J2205-5927	331.2665	−59.4564	5.55	1.00	64 ± 12	$0.37 \pm 0.03^*$	$3.82^{+0.73}_{-0.91}$	$5.80^{+1.12}_{-1.42}$	$4.35^{+0.79}_{-0.80}$
SPT-CL J2206-5807	331.6558	−58.1290	6.24	0.75	72 ± 13	0.60 ± 0.04	$3.95^{+0.71}_{-0.89}$	$6.14^{+1.12}_{-1.42}$	$4.51^{+0.70}_{-0.78}$

Table 5 continued

Table 5 *(continued)*

SPT ID	R.A. (J2000)	DEC. (J2000)	ξ	θ_c arcmin	Y_{SZ} $10^{-6}\mathrm{arcmin}^2$	Redshift	M_{500c} $[10^{14}M_\odot/h_{70}]$	M_{200c} $[10^{14}M_\odot/h_{70}]$	$M_{500c}^{\mathrm{no\ syst.}}$ $[10^{14}M_\odot/h_{70}]$
SPT-CL J2211-4833	332.8260	−48.5603	7.40	1.75	87 ± 13	0.24 ± 0.03	$4.73^{+0.78}_{-0.94}$	$7.16^{+1.21}_{-1.46}$	$5.48^{+0.71}_{-0.85}$
SPT-CL J2214-4642	333.7184	−46.7050	7.17	0.25	91 ± 25	1.16 ± 0.10	$3.76^{+0.64}_{-0.93}$	$6.07^{+1.05}_{-1.54}$	$4.17^{+0.58}_{-0.67}$
SPT-CL J2217-6509	334.4895	−65.1506	6.77	3.00	117 ± 27	0.095	$4.56^{+0.79}_{-0.99}$	$6.81^{+1.20}_{-1.51}$	$5.34^{+0.74}_{-0.86}$
SPT-CL J2218-4519$^{\mathrm{X}}$	334.7486	−45.3205	8.84	0.75	102 ± 13	0.637^*	$4.99^{+0.76}_{-0.95}$	$7.82^{+1.21}_{-1.52}$	$5.60^{+0.66}_{-0.80}$
SPT-CL J2219-5708	334.9614	−57.1384	8.91	0.75	105 ± 13	$0.31 \pm 0.02^*$	$5.48^{+0.90}_{-0.94}$	$8.40^{+1.35}_{-1.54}$	$6.31^{+0.74}_{-0.89}$
SPT-CL J2220-4534	335.0809	−45.5824	7.07	0.75	77 ± 13	$0.64 \pm 0.04^*$	$4.27^{+0.69}_{-0.84}$	$6.64^{+1.09}_{-1.33}$	$4.77^{+0.66}_{-0.76}$
SPT-CL J2222-4834$^{\mathrm{X}}$	335.7122	−48.5735	9.08	0.50	99 ± 15	0.652	$5.08^{+0.74}_{-0.95}$	$7.97^{+1.19}_{-1.53}$	$5.69^{+0.66}_{-0.80}$
SPT-CL J2228-5828	337.2153	−58.4686	5.15	1.50	57 ± 13	$0.73 \pm 0.05^*$	$3.26^{+0.62}_{-0.84}$	$5.10^{+0.98}_{-1.34}$	$3.69^{+0.63}_{-0.79}$
SPT-CL J2232-5959$^{\mathrm{X}}$	338.1487	−59.9903	8.80	0.25	113 ± 22	0.595	$5.19^{+0.78}_{-0.97}$	$8.11^{+1.24}_{-1.55}$	$5.81^{+0.68}_{-0.82}$
SPT-CL J2232-6151	338.2319	−61.8558	5.04	2.25	58 ± 16	$0.79 \pm 0.08^*$	$3.09^{+0.59}_{-0.82}$	$4.84^{+0.93}_{-1.32}$	$3.49^{+0.59}_{-0.75}$
SPT-CL J2233-5339$^{\mathrm{X}}$	338.3295	−53.6502	8.29	1.00	98 ± 14	0.440^*	$5.13^{+0.77}_{-0.96}$	$7.91^{+1.20}_{-1.51}$	$5.82^{+0.70}_{-0.85}$
SPT-CL J2235-4416	338.8637	−44.2694	5.38	1.00	65 ± 12	0.45 ± 0.04	$3.50^{+0.68}_{-0.84}$	$5.37^{+1.06}_{-1.31}$	$4.03^{+0.71}_{-0.80}$
SPT-CL J2236-4555$^{\mathrm{X}}$	339.2186	−45.9279	7.72	0.25	111 ± 25	1.17 ± 0.10	$3.98^{+0.69}_{-0.97}$	$6.42^{+1.13}_{-1.60}$	$4.40^{+0.57}_{-0.67}$
SPT-CL J2241-4236	340.4749	−42.6004	5.29	1.25	57 ± 12	0.20 ± 0.03	$3.64^{+0.72}_{-0.90}$	$5.47^{+1.09}_{-1.38}$	$4.25^{+0.75}_{-0.84}$
SPT-CL J2241-4558	340.4365	−45.9685	6.49	0.25	95 ± 22	$1.03 \pm 0.09^*$	$3.59^{+0.64}_{-0.87}$	$5.74^{+1.04}_{-1.43}$	$3.99^{+0.61}_{-0.68}$
SPT-CL J2245-6206$^{\mathrm{X}}$	341.2604	−62.1136	8.74	1.00	101 ± 13	0.586	$5.03^{+0.79}_{-0.96}$	$7.85^{+1.25}_{-1.53}$	$5.67^{+0.66}_{-0.81}$
SPT-CL J2248-4431$^{\mathrm{X}}$	342.1907	−44.5269	42.36	0.75	476 ± 13	0.351	$14.87^{+2.25}_{-2.58}$	$23.31^{+3.59}_{-4.13}$	$15.71^{+1.49}_{-1.83}$
SPT-CL J2249-4442	342.4069	−44.7158	5.11	0.25	68 ± 19	$0.62 \pm 0.04^*$	$3.22^{+0.64}_{-0.82}$	$5.00^{+1.01}_{-1.30}$	$3.68^{+0.64}_{-0.78}$
SPT-CL J2249-6426	342.4296	−64.4342	5.96	2.25	83 ± 35	0.094	$4.12^{+0.78}_{-0.94}$	$6.13^{+1.18}_{-1.42}$	$4.83^{+0.77}_{-0.86}$
SPT-CL J2250-4808	342.6823	−48.1447	5.82	0.25	72 ± 17	$0.98 \pm 0.09^*$	$3.31^{+0.63}_{-0.84}$	$5.26^{+1.02}_{-1.37}$	$3.69^{+0.61}_{-0.70}$
SPT-CL J2251-4848	342.7891	−48.8032	6.42	0.25	86 ± 21	$0.87 \pm 0.08^*$	$3.71^{+0.66}_{-0.87}$	$5.86^{+1.05}_{-1.42}$	$4.15^{+0.64}_{-0.71}$
SPT-CL J2254-4620	343.5880	−46.3436	8.37	1.25	91 ± 15	0.27 ± 0.02	$5.14^{+0.81}_{-0.96}$	$7.82^{+1.25}_{-1.50}$	$5.94^{+0.71}_{-0.86}$
SPT-CL J2254-5805	343.5895	−58.0851	5.36	2.25	95 ± 24	0.153	$3.84^{+0.77}_{-0.94}$	$5.74^{+1.16}_{-1.44}$	$4.48^{+0.78}_{-0.88}$
SPT-CL J2254-6314	343.5145	−63.2450	8.18	1.25	92 ± 15	0.211	$5.16^{+0.81}_{-0.99}$	$7.81^{+1.25}_{-1.53}$	$5.95^{+0.73}_{-0.87}$
SPT-CL J2258-4044$^{\mathrm{X}}$	344.7051	−40.7386	10.95	0.25	153 ± 30	0.897^*	$5.49^{+0.83}_{-1.11}$	$8.79^{+1.34}_{-1.82}$	$6.02^{+0.65}_{-0.79}$
SPT-CL J2259-3952	344.8138	−39.8740	9.02	0.75	105 ± 12	$0.54 \pm 0.04^*$	$5.16^{+0.76}_{-0.98}$	$8.04^{+1.21}_{-1.57}$	$5.84^{+0.68}_{-0.83}$
SPT-CL J2259-5431	344.9818	−54.5294	5.39	0.25	54 ± 14	0.39 ± 0.04	$3.66^{+0.73}_{-0.87}$	$5.59^{+1.13}_{-1.37}$	$4.23^{+0.74}_{-0.83}$
SPT-CL J2259-5617	344.9955	−56.2859	5.73	0.75	56 ± 11	0.153	$4.06^{+0.81}_{-0.97}$	$6.07^{+1.22}_{-1.48}$	$4.72^{+0.83}_{-0.84}$
SPT-CL J2259-6057$^{\mathrm{X}}$	344.7528	−60.9546	9.77	0.50	113 ± 14	$0.81 \pm 0.03^*$	$5.16^{+0.79}_{-1.03}$	$8.22^{+1.28}_{-1.69}$	$5.76^{+0.65}_{-0.79}$
SPT-CL J2300-5331	345.1761	−53.5190	6.44	1.00	62 ± 11	0.262	$3.83^{+0.68}_{-0.83}$	$5.78^{+1.04}_{-1.29}$	$4.47^{+0.67}_{-0.75}$
SPT-CL J2301-4023$^{\mathrm{X}}$	345.4687	−40.3912	8.09	0.50	107 ± 20	0.835^*	$4.47^{+0.73}_{-0.94}$	$7.09^{+1.18}_{-1.53}$	$4.99^{+0.62}_{-0.74}$
SPT-CL J2301-5546	345.4669	−55.7768	5.01	0.50	52 ± 17	0.748	$2.78^{+0.55}_{-0.72}$	$4.34^{+0.86}_{-1.15}$	$3.19^{+0.54}_{-0.67}$
SPT-CL J2306-6505$^{\mathrm{X}}$	346.7298	−65.0910	9.22	0.75	100 ± 12	0.530	$5.29^{+0.75}_{-0.96}$	$8.24^{+1.18}_{-1.53}$	$5.96^{+0.69}_{-0.83}$
SPT-CL J2308-4834	347.2351	−48.5679	5.14	0.25	65 ± 20	> 1.50	$\cdots$	$\cdots$	$\cdots$
SPT-CL J2311-4203	347.8447	−42.0637	5.80	1.00	63 ± 13	1.16 ± 0.10	$2.93^{+0.56}_{-0.80}$	$4.65^{+0.90}_{-1.30}$	$3.50^{+0.58}_{-0.67}$
SPT-CL J2311-5820	347.9924	−58.3452	5.72	0.25	65 ± 18	$0.93 \pm 0.09^*$	$3.10^{+0.67}_{-0.85}$	$4.98^{+1.10}_{-1.40}$	$3.37^{+0.56}_{-0.64}$
SPT-CL J2312-4621	348.0560	−46.3523	6.86	1.25	75 ± 13	0.63 ± 0.04	$2.97^{+0.54}_{-0.75}$	$4.69^{+0.87}_{-1.21}$	$4.68^{+0.66}_{-0.76}$
SPT-CL J2313-4243	348.4995	−42.7256	5.47	1.75	39 ± 26	0.056	$4.12^{+0.71}_{-0.86}$	$6.43^{+1.13}_{-1.37}$	$4.52^{+0.78}_{-0.87}$
SPT-CL J2316-5453	349.2082	−54.8978	6.23	1.00	57 ± 11	$0.37 \pm 0.03^*$	$2.93^{+0.53}_{-0.77}$	$4.57^{+0.84}_{-1.24}$	$4.24^{+0.65}_{-0.73}$
SPT-CL J2319-4716	349.9828	−47.2787	6.17	1.50	62 ± 12	$0.43 \pm 0.04^*$	$3.05^{+0.58}_{-0.80}$	$4.73^{+0.92}_{-1.27}$	$4.54^{+0.75}_{-0.76}$
SPT-CL J2321-5419	350.4022	−54.3231	5.27	0.25	57 ± 12	> 0.97	$\cdots$	$\cdots$	$\cdots$
SPT-CL J2325-4111$^{\mathrm{X}}$	351.3043	−41.1959	12.50	1.50	134 ± 12	0.358	$3.92^{+0.68}_{-0.89}$	$6.02^{+1.06}_{-1.40}$	$7.52^{+0.78}_{-0.96}$
SPT-CL J2329-5831	352.4733	−58.5245	6.62	0.25	67 ± 12	$0.72 \pm 0.04^*$	$3.03^{+0.60}_{-0.78}$	$4.57^{+0.93}_{-1.21}$	$4.05^{+0.60}_{-0.68}$
SPT-CL J2330-4502	352.5708	−45.0344	5.18	1.50	61 ± 12	$0.32 \pm 0.02^*$	$3.55^{+0.60}_{-0.79}$	$5.55^{+0.95}_{-1.27}$	$4.06^{+0.71}_{-0.83}$
SPT-CL J2331-5051$^{\mathrm{WL, X}}$	352.9608	−50.8639	10.47	0.25	106 ± 14	0.576	$3.50^{+0.70}_{-0.88}$	$5.30^{+1.08}_{-1.37}$	$5.81^{+0.64}_{-0.78}$
SPT-CL J2332-5358$^{\mathrm{WL}}$	353.1057	−53.9675	9.12	1.50	106 ± 15	0.402	$2.73^{+0.52}_{-0.73}$	$4.19^{+0.81}_{-1.15}$	$5.54^{+0.64}_{-0.78}$
SPT-CL J2335-4243	353.9710	−42.7328	5.59	0.75	63 ± 13	$0.75 \pm 0.05^*$	$4.84^{+0.74}_{-0.85}$	$7.43^{+1.16}_{-1.33}$	$3.80^{+0.66}_{-0.74}$
SPT-CL J2335-4544$^{\mathrm{X}}$	353.7861	−45.7389	10.37	1.00	112 ± 12	0.547	$3.38^{+0.63}_{-0.84}$	$5.30^{+1.01}_{-1.35}$	$6.38^{+0.70}_{-0.85}$
SPT-CL J2337-5942$^{\mathrm{WL, X}}$	354.3523	−59.7049	20.35	0.25	198 ± 15	0.775	$2.82^{+0.54}_{-0.74}$	$4.35^{+0.84}_{-1.17}$	$8.29^{+0.80}_{-0.99}$
SPT-CL J2341-5119$^{\mathrm{WL, X}}$	355.2991	−51.3281	12.49	0.75	127 ± 12	1.003	$7.71^{+1.09}_{-1.47}$	$12.32^{+1.78}_{-2.42}$	$5.80^{+0.61}_{-0.75}$
SPT-CL J2341-5724$^{\mathrm{X}}$	355.3568	−57.4158	6.87	1.00	64 ± 12	1.259^*	$5.30^{+0.79}_{-1.10}$	$8.53^{+1.29}_{-1.82}$	$3.58^{+0.51}_{-0.59}$

Table 5 continued

Table 5 *(continued)*

SPT ID	R.A. (J2000)	DEC. (J2000)	ξ	θ_c arcmin	Y_{SZ} 10^{-6}arcmin^2	Redshift	M_{500c} $[10^{14}M_\odot/h_{70}]$	M_{200c} $[10^{14}M_\odot/h_{70}]$	$M_{500c}^{\text{no syst.}}$ $[10^{14}M_\odot/h_{70}]$
SPT-CL J2342-5411[WL, X]	355.6892	−54.1856	8.18	0.25	92 ± 20	1.075	$3.27^{+0.65}_{-0.87}$	$4.99^{+1.00}_{-1.35}$	$4.30^{+0.54}_{-0.64}$
SPT-CL J2344-4243[X]	356.1847	−42.7209	27.44	0.50	331 ± 21	0.596	$3.16^{+0.61}_{-0.86}$	$4.76^{+0.94}_{-1.33}$	$11.38^{+1.11}_{-1.35}$
SPT-CL J2345-6405[X]	356.2555	−64.0959	9.42	0.50	109 ± 16	$1.00 \pm 0.09^*$	$10.71^{+1.62}_{-1.94}$	$17.02^{+2.61}_{-3.16}$	$5.33^{+0.61}_{-0.74}$
SPT-CL J2350-5301	357.7272	−53.0212	6.05	0.25	65 ± 16	0.54 ± 0.04	$4.85^{+0.74}_{-1.04}$	$7.79^{+1.20}_{-1.72}$	$3.95^{+0.63}_{-0.71}$
SPT-CL J2351-5452	357.8978	−54.8829	6.28	0.75	64 ± 11	0.384	$3.43^{+0.62}_{-0.77}$	$5.29^{+0.97}_{-1.21}$	$4.25^{+0.66}_{-0.73}$
SPT-CL J2352-4657[X]	358.0631	−46.9569	7.46	0.25	89 ± 13	$0.89 \pm 0.03^*$	$3.66^{+0.66}_{-0.81}$	$5.59^{+1.02}_{-1.26}$	$4.64^{+0.62}_{-0.71}$
SPT-CL J2352-5846	358.0510	−58.7758	5.18	0.75	47 ± 12	> 0.67	$\cdots$	$\cdots$	$\cdots$
SPT-CL J2352-6134	358.1939	−61.5671	6.07	0.25	84 ± 21	$0.89 \pm 0.03^*$	$4.17^{+0.69}_{-0.91}$	$6.63^{+1.11}_{-1.48}$	$3.94^{+0.64}_{-0.71}$
SPT-CL J2353-5512	358.2559	−55.2050	5.10	0.50	51 ± 11	> 1.50	$\cdots$	$\cdots$	$\cdots$
SPT-CL J2354-5633	358.7122	−56.5545	5.70	0.75	56 ± 11	$0.56 \pm 0.04^*$	$3.64^{+0.67}_{-0.82}$	$5.72^{+1.07}_{-1.32}$	$3.74^{+0.62}_{-0.70}$
SPT-CL J2355-5055[WL, X]	358.9498	−50.9320	6.60	0.75	69 ± 11	0.320	$3.26^{+0.61}_{-0.77}$	$5.02^{+0.95}_{-1.21}$	$4.49^{+0.66}_{-0.74}$
SPT-CL J2356-4220	359.0127	−42.3496	5.28	0.25	75 ± 21	$0.80 \pm 0.03^*$	$3.87^{+0.69}_{-0.82}$	$5.88^{+1.06}_{-1.27}$	$3.57^{+0.62}_{-0.74}$
SPT-CL J2358-4354	359.7306	−43.9026	5.80	1.00	68 ± 13	$0.67 \pm 0.04^*$	$3.10^{+0.59}_{-0.81}$	$4.89^{+0.95}_{-1.31}$	$4.03^{+0.68}_{-0.75}$
SPT-CL J2358-6129	359.7075	−61.4862	5.85	1.25	70 ± 13	$0.36 \pm 0.04^*$	$2.65^{+0.50}_{-0.72}$	$4.09^{+0.78}_{-1.14}$	$4.45^{+0.78}_{-0.78}$
SPT-CL J2359-5009[WL, X]	359.9230	−50.1649	6.68	1.00	71 ± 11	0.775	$3.83^{+0.69}_{-0.86}$	$5.84^{+1.08}_{-1.35}$	$4.01^{+0.58}_{-0.67}$